

SANDIA REPORT

SAND2001-3421

Unlimited Release

Printed November 2001

Quantifying Atmospheric Corrosion Processes Using Small Length-Scale Electromechanical Measurements and 3-D Electric Field Modeling

F. Douglas Wall, Michael A. Martinez, Corbett C. Battaile, Nancy A. Missert

Prepared by
Sandia National Laboratories
Albuquerque, New Mexico 87185 and Livermore, California 94550

Sandia is a multiprogram laboratory operated by Sandia Corporation, a Lockheed Martin Company, for the United States Department of Energy under Contract DE-AC04-94AL85000.

Approved for public release; further dissemination unlimited.



Sandia National Laboratories

Issued by Sandia National Laboratories, operated for the United States Department of Energy by Sandia Corporation.

NOTICE: This report was prepared as an account of work sponsored by an agency of the United States Government. Neither the United States Government, nor any agency thereof, nor any of their employees, nor any of their contractors, subcontractors, or their employees, make any warranty, express or implied, or assume any legal liability or responsibility for the accuracy, completeness, or usefulness of any information, apparatus, product, or process disclosed, or represent that its use would not infringe privately owned rights. Reference herein to any specific commercial product, process, or service by trade name, trademark, manufacturer, or otherwise, does not necessarily constitute or imply its endorsement, recommendation, or favoring by the United States Government, any agency thereof, or any of their contractors or subcontractors. The views and opinions expressed herein do not necessarily state or reflect those of the United States Government, any agency thereof, or any of their contractors.

Printed in the United States of America. This report has been reproduced directly from the best available copy.

Available to DOE and DOE contractors from
U.S. Department of Energy
Office of Scientific and Technical Information
P.O. Box 62
Oak Ridge, TN 37831

Telephone: (865)576-8401
Facsimile: (865)576-5728
E-Mail: reports@adonis.osti.gov
Online ordering: <http://www.doe.gov/bridge>

Available to the public from
U.S. Department of Commerce
National Technical Information Service
5285 Port Royal Rd
Springfield, VA 22161

Telephone: (800)553-6847
Facsimile: (703)605-6900
E-Mail: orders@ntis.fedworld.gov
Online order: <http://www.ntis.gov/ordering.htm>



Quantifying Atmospheric Corrosion Processes Using Small Length-Scale Electrochemical Measurements And 3-D Electric Field Modeling

F. Douglas Wall and Michael A. Martinez
Corrosion Science and Technology Department

Corbett C. Battaile
Materials & Process Modeling Department

Nancy A. Missert
Nanostructure and Semiconductor Physics Department

Sandia National Laboratories
P.O. Box 5800
Albuquerque, NM 87185-2356

Abstract

Small length scale atmospheric probes were coupled with highly sensitive electrochemical instrumentation in order to assess the range of applicability of electrochemical measurements to quantifying the corrosion behavior of metals exposed to atmospheric conditions. Additionally, the influence of electrolyte conductance on the galvanic corrosion behavior in heterogeneous systems was studied by developing a 3-D electric field model. Atmospheric probes were constructed using either thin-film lithographic techniques or using off-the-shelf materials such as thin foils, wires and insulating coatings. A range of electrochemical techniques was evaluated including AC electrochemical impedance spectroscopy, galvanic current measurements and DC polarization techniques. Thin-film electrodes had much higher parasitic impedance than the foil electrodes and could be used with AC techniques to resolve electrochemical behavior over a much larger range of frequency. The foil-based electrodes suffered from low parasitic impedance but were ideal for making DC measurements. Thin film gold electrodes allowed quantification of the conductivity of the thin adsorbed electrolyte that forms on the metal surfaces under atmospheric conditions. Aluminum and copper foil-based electrodes demonstrated sensitivity to galvanic corrosion at all humidity levels tested (down to 0% relative humidity). Furthermore, the aluminum foil-based electrodes were capable of resolving to extremely small, localized corrosion events, and it was

possible to determine a critical humidity below which localized corrosion could not be induced or detected. Overall, it was demonstrated that quantitative atmospheric electrochemical measurements can be made under conditions of extremely low relative humidity and contamination level, suggesting the applicability of these techniques to studying aging and reliability in relatively benign atmospheric exposures.

1 INTRODUCTION

Atmospheric corrosion can be a life-limiting process for many mechanical and microelectronic devices. Deriving even a qualitative understanding of how materials will react with non-aggressive service environments over a long period of time is an extremely daunting task. Figure 1 shows a schematic relationship between the sensitivity of measurement, the acceleration factor and the time required to resolve a change in material behavior. Many atmospheric tests are conducted by exposing a sample to a controlled environment and monitoring the morphology of the sample as a function of exposure time. Since visual inspection (e.g., optical microscopy, SEM) requires sufficient damage such that a difference in surface condition is readily apparent, either the environment has to be extremely accelerating, or the exposure time has to be prohibitively long. Furthermore, high acceleration factors can cause shifts in the operative mechanisms influencing atmospheric degradation. Therefore, more sensitive techniques are sought which can resolve changes in materials in reasonable lengths of time and under mildly accelerating conditions. An additional consideration is the ability to quantify the material / environment interactions *in-situ* and in *real time*. This program evaluates the suitability of electrochemical techniques to meeting these goals. Under inundated conditions, electrochemical techniques are widely applied to make direct measurements of the electron transfer processes that accompany metal dissolution. By studying the response of the system to imposed voltages or currents, it is possible to gain quantitative information concerning the kinetics and mechanisms of metal dissolution, as well as gaining information about the electrolyte. The goal of this program is to transfer the technology of inundated electrochemistry to studying corrosion processes under atmospheric conditions. The difficulty in making the transition lies in the fact that inundated electrochemistry takes place in a semi-infinite system whereas atmospheric electrochemistry takes place under thin, adsorbed water layers. As the electrolyte thickness is reduced, the resistance between electrodes increases. As the electrolyte impedance approaches the interfacial impedance associated with dissolution, resolving the latter process becomes increasingly difficult.

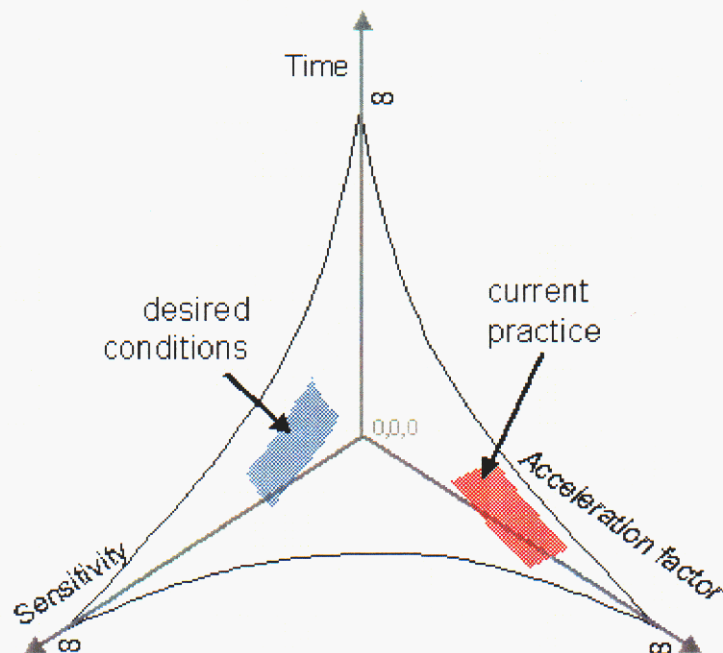


Figure 1 Relationship between measurement sensitivity, acceleration factor and the time required to resolve a change in material behavior.

1.1 Background

The goal of applying electrochemical techniques to atmospheric corrosion has been pursued by various researchers, and reviews of these efforts are available in the literature.¹⁻² The basic approach is to locate coplanar electrodes in close proximity separated by an electrical insulator. Various electrode configurations have included coplanar square electrodes¹, stacked foil electrodes¹⁻⁶ and interdigitated finger electrodes¹⁻².

The most common measurement techniques that have been applied to atmospheric electrochemistry are measuring galvanic coupling current⁷⁻⁹ and electrochemical impedance spectroscopy (EIS)^{1-6,9-11}. Although good correlation has been observed between the electrochemical measurements and mass change, most of the research has been performed under relatively thick electrolyte layers (e.g., 100's of microns) or under conditions of high relative humidity (e.g., 80% RH). Indeed, many of the references cited have studied the corrosion rate as thin water layers dry out under various controlled RH environments (i.e. references 1,2,4,5). Once the electrode has "dried out", the corrosion rate is generally taken to be negligible.

In the current program, we contend that the electrodes can still be electrochemically active at very low relative humidity levels. What has not been shown in the literature is whether or not atmospheric measurements can be made under

conditions that were previously considered to be “dry” (e.g., 60%RH). The magnitudes of corrosion currents that have been reported in the literature are typically on the order of μA down to nA. These may be too coarse of measurements to make definitive statements about the electrochemical activity that occurs under thin water layers. Additionally, most electrodes used to date have had inter-electrode spacing on the order of 0.1 to 1 or more mm. Minimizing the inter-electrode distance should expand the range of RH where electrochemical measurements can be made. Our goal, therefore, is to construct electrodes with minimal inter-electrode spacing and make atmospheric electrochemical measurements using state of the art equipment with current resolution in the 10^{-13} A range. By doing this, we anticipate being able to better define the types of electrochemical measurements that are possible under atmospheric conditions. Additionally, we will determine under what RH levels electrochemical signals can be resolved.

1.2 Objectives and Approach

Our goal in this program is to determine the range of applicability of electrochemical techniques to making measurements under atmospheric conditions. Specifically, we seek to build sensors that will maximize sensitivity to low amplitude currents and potentials and will allow standard electrochemical measurements to be made in the presence of thin adsorbed electrolytes. Two approaches will be taken in building atmospheric sensors. In the first effort photolithographic techniques will be used to generate coplanar thin-film electrodes. In a second effort, traditional materials such as thin foils, wires and readily available insulating materials will be used to construct parallel plate type electrodes. Specific construction techniques will be covered in a later section of this report. The various sensors will be exposed to atmospheres of controlled relative humidity (RH) and contaminant concentration, then both DC and AC measurements will be made on the electrodes. Success of the measurements will be determined by the ability to resolve various modes of corrosion, the magnitudes of corrosion that can be detected and quantified, and the sensitivity to changes in relative humidity.

An additional goal of this program is to assess the role of potential and current fields in determining the corrosion behavior of heterogeneous microstructures or coupled dissimilar metals. Whereas potential drop as a function of distance on an electrode may be of limited concern on surfaces exposed to bulk aqueous solutions, under atmospheric conditions, the thin adsorbed electrolyte can result in large variations in the local potential field. Thus, the nature of the electrolyte layer can control the local polarization of a structure and the available current flow to a corroding site. This phenomenon will be specifically addressed by developing a 3-D mesoscale model for solving the potential and current distributions on a heterogeneous surface. While the boundary conditions are not currently available for a precise numerical solution to specific corroding systems, model development will allow trends and important factors to be identified.

2 ELECTRODE DESIGN

2.1 General considerations for electrode design

The basic design scheme for making electrochemical measurements under atmospheric conditions is to locate two (or more) coplanar, electrically isolated metal surfaces in close proximity to one another. A measurement is made by either passively monitoring the potential or current between electrodes or by imposing a signal and measuring the system response. The two primary design criteria for making successful probes are minimizing the impedance of the system under study and maximizing the parasitic impedance due to the electrode configuration.

The signal from the electrochemical system is comprised of two main components: the polarization resistance (R_p), which is a measure of corrosion rate, and the solution resistance (R_s), which is a measure of the resistance between electrodes due to the adsorbed electrolyte. The total impedance of the system is the sum of these two values. When R_s is of the same magnitude as R_p , it is very difficult to accurately determine either value. R_p is determined by the nature of the corroding system and the electrode area and cannot be changed independently of R_s . On the other hand, R_s increases linearly with electrode separation, decreases with increasing solution layer thickness and decreases with increasing conductivity. Therefore, it is possible to construct electrodes with very small inter-electrode separation in order to define a condition where $R_s < R_p$, making it possible to experimentally resolve both parameters. Increasing the electrode area can reduce the total impedance of the system, because R_s and R_p are inversely proportional to area. Based on these considerations, probes for atmospheric electrochemistry should have a high surface area and minimal inter-electrode separation. Thus long, thin parallel lines of metal are the ideal choice for electrode design.

Because atmospheric electrochemical systems have inherently high impedance, parasitic impedance (Z_{para}) from the design of the probe or from cables or instrumentation can become a limiting factor for making measurements. In traditional, inundated experimentation $Z_{para} \gg R_s + R_p$ such that Z_{para} does not affect the measurement. In atmospheric testing, care must be taken to insure that Z_{para} is maximized. This becomes especially important when AC measurements are made because the capacitance of the probe can become a low impedance pathway, in essence shorting out the electrodes. The electrochemical probe impedance is controlled primarily by two factors: the nature (dielectric constant and resistivity) of the insulating material between the electrodes and the cross sectional area where adjacent electrodes overlap. Thus, independent of insulating material, probe impedance can be maximized by minimizing cross-sectional overlap of electrodes.

The ideal electrode would have a large surface area (to minimize R_p and R_s) but a vanishing thickness (to maximize Z_{para}). Reducing inter-electrode separation is a trade-

off because doing so decreases R_s (desirable) but also decreases Z_{para} (undesirable). The final consideration, however, is resolving both R_s and R_p , which requires minimizing inter-electrode spacing. Therefore, the only strategy available for mitigating the parasitic capacitance is to design electrodes with minimal overlap.

Two basic construction schemes were pursued in this program. The first was based on thin-film photolithographic techniques and was primarily used to produce coplanar electrode structures with very small overlap in the electrode cross-section (nominally 150 nm thick), and therefore very high values of Z_{para} . The basic drawback to this electrode type is that minimal localized corrosion consumes the electrode, rendering it unusable for further experimentation. The second approach was to use readily available forms of metal (e.g., foils and wires) and commercially available insulators and potting compounds to make parallel electrodes with minimized inter-electrode spacing. The primary drawback to this electrode type is the inherently high capacitance (low Z_{para}) that arises from having parallel foils or parallel foils and wires. A significant advantage compared to the thin film electrodes is reusability – the electrode surface can be polished and reused for multiple experiments.

2.2 Thin-film based electrodes

2.2.1 Al/Cu/Pd

Reducing the size scale at which we measure and understand corrosion-based degradation pathways is of primary importance to scientific stewardship of the enduring stockpile. Central to this goal is to understand atmospheric degradation of Al based alloys. Galvanic interactions play a primary role in atmospheric degradation of (1) Al alloys due to electrochemically active second phase particles and (2) high purity Al used in microelectronics due to intimate contact with more noble metals (i.e., Au bond pads). A mechanistic understanding of the atmospheric electrochemical failure modes requires a precise spatial description of potential and current within a corroding system. Measuring the potential field and resulting current map on a small length scale in an adsorbed electrolyte is not possible using conventional electrodes and measurement capabilities. Atmospheric electrochemical sensors must be coplanar and physically oriented to reduce inter-sensor path lengths while providing sufficient surface area for quantification of the corrosion processes. Our microelectrode array design includes Al electrodes to measure the corrosion currents, Cu electrodes which can initiate galvanic corrosion and Pd electrodes which are electrochemically stable and therefore can be used to measure potential fluctuations during the exposures. Initial studies using Au electrodes to measure the potential fluctuations indicated that the Au potential stability was not sufficient.

The layout of the 19 microelectrode array is shown in Figure 2. Each metal layer was deposited onto an SiO_2 coated Si wafer using standard photolithographic liftoff techniques and electron-beam evaporation of the metal layers. An SiO_2 layer was initially deposited on top of the metal layers using ion-beam sputtering, in order to define the

electrode area which would be exposed to the electrolyte: 300 μm x 300 μm for the Al and Cu, and 100 μm x 100 μm for the Pd electrodes. The adhesion of the SiO_2 layer to the noble metals, Pd and Au, was insufficient to provide adequate isolation of the electrode interconnects. Therefore a layer of hard-baked (120°C) photoresist with an HMDS adhesion layer was employed.

2.2.2 Interdigitated Fingers

In order to determine the sensitivity to relative humidity during atmospheric testing, microelectrodes consisting of interdigitated Pt fingers were constructed as shown in Figure 3. These electrodes were deposited on SiO_2 coated Si wafers using standard photolithographic liftoff techniques combined with electron beam evaporation of the Pt layer. As shown in Figure 2, two designs were fabricated, one with 100 μm width lines and 300 μm spacing and another with 200 μm wide lines and 200 μm spacing.

Galvanic coupling between Al and Cu microelectrodes was also investigated by using a variable resistor to control the coupling between the electrodes. These were fabricated using the same techniques described above, but with Al and Cu electron-beam evaporation. The layout of the galvanic fingers is shown in Figure 4. Here the spacing between the electrodes was 20 μm and their width was 40 μm .

2.2.3 Al lines

A new microelectrochemical cell based on individual thin film electrodes has been developed in order to determine how metastable pitting at one site influences initiation at another. Individually addressable Al lines with a 20 μm width and 20 μm spacing allow both current and voltage measurements to be made simultaneously. If a correlation in the magnitude of the current on each line exists as a function of time, then metastable pitting sites can influence each other – either through the potential field or through the local solution chemistry. Studies of the spatial dependence of these interactions as a function of environmental variables, such as relative humidity and Cl concentration, elucidate the relevant mechanism and length scales for atmospheric conditions.

Galvanic coupling was investigated by including a Cu cathode line (20 μm wide, 20 μm spacing) at the center of the Al line array. Here pit initiation will depend upon proximity to the Cu cathode as well as anode/cathode ratio, which is varied on each test site. Again, behavior as a function of relative humidity and Cl concentration can be assessed and incorporated into a mechanistic picture of galvanic corrosion.

The microelectrodes were fabricated on SiO_2 coated Si wafers using standard photolithographic liftoff techniques and electron beam deposition. A 20 nm Ti film was initially deposited to ensure good adhesion between the metal layers and the SiO_2 substrate. Each of the metal layers was ~ 200 nm thick. A thin film of SiO_2 was deposited by ion beam sputtering on top of the metal layers in order to precisely define a window

on the metal areas, 40–400 μm , allowing exposure to the electrolyte. The microelectrodes are shown in Figure 5.

2.2.4 Atmospheric Electrolyte Conductivity

Solution conductivity as a function of relative humidity was measured by forming a microcapacitor using Au thin film deposition to form the capacitor plates, which were separated by (20 μm) using a parylene layer. The Au capacitor plates were defined on glass wafers using standard photolithographic liftoff techniques. The top plate is a 250 μm x 32 mm line and the bottom plate is a 4 mm x 35.3 mm line as shown in Figure 5. Electron-beam evaporation of a 20 nm Ti layer was performed first to ensure good adhesion of the 1.5 μm thick Au layer.

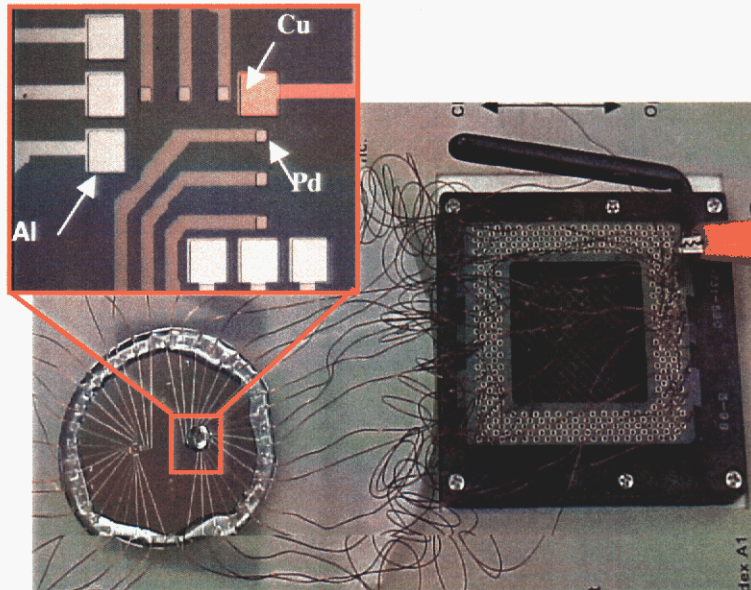


Figure 2 Thin-film multi-electrode connected to MMA via Pentium chip carrier. The enlarged image does not show the other 6 symmetric Al electrodes.

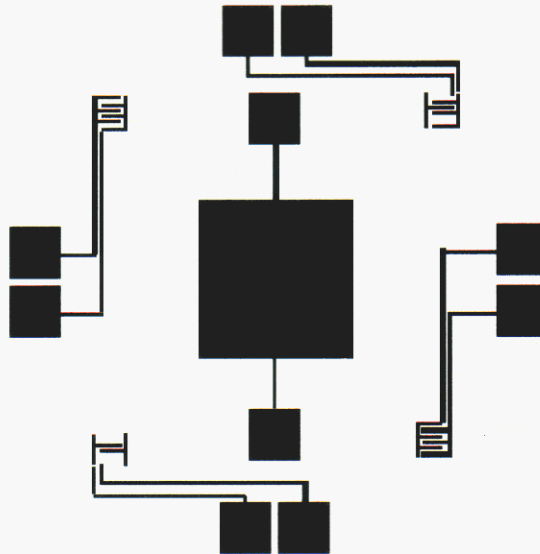


Figure 3 Pt interdigitated fingers showing two different widths and spacings and a central Pt electrode for determining the electrochemical properties of the deposited Pt thin film.

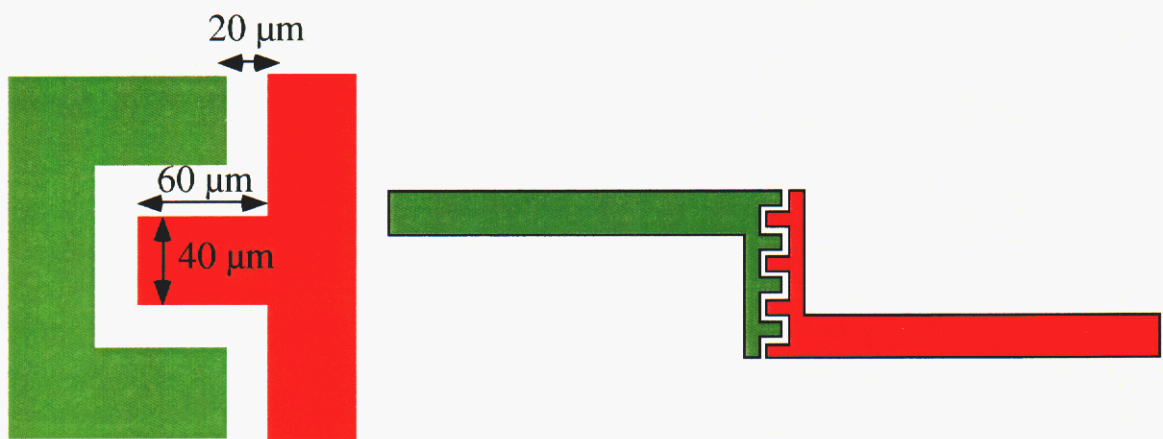


Figure 4 Interdigitated Al and Cu fingers

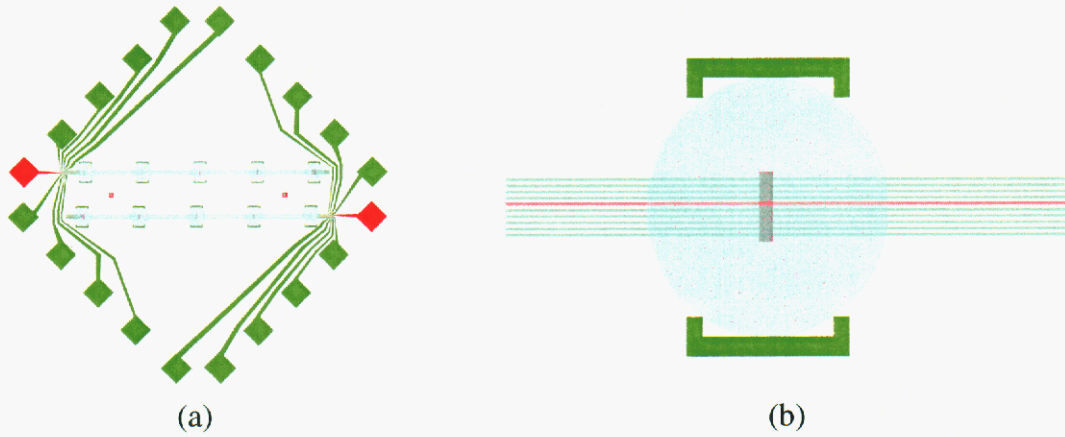


Figure 5 (a) Al lines layout. (b) Magnified view of experimental area showing 9 Al lines, 1 Cu line and opening in SiO₂ layer for electrolyte exposure.



Figure 6 (a) Top capacitor plate for measuring solution resistance as a function of RH. (b) Bottom capacitor plate for measuring solution resistance as a function of RH.

2.3 Foil and wire based electrodes

2.3.1 General construction techniques

The majority of the electrodes used in this program were constructed by stacking two or more electrically isolated metal foils, mounting in an epoxy compound and polishing the face to expose the foil edges in cross-section. A schematic of the basic foil electrode is shown in Figure 7. Electrodes were assembled by preparing and coating the foils, making electrical connections, potting the electrode then polishing the exposure surface. Foils were typically 25 μm thick and cut to widths from 1 to 2 cm.

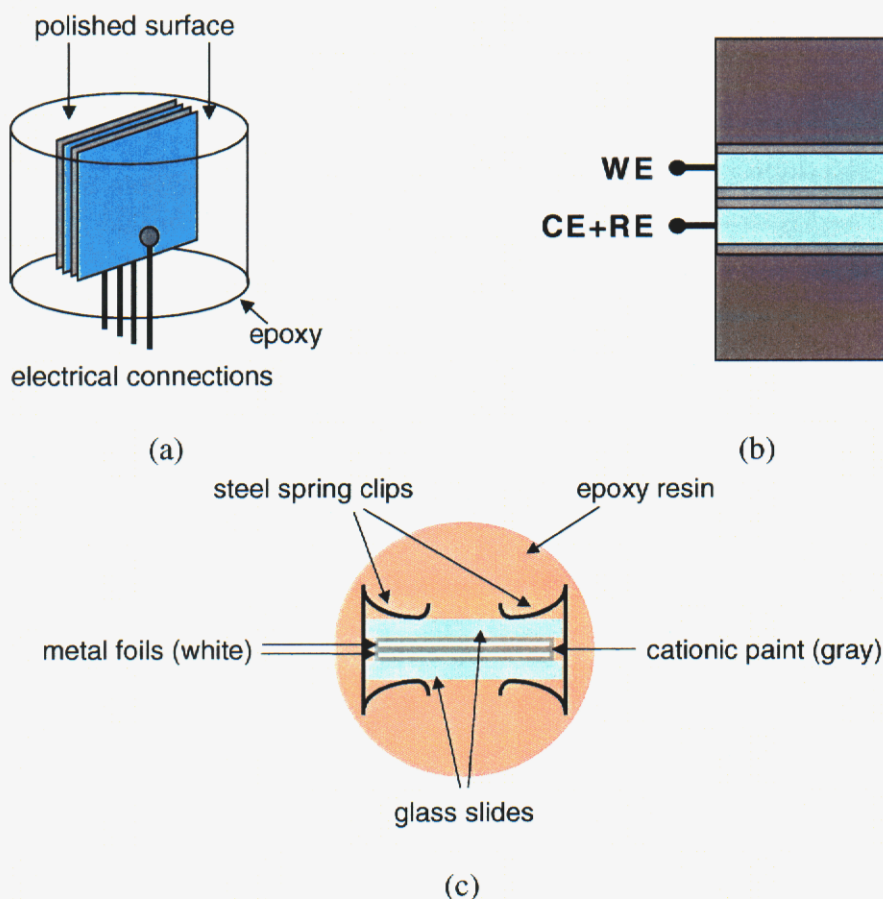


Figure 7. Schematic representations of the stacked foil electrode. (a) Overall view of electrode layout, (b) Cross-section demonstrating high degree of electrode overlap that leads to high capacitance and low Z_{para} , (c) Exposed face of sample showing the minimized inter-electrode spacing and maximized surface area for decreasing R_s and R_p .

The foils were coated with an insulator prior to assembling the electrode. The insulating material serves to assure electrical isolation between the foils and at the same time must have good adhesion to the foils to prevent the formation of crevices where moisture and contaminants can accumulate. Initially, electrodes were prepared using a variety of insulating materials including electroplating tape and thin polymer sheets. Although these materials provide adequate insulation they do not adhere to the electrode and are not suitable. The best insulator was found to be an electrochemically applied electrophoretic paint. Specifics of the paint and how it is applied can be found in Appendix A. The paint was applied such that approximately 1 cm of foil was left exposed at one end for making electrical contact. Benefits of this coating are reproducible and controllable coating thickness, uniformity of application, good adhesion to a variety of metals, high resistivity and excellent corrosion resistance. A limitation of the paint when applied in very thin coatings (as was the case in this work) is that it did not adhere to the sharp, cut edges of the foils. The impact of this behavior is that foils cannot be laid up in a configuration where the edges of the foils are in registry. If the edges come into contact and pressure is applied to the stack of foils, an electrical short can occur between foils. To prevent this problem foils were staggered so that edges did not overlap, or, in some cases, foils were cut to different widths such that one foil sat completely within the boundaries of its neighboring foil.

Once coated, the foils were assembled into a stacked arrangement with glass slides on the outsides of the stack. The stack was held together using steel spring-clips. The non-coated end of the foils extended beyond the glass slides such that electrical connections could be made after potting. The samples were potted in 2.54 cm diameter molds with an epoxy-based resin. After curing, insulated wires were soldered to the exposed foil surfaces. Polymeric insulators were inserted between the electrical connections to maintain electrical isolation. The epoxy was then extended in a second potting step to cover the solder connections and provide mechanical strength.

The electrode surface was mechanically polished to expose the edges of the foils. Nominally either 4000 grit SiC polishing paper or a 0.05 μm diamond paste was used as the final polishing step. Care had to be taken to avoid smearing the metal during the final polishing step. Small metal “fingers” were prone to shorting the parallel foils, especially when the inter-electrode separation was small (i.e., less than 20 μm). When the 4000 grit SiC was used as the final polishing step, the foils were directionally polished such that the grinding motion was parallel to the foil edges and making it less likely that smearing would cause a short between foils. When 0.05 μm diamond was used as the final polishing step, directional polishing was not required as smearing was minimized due to the fine particle size of the polishing medium. The ends of the foils were masked off using Microstop™ such that approximately the same length of each foil was exposed.

In addition to the stacked foil electrodes, additional electrodes were constructed by placing a foil and a wire in close proximity. Two variations of the foil-wire electrode were generated (Figure 8). The first type had the axis of the wire running parallel to the polished surface of the sample such that the exposed area was maximized (this is referred to as a bent-wire electrode). The second type had the axis of the wire running parallel to the long direction of the foil such that when polished the wire was exposed in cross

section (referred to as a straight-wire electrode). For both electrode types, the wire and foil were coated with electrophoretic paint to provide an insulating layer.

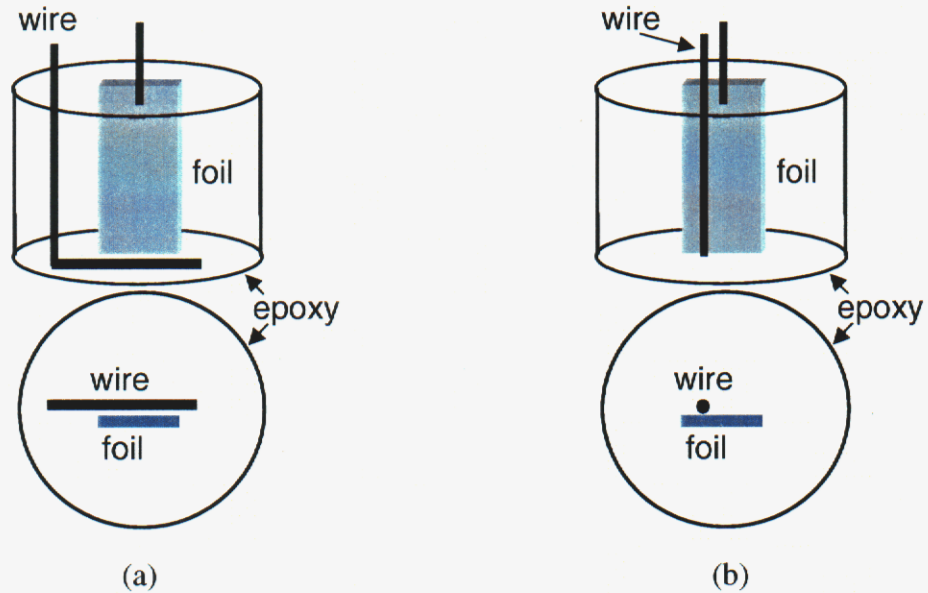


Figure 8 Schematic representation of foil-wire electrodes: (a) Bent-wire electrode used for maximizing Z_{para} while minimizing R_p and R_s . (b) Straight-wire electrode used for exposing a restricted surface area for localized corrosion experimentation.

The bent-wire electrodes were constructed using 250 μm diameter aluminum wires. After mounting in epoxy, the electrode face was polished such that the maximum area of wire was exposed. This condition corresponds to the point of closest approach between the wire and the foil electrode. This arrangement yields a large sample area while minimizing inter-electrode separation and minimizing electrode overlap. The result is an electrode with higher impedance than the foil-foil arrangement, but with the same characteristics as far as resolving R_s and R_p . The disadvantage to this electrode is that it cannot be repolished, because to do so would change the cross-sectional area of the wire and increase the separation between the wire and foil.

The straight-wire electrodes were constructed using 25 μm diameter aluminum wires. This configuration was used for studying localized corrosion initiation under atmospheric conditions. The small diameter electrode restricts the area where corrosion damage can occur. The large surface area of the foil is used to supply current to the system. Thus, this electrode can be used to studying the response of the wire to an externally imposed current or potential.

2.3.2 Specific electrode types and applications

2.3.2.1 Al foil electrodes

Al foil electrodes were constructed by parallel arrangement of 25 μm thick, 99.99% pure Al foils. These electrodes were used for studying the atmospheric corrosion response of Al and for assessing the sensitivity of a parallel foil electrode to varying levels of RH.

2.3.2.2 Cu foil electrodes

Cu foil electrodes were constructed by parallel arrangement of 25 μm thick, high purity Cu foils. These electrodes were used for assessing the applicability of electrochemical techniques to measuring uniform attack at high RH and in the presence of either $\text{Cl}_{2(\text{g})}$ or $\text{H}_2\text{S}_{(\text{g})}$

2.3.2.3 Al foil-Cu foil electrodes

Two-layer and multi-layer Al foil-Cu foil electrodes were constructed by parallel arrangement of 25 μm Al and Cu foils. These electrodes were used to measure galvanic current flow between Al (anode) and Cu (cathode) under atmospheric conditions. The electrodes were used to assess the sensitivity of electrochemical measurements to galvanic corrosion as a function of RH and contaminant level. They were also used to measure both uniform and localized attack on the Al due to the galvanic coupling. In an effort to amplify the electrochemical signals, multi-layer Al foil-Cu foil samples were constructed where the total electrode area was the sum of all of the individual foils (Figure 9a). Since the current is proportional to the surface area, increasing the number of foils should result in a proportional increase in corrosion current. Multi-layer electrodes were also constructed to study the effect of inter-electrode distance and current distributions. In some cases multiple Al electrodes were arranged around a central Cu electrode (Figure 9b). In other cases multiple Cu electrodes were arranged next to an Al electrode (Figure 9c).

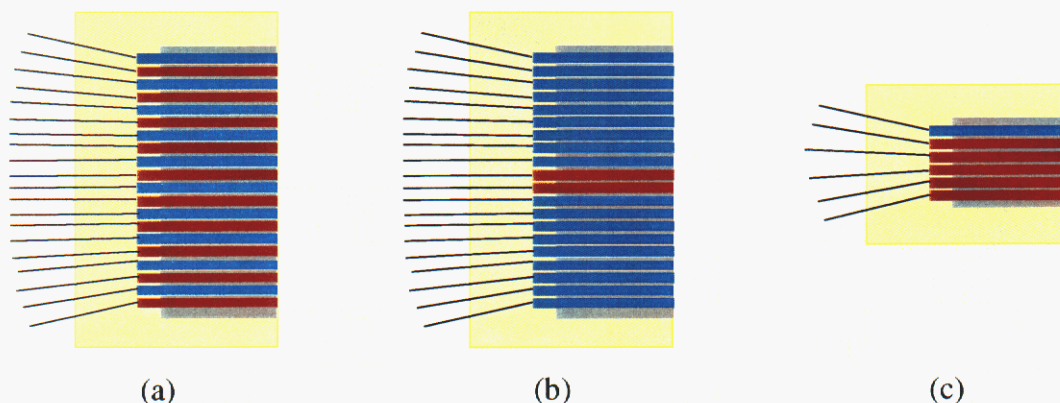


Figure 9 Examples of multi-layer electrode layouts: (a) Alternating Al and Cu foils for maximizing corrosion current signal. (b) 10 Al electrodes on either side of 2 central Cu electrodes. This electrode was intended for measuring the propensity for corrosion initiation as a function of distance from the Cu layers. (c) 5 Cu electrodes next to a single Al electrode. This configuration was intended for studying the galvanic current as a function of separation between the coupled materials.

2.3.2.4 Al foil-Au foil and Al foil-Pt foil electrodes

Multi-layer electrodes were constructed from Al and either Pt or Au in an effort to make standard 3-electrode electrochemical measurements under atmospheric conditions. The basic scheme is to locate the working electrode (in this case Al) between two layers of a noble material. One foil of the noble material is used as the counter electrode and supplies current to the working electrode. The other noble metal foil is used as a pseudo-reference electrode and is used as a reference point for either measuring or controlling the potential of the working electrode. However, according to González a simple 3-electrode configuration results in the pseudo-reference electrode experiencing an asymmetric field that can cause errors in the potential measurements¹². The asymmetric field can be avoided by using a 5-electrode configuration (see Figure 10). Two 5-electrode sensors were constructed. One had Au foils for the counter and reference electrodes; the other had Pt foils for these electrodes. Difficulties with electrical shorting between foil layers limited the utility of these electrodes. It is possible that the electrophoretic paint did not adhere to the Au and Pt as well as it did to the Al and Cu.

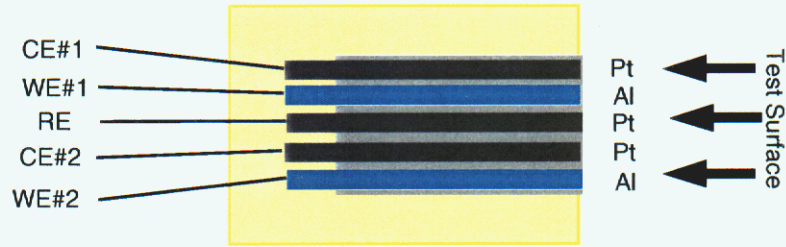


Figure 10 Adaptation of conventional 3-electrode system for atmospheric testing. The 5-layer electrode layout is intended to prevent induced fields in the central reference electrode

2.3.2.5 Cu-coated Al foil electrodes

A well-controlled system was desired that would undergo exacerbated corrosion on each electrode in order to study the electrochemical behavior of an active system under atmospheric conditions. It is well known in the Al-Cu system that corrosion preferentially initiates at Cu-rich secondary phases¹³; therefore, it was anticipated that corrosion would occur at an artificial Al-Cu interface. A procedure was developed for plating Cu onto Al without a strike layer – the details of this process can be found in Appendix B. Al foils of 25 μm thickness were plated with approximately 14 μm of Cu then coated with electrophoretic paint. A schematic cross-section of this electrode is shown in Figure 11. Assuming that corrosion will preferentially initiate at the Al-Cu interface, this electrode should exhibit a much higher average corrosion rate than the Al foil electrode or the Cu foil electrode described above. Thus this electrode serves as an extreme case (high corrosion rate) for evaluating sensitivity of the atmospheric corrosion measurements. It was also used to compare the morphology of corrosion attack that evolves under atmospheric and aqueous conditions.

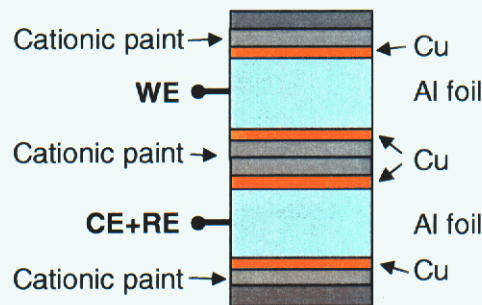


Figure 11 Cu-coated Al foil electrode.

2.3.2.6 Pd foil electrodes

A Pd foil electrode was constructed with the objective of minimizing the inter-electrode spacing but maximizing the electrode impedance. This electrode was intended

as a probe for quantifying R_s . The Pd foils should be inert in the environments studied in this program and thus provide a stable system for studying R_s as a function of RH and contaminant level. The electrode was constructed as shown in Figure 12 with the foils arranged at an angle to maximize separation at all points other than at the exposed electrode surfaces.

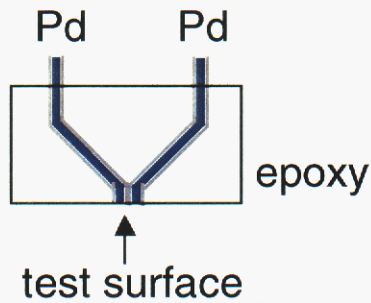


Figure 12 Layout of Pd foil electrode. The foils are separated in order to minimize the capacitance of the electrode.

3 CORROSION TESTING

3.1 Introduction to corrosion testing

The underlying goal of the corrosion testing was to determine our ability to resolve electrochemical phenomena under atmospheric conditions by combining sensitive measuring equipment with specially fabricated corrosion probes (previous section). A subset of the experimentation was performed under inundated conditions. These tests were usually targeted at assessing the performance of a probe design under well-defined conditions. Inundated conditions were also used when determining the baseline behavior of multi-layer electrodes tested in conjunction with a multi-channel potentiostat. The majority of the experiments were carried out in atmospheric environments with controlled humidity, temperature and contaminant concentration. The goals of these experiments were to:

- (1) Determine RH levels where corrosion could be measured and quantified.
- (2) Differentiate between corroding systems (e.g., passive, uniform corrosion, localized active dissolution) under fixed environmental conditions.
- (3) Determine the RH levels where localized corrosion can be induced in Al electrodes through external polarization.
- (4) Determine the sensitivity / applicability of various test techniques (impedance spectroscopy, galvanic current measurement, polarization testing, open circuit measurements, etc.) to detecting corrosion under atmospheric conditions.
- (5) Evaluate the ability to characterize the conductivity of the adsorbed electrolyte (R_s measurements) by minimizing electrode impedance (Z_{para}).
- (6) Measure the interfacial impedance (expressed as R_p) and the solution resistance (R_s) as a function of RH.
- (7) Measure the reversibility of water adsorption on electrodes by humid / dry cycling.
- (8) Determine the propensity for localized corrosion initiation on aluminum microelectrodes.

In the next two sections the test apparatus and the electrochemical techniques used in this work are described in detail. Then the results are presented for each of the electrode types developed in this work.

3.2 Experimental set-up: Atmospheric test chamber

The ability to specify the temperature, relative humidity (RH) and contaminant level (e.g., concentration of $\text{Cl}_{2(g)}$) was critical to performing a quantitative evaluation of electrochemical techniques under atmospheric conditions. In order to achieve this experimental objective, a dedicated gas exposure system (GES) configured with electrochemical measurement capability was constructed. The basic schematic outline of an exposure system is shown in Figure 13. The actual GES contained two duplicates of the system shown in the figure.

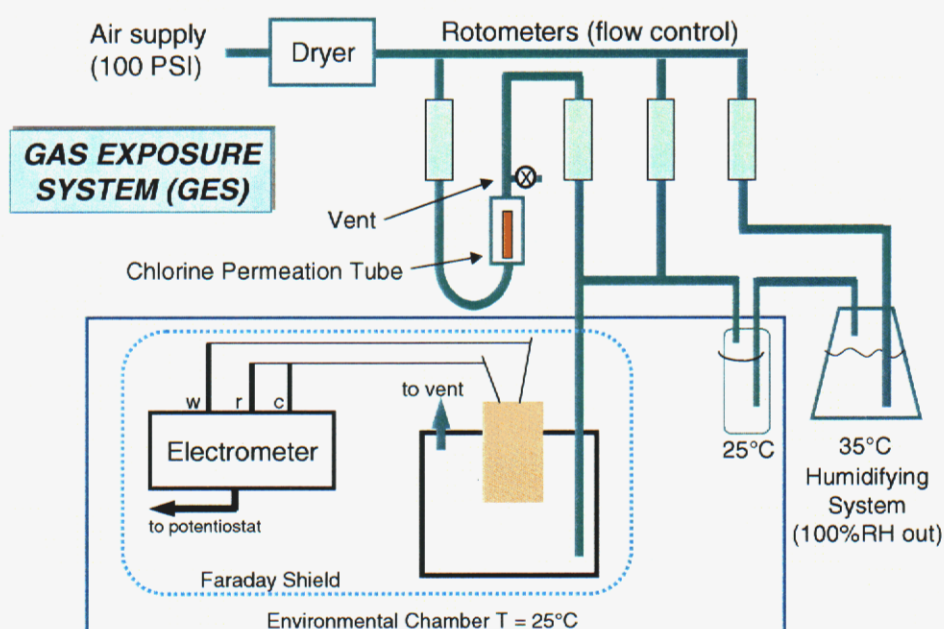


Figure 13 Gas exposure system (GES). Controlling flow rates and combining flows from a contaminated air stream, a dry air stream and a humid air stream allows the contaminant level and relative humidity to be specified. Enclosing the test system in an environmental chamber allows the test temperature to be specified as well.

The operation of the GES is based on mixing flows from several well-defined gas streams to yield a final gas mixture having the desired RH and composition. The first parameter to be determined is the desired flow rate through the test chamber. Once this is known, the various feed streams can be determined such that their sum equals the total desired rate. Dry air flows through both the perm-tube (to pick up the desired contaminant) as well as through a dedicated dry air line. The total dry air flow is balanced against a humid air stream to give the desired relative humidity. The air in the humid air stream is passed through a saturator at a slightly elevated temperature (e.g.,

40°C) to yield approximately 100% RH in the air stream. The two dry air lines are balanced against one another to yield the desired contaminant level. The contaminant concentration in the contaminated air line is determined by the flow into the perm-tube, the permeation rate of the perm-tube and the flow rate out of the perm tube. A bleed-off valve is used in conjunction with a rotometer to regulate the flow of the contaminated gas from the perm-tube. Because this system was operated significantly above sea level (Sandia National Laboratories, Albuquerque, NM), all flow rates were adjusted to yield the equivalent delivery of moles per second of species to the exposure chamber as would be delivered if the tests were run at sea level.

In general, it was possible to control RH between approximately 0% (no humid line connected) and approximately 85%. The upper bound is likely due to condensation in various portions of the test system. The only contaminant used in the GES system was $\text{Cl}_{2(g)}$. Concentration was controlled at target levels of 0, 20 ppb, 200 ppb and 300 ppb.

In order to run low-current electrochemical measurements it was necessary to provide Faraday shielding for the test chamber and the electrometer connected to the potentiostat. Simple and effective shielding was achieved by wrapping the various components (test chamber, electrode leads and electrometer) in multiple layers of aluminum foil. The foil was grounded to both an earth ground and to the grounding pin on the electrometer.

Some of the initial atmospheric experiments were run in a controlled humidity bell-jar. In these experiments both temperature and humidity were controlled. No intentionally added contaminants were used in these experiments and there was no Faraday shielding.

3.3 Electrochemical equipment and techniques

3.3.1 Potentiostats

Although the design of the electrode is of paramount importance to making successful atmospheric electrochemical measurements, the electronic instrumentation is equally critical. The basic piece of equipment for running traditional electrochemical experiments is the 3-electrode potentiostat. The potentiostat has three connections to an electrochemical cell: the working electrode (WE), the counter electrode (CE) and the reference electrode (RE). The potentiostat is used to either (1) measure the potential of the WE vs. the RE, (2) measure the current flow from the CE to the WE that is required to polarize the WE to a specified potential vs. the RE, or (3) measure the potential difference between the WE and RE when a specified current is passed between the CE and the WE. The critical specifications of the potentiostat are thus the input impedance, the leakage current through the RE, and the precision with which current and potential can be measured and controlled. Three commercially available potentiostats were used in various phases of this program. They are briefly described below.

The first potentiostat used was a Princeton Applied Research model 283 in conjunction with a Solartron HF1255 frequency response analyzer (FRA). In this configuration the FRA is used during electrochemical impedance spectroscopy (EIS) measurements in which an AC potential waveform is applied and the resulting phase and magnitude of the current response is monitored. The 283 potentiostat was experimentally found to have a low-frequency impedance limit of approximately 10^{10} ohms when run without a test structure connected to the potentiostat leads. The implication of this limit is that electrochemical systems with higher impedance cannot be measured.

A Scribner Associates Multi-Microelectrode Analyzer (MMA) was used to measure currents in multi-electrode systems. The MMA has the capability to measure up to 100 individual current signals with a resolution of approximately 30 pA. It is also possible to configure some of the measurement channels as electrometers such that multiple potential measurements can be made simultaneously. While extremely useful for making measurements in inundated environments, the MMA lacked the current resolution to make sensitive atmospheric measurements in low humidity environments.

The potentiostat that was eventually selected for making the majority of the atmospheric measurements was the Gamry Instruments FAS-1 Femtostat. This instrument has an experimentally determined low-frequency impedance limit of at least 10^{12} Ohms. The voltage control/measurement resolution was found to be approximately 10^{-4} V and the current control/measurement resolution is on the order of 10^{-14} A. This represents excellent sensitivity to low amplitude electrochemical signals. By comparison, many standard corrosion experiments involve currents in the range of 10^{-8} to 10^{-3} A. Two Femtostats were incorporated into the GES system, one for each exposure chamber.

3.3.2 Electrochemical measurements applied to atmospheric testing

3.3.2.1 Open circuit measurements

Open circuit measurements were occasionally used to determine if a “realistic” potential could be measured between electrodes. The parameter measured with this technique is termed the open circuit potential (E_{oc}) and has the units of Volts. For atmospheric probes having two electrodes of the same material, the potential difference is ideally zero volts. For two dissimilar metals, the more noble material should be at a higher potential than the less noble material. For instance, a positive value should be measured if the potential of Cu is measured with respect to Al. The open circuit measurement is inherently passive, as the input impedance of the reference electrode circuit in the potentiostat is ideally infinite. In practice, however, the true E_{oc} value can be obscured when stray electric fields act to impart a charge to either the electrode or the potentiostat cables. It was generally observed that at low RH reliable open circuit measurements could not be made due to the charging effect.

3.3.2.2 Potentiostatic experiments

Potentiostatic polarization experiments were used to study the induction time for localized corrosion (i.e., pitting) of Al under various atmospheric conditions. In this experiment a fixed potential is applied between electrodes and the resulting corrosion current is monitored. It was found that as the RH was lowered, very high potentials had to be applied and maintained for extended periods of time before localized corrosion initiated. The limiting factor in making potentiostatic polarization measurements is R_s . At low humidity the magnitude of R_s can be comparable to R_p . When a potential is applied between electrodes, a large portion of the potential drop occurs across R_s and the effective polarization of the working electrode is only a fraction of the total applied potential.

3.3.2.3 Galvanic current measurements

Galvanic current measurements are a special case of the potentiostatic measurement. In this experiment the potentiostat is used to short the electrodes together, acting as a very low impedance ammeter, and measure the resulting current. For probes having two electrodes of the same material the average galvanic current should be zero (because the electrodes have nominally the same E_{oc} , shorting them together will not cause current flow). Most of the galvanic current measurements in this program were made between Al and Cu. Because Cu is more noble than Al, a positive current should flow from the Al to the Cu, i.e., the Al is oxidized (giving up electrons) and the Cu supports reduction reactions (consuming electrons). The galvanic current measurements made between Al and Cu using the Femtostat potentiostat were found to be extremely sensitive to atmospheric conditions for all environments investigated. It was possible to resolve changes in current at very low RH, with or without the presence of a contaminant gas. The data from the galvanic current measurement reflect both the background or average corrosion rate of the more active material, and provide an indication of the magnitude of any localized corrosion. The galvanic current measurement is extremely sensitive to localized attack because the background current in atmospheric systems is inherently low. Thus the signal to noise ratio for localized events can be much higher than is observed for comparable systems under inundated conditions.

3.3.2.4 Potentiodynamic experiments

In potentiodynamic experiments a potential field is applied to the sample and is ramped at a fixed, linear rate. For Al electrodes exposed to a halogen contaminant in the presence of moisture, a potential will be reached which causes a sudden increase in the corrosion current. The increase in current is due to localized attack of the Al, usually pitting, and the potential at which attack initiates is termed the pitting potential (E_{pit}). Potentiodynamic experiments were used in an attempt to assess the relationship between E_{pit} and RH. However, the Femtostat can only apply 3.6 V in a controlled-potential experiment and it was found that this potential was insufficient to initiate pitting at low

RH. Potentiostats capable of applying higher potentials do not have the requisite current resolution to detect pitting at low RH.

3.3.2.5 Galvanodynamic experiments

The galvanodynamic experiment is similar to the potentiodynamic experiment, except the current, instead of the potential, is the controlled variable. The current is ramped at a fixed, linear rate between an initial current and a final current and the resulting potential is measured. Localized attack results in a rapid decrease in the measured potential. This is due to active metal being exposed when the oxide is locally disrupted. In a galvanodynamic experiment, a pit usually grows until it requires more current than is being supplied by the potentiostat, then the pit repassivates. The potential then climbs again until pitting resumes. The sample continues to corrode in this fashion, undergoing a sequence of pitting and repassivation steps until a sufficient current is reached that can support continued pit growth. One advantage of the galvanodynamic experiment over the potentiodynamic experiment, when run with the FAS-1 Femtostat, is that higher potential fields can be probed. This stems from the instrument design, which allows higher potentials to be measured than can be controlled. The Femtostat is capable of measuring a potential of approximately 11 V vs. RE whereas it is only capable of controlling 3.6 V vs. RE.

3.3.2.6 Electrochemical Impedance Spectroscopy

Electrochemical impedance spectroscopy (EIS) is generally a non-perturbing experiment that gives information on both the interfacial reactions between the WE and the environment and on the resistance of the environment. EIS is typically performed by applying a low-amplitude, sinusoidal AC potential waveform and measuring the resulting current waveform. The amplitudes of the voltage and current as well as the phase shift between the two waveforms are used to characterize the electrochemical system. Measurements are made across a range of applied frequencies (e.g., 10^{-3} to 10^5 Hz). High frequency data is generally interpreted as the solution resistance (R_s) of the environment and the low frequency data is generally interpreted as the sum of R_s and the polarization resistance (R_p). R_p can be used to calculate the average corrosion rate of the material. Complications arise in using EIS under atmospheric conditions due to the extremely high impedance of the electrochemical system. When the system impedance is on the same order as the instrument impedance or the parasitic impedance (Z_{para}) of the electrode, it can become difficult to extract the desired information from the EIS signal. All of the electrodes used have a capacitive component that manifests itself as a low Z_{para} at intermediate to high frequencies. Thus, at low RH, R_s can be greater than Z_{para} , making it impossible to extract a value for R_s . Another troubling situation can arise if R_s is much greater than R_p . In this case, the low frequency impedance will be dominated by R_s and extracting R_p becomes inaccurate, because it requires calculating a small difference between two large values.

3.4 Results

3.4.1 Al / Cu / Pd Multi-electrode

A series of multi-electrodes were fabricated to assess the feasibility of making spatially resolved measurements of both current and potential. Although the ultimate goal of this line of research is to quantify electrochemical gradients under atmospheric conditions, the scoping experiments performed in this work were all performed under aqueous conditions. Figure 14 shows the basic layout of the thin-film multi-electrode. The central electrode is Cu and the 12 outer electrodes are Al. Reference electrodes are arranged along two dimensions between the Cu and the Al and were intended to provide a spatially resolved measure of the potential fields that develop between the dissimilar metals. In the first fabrication run the reference electrodes were made from Au, later the material was switched to Pd.

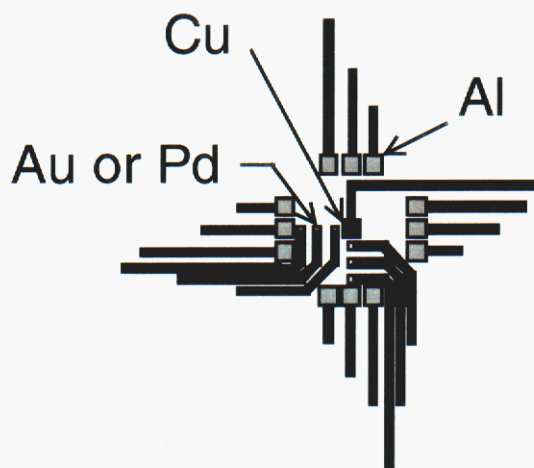


Figure 14 Thin-film multi-electrode. Current flow is monitored between the central Cu electrode and the 12 surrounding Al electrodes. Either Au or Pd reference electrodes are used to measure the potential field as a function of position.

The functionality and consistency of the Al, Au, Pd and Cu thin-film electrodes incorporated in the micro-electrochemical cell were assessed using open circuit measurements (Figure 15) and EIS testing (Figure 16). Open circuit data for the three materials are consistent with previous measurements made on bulk samples of similar materials. Additionally, the open circuit values are reproducible from electrode to electrode and fall within typical scatter bands for this parameter. EIS testing in a benign environment indicated relatively good consistency between Al samples with only a few outliers. The Au electrodes were intended to provide reference electrochemical potentials and were effectively used during short-term electrochemical testing; however, the reduced area Au interface was too polarizable for long term stability. In a subsequent sample, the Au was replaced with Pd, which had much better stability. Difficulties may

have also been encountered with stability due to the leakage current through the RE circuitry of the potentiostat. Stability measurements were made using the PAR 283 instead of the FAS-1 Femtostat, because the Femtostat was not available during this portion of the program. It is certainly possible that better behavior could result from using a higher-impedance potentiostat.

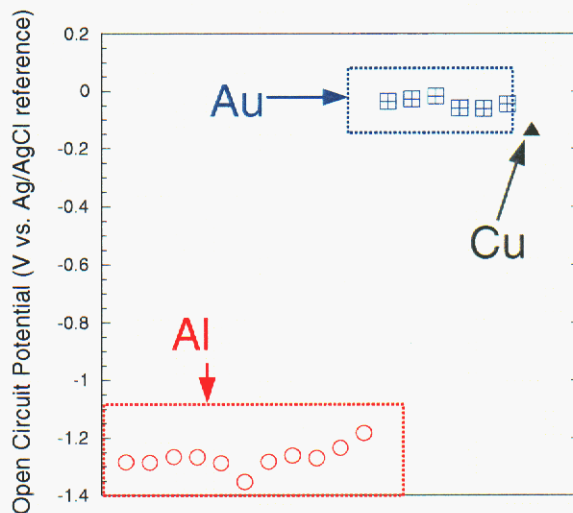


Figure 15 Open circuit measurements for the thin-film multi-electrode. Experiments were run in aerated 0.05 M NaCl. Measured values were consistent among electrodes of the same material. The values obtained for the thin film micro-electrodes are similar to those observed on bulk materials in this environment.

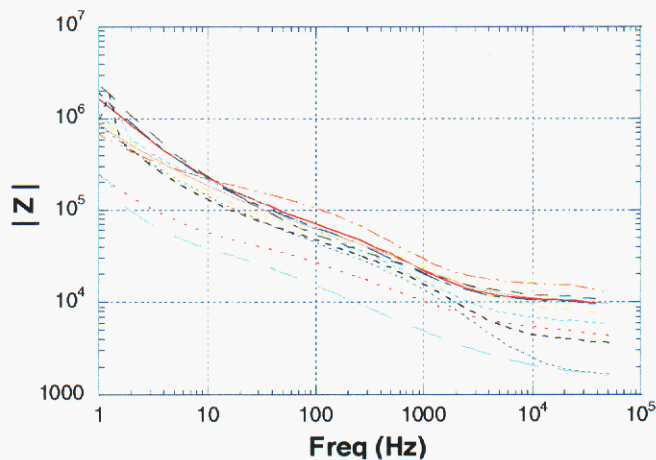


Figure 16 EIS data for 11 Al electrodes in Na₂B₄O₇ buffered to pH 7.0. EIS spectra demonstrate consistency of electrode behavior.

To test the capability to simultaneously measure potential and current information, the 19-electrode device was connected to the MMA potentiostat. Channels connected to the Al and Cu electrodes were configured for measuring current flow, while channels connected to the Pd electrodes were configured for measuring potential vs. the Cu electrode. A typical experiment consists of placing a droplet of test solution and monitoring the system response (Figure 17).

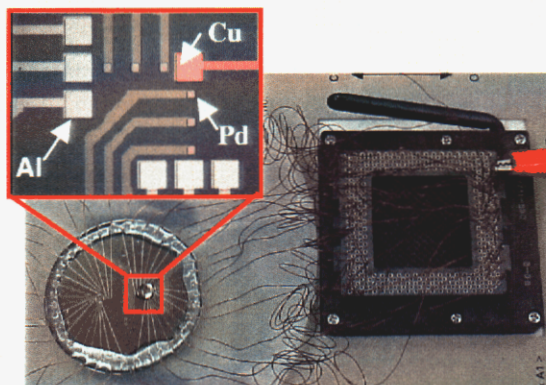


Figure 17 Experimental set-up for testing the thin-film multi-electrode. The electrode is connected to the MMA via a Pentium chip carrier. The enlarged image does not show the other 6 symmetric Al electrodes.

The basic functionality of the system was evaluated by using deionized H_2O as the test medium. This environment was chosen in order that galvanic currents could be measured without causing pitting of the Al. Figure 18 shows the response when solution is placed on the electrode surface. The Al electrodes are anodically polarized and show passive corrosion behavior. The Cu is cathodically polarized and supports reduction reactions. The Pd electrodes all measure similar, noble potentials. The data for the Al indicate very little current flow and no evidence of localized attack.

The system was tested under corroding conditions by using 0.05M NaCl solution as the test environment (Figure 19). The data indicate mostly passive corrosion of the aluminum nodes except for a brief period of metastable pitting and a period of more extensive pitting at the end of the experiment. The elevated currents observed while the solution dries out are due to (1) increased concentration of Cl^- in the electrolyte, (2) and possibly decreased diffusion distance for O_2 to reach the Cu electrode.

Experiments were not run under atmospheric conditions using this electrode. Tests on Al and Cu foil electrodes indicated that the MMA potentiostat was not sensitive enough to measure the expected currents under atmospheric conditions. Furthermore, the separation of electrodes on the thin-film sample was approximately $850 \mu m$, and experimentation on foil-based electrodes indicated that separations on the order of $50 \mu m$ or less are required to make sensitive atmospheric measurements. The functionality of

the multi-electrode under aqueous conditions does, however, demonstrate the feasibility of the concept of making spatially resolved atmospheric measurements. Future endeavors along this line should be based on making samples with smaller inter-electrode spacing and possibly implementing more sensitive potentiostats.

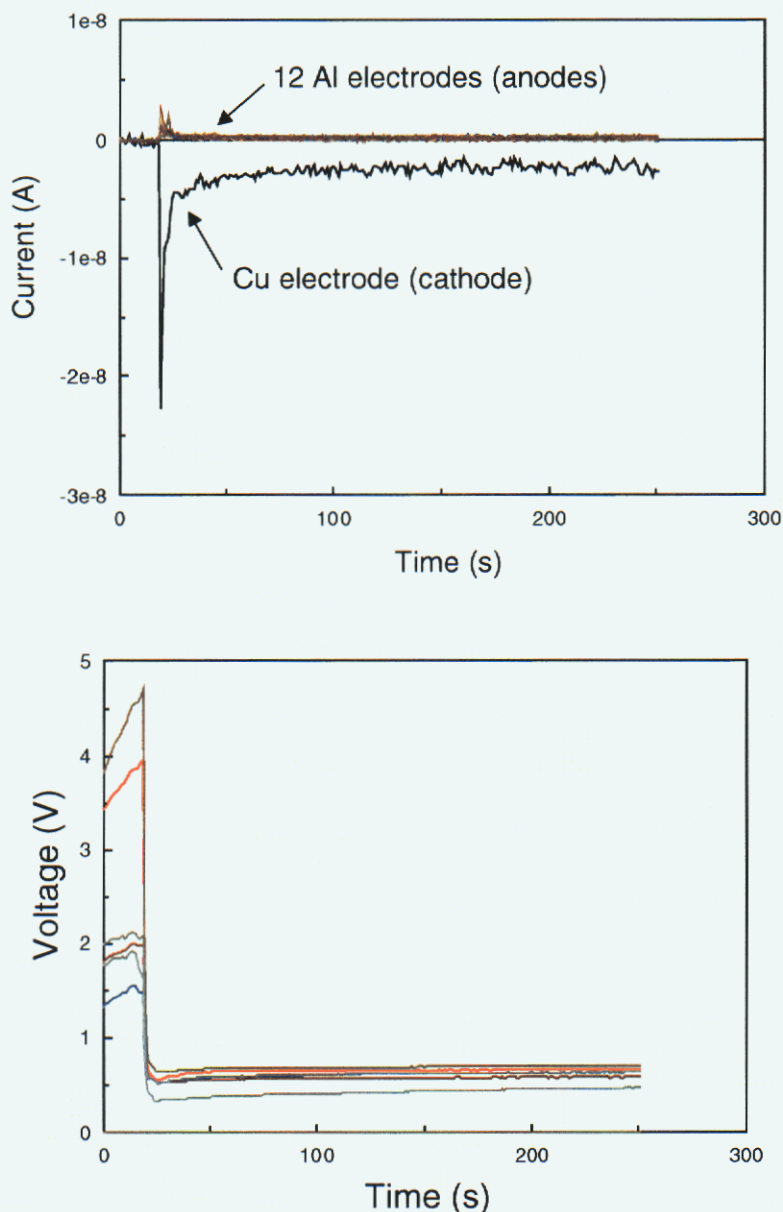


Figure 18 Response of thin-film multi-electrode in deionized H_2O (current, top graph and potential, bottom graph). A droplet of water was placed on the electrode surface at $t = 11$ sec. The data indicate general corrosion of the Al (no localized corrosion such as pitting) and cathodic polarization of the Cu.

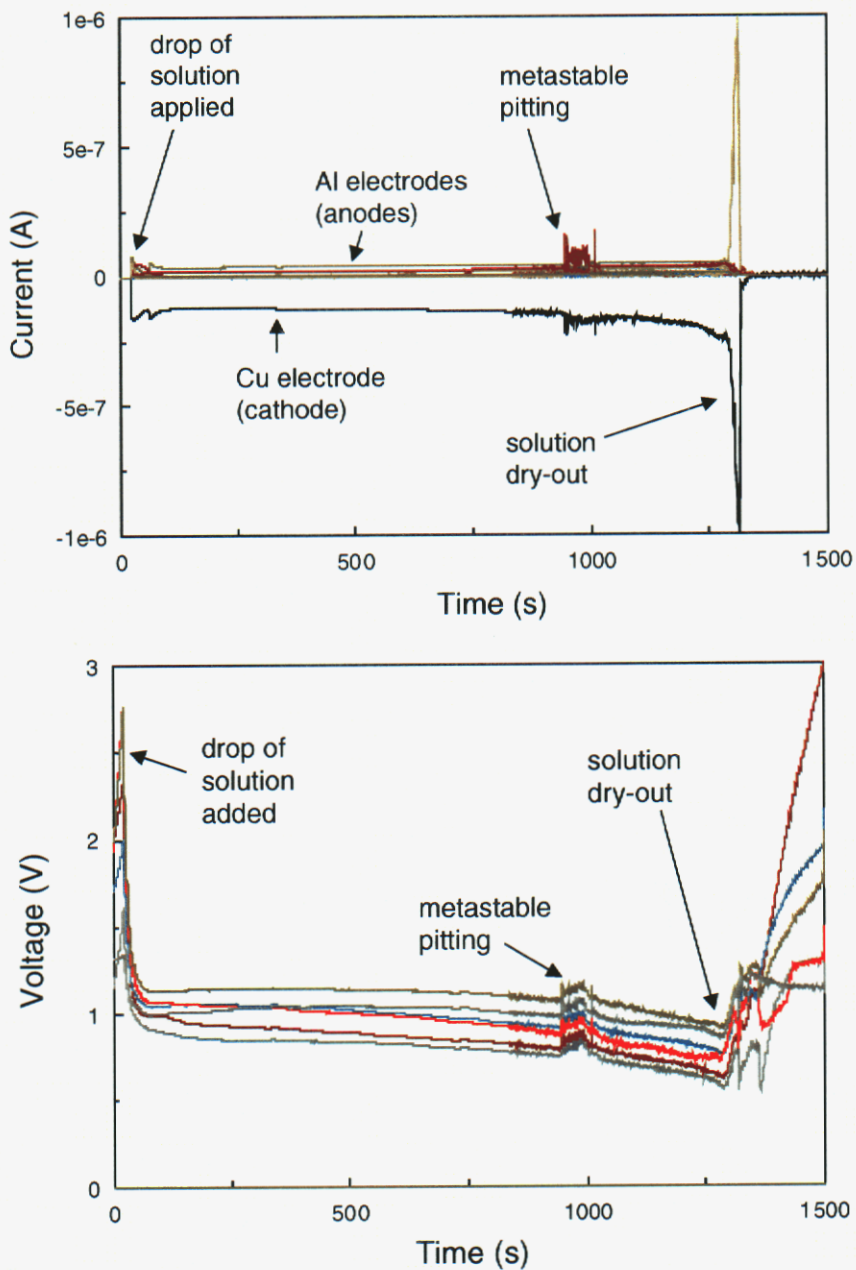


Figure 19 Response of thin-film multi-electrode in 0.05 M NaCl (current, top graph and potential, bottom graph). A droplet of solution was placed on the electrode surface at $t = 23$ sec. The data indicate general corrosion of the Al until $t = 950$ sec where metastable pitting of one Al electrode begins. At $t = 1290$ sec the electrolyte begins drying out, resulting in exacerbated corrosion of one of the Al electrodes.

3.4.2 Interdigitated Pt Fingers

Thin-film Pt electrodes were fabricated to determine the feasibility of using thin-film electrode structures to make EIS measurements under atmospheric conditions. The electrodes consisted of interdigitated fingers that were either 200 μm long with 100 μm spacing or 100 μm long with 200 μm spacing. The electrode was initially tested in 0.05 M NaCl solution (25°C) to determine if any artifacts were apparent in the data due to the long edge length to surface area ratio. A 10 mV AC perturbation was used. A disk-shaped area of deposited Pt was tested as a control. The data (Figure 20) demonstrate that the Pt electrodes yield the same shape of impedance data independent of edge-length to surface area ratio. Differences in the data shown correspond to the differences in electrode areas.

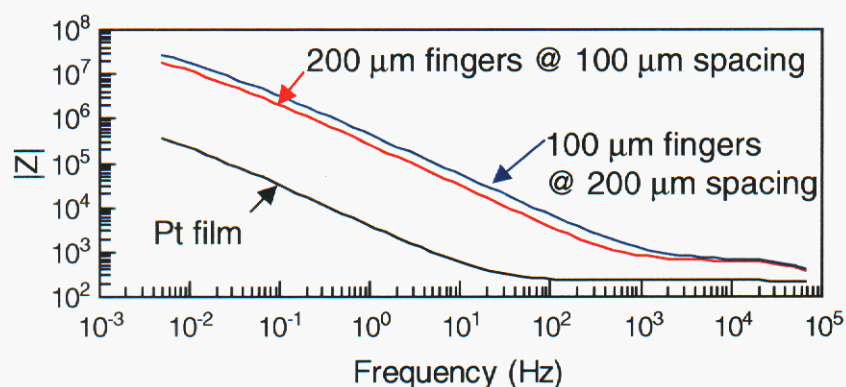


Figure 20 Interdigitated Pt electrodes and thin-film Pt control electrode tested in 0.05 M NaCl solution at 25°C. The shifts in impedance between the electrodes are due to differences in electrode area.

The electrodes were also tested under atmospheric conditions. The test was performed inside a controlled temperature and humidity bell jar. No contaminants were intentionally added to the environment or to the sample face. Once again, EIS was collected using a 10 mV AC signal. The 283 potentiostat was used to run these experiments. Figure 21 shows the response of the Pt fingers with 100 μm spacing as a function of RH and temperature. At 85% RH increasing the temperature from 40°C to 60°C results in a decrease in impedance at intermediate frequencies, indicating a decrease in R_s . This observation corresponds to an increase in ionic conductivity in the adsorbed moisture layer with increasing temperature. Decreasing the RH from 85% to 60% results in an increase in impedance and degradation in the quality of the signal. There is a practical limitation to the RH limits that can be probed with this combination of electrode design and potentiostat type. Even at 60%RH the data are approaching the response of the system when run without a sample connected to the potentiostat leads. Once the impedance of the electrochemical system exceeds the instrument impedance, the sample will no longer provide useful information. Thus, the interdigitated Pt electrodes appear

suitable for making measurements at high RH (greater than 60%) but are not promising for making measurements in low RH environments.

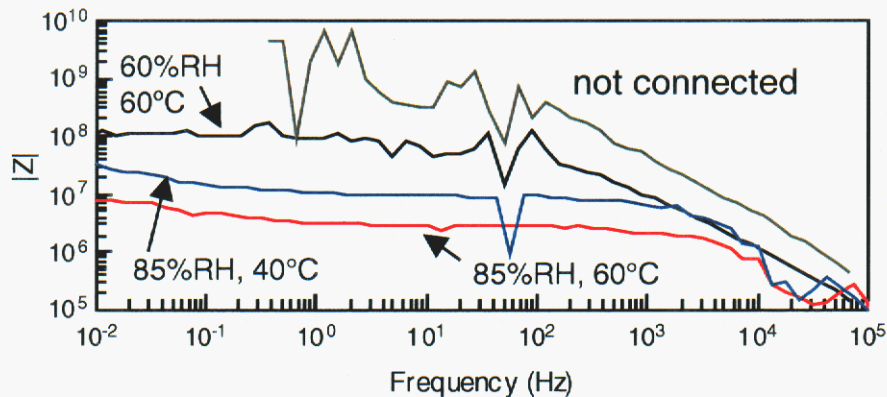


Figure 21 Pt interdigitated electrodes tested under atmospheric conditions. No contaminants were added to the system.

3.4.3 Au / Au EIS Electrode

One of the goals of this research program was to be able to make electrochemical measurements of R_s under atmospheric conditions. While, in theory, any electrode pair can be used to measure R_s values, there are practical limitations that can only be overcome by careful electrode design. Importantly, the electrodes must be constructed from an inert material such that corrosion reactions are impeded and $R_p > R_s$. Also, the parasitic capacitance of the electrode (Z_{para}) must be minimized to avoid masking the R_s value. To accomplish these goals an electrode was constructed consisting of parallel Au traces in close proximity with minimal overlap of cross sectional area.

The Au-Au electrode was tested as a function of RH in the absence of any contaminant gaseous species. The test chamber was adjusted to approximately 0%RH (no air flow through the saturator line) and 25°C. The Au-Au electrode was heated to approximately 40°C prior to insertion into the atmospheric test chamber. The slightly elevated temperature was intended to minimize the propensity for condensation on the sample surface prior to equilibration with the test environment. EIS experiments were run at a given RH level until the response was stable. EIS was run on a Gamry Femtostat using a 15 mV AC signal and a 0 V vs. RE DC offset. Once the EIS data stabilized at a particular RH, the RH was increased to the next target level and the procedure repeated.

The EIS data are shown in Figure 22. The overall trend is a decrease in the impedance as the RH is increased. A plateau in the Bode magnitude plot at intermediate to high frequency can be used as an estimate of the solution resistance value. Unfortunately, as the impedance of the system increases, quantifying R_s becomes increasingly difficult due to overlap with the impedance of the electrode itself, cables and

instrument impedance. To make the analysis more self-consistent the data can be fit to an analogous electrical model and specific parameters from the model taken as the measurement of interest (in this case R_s).

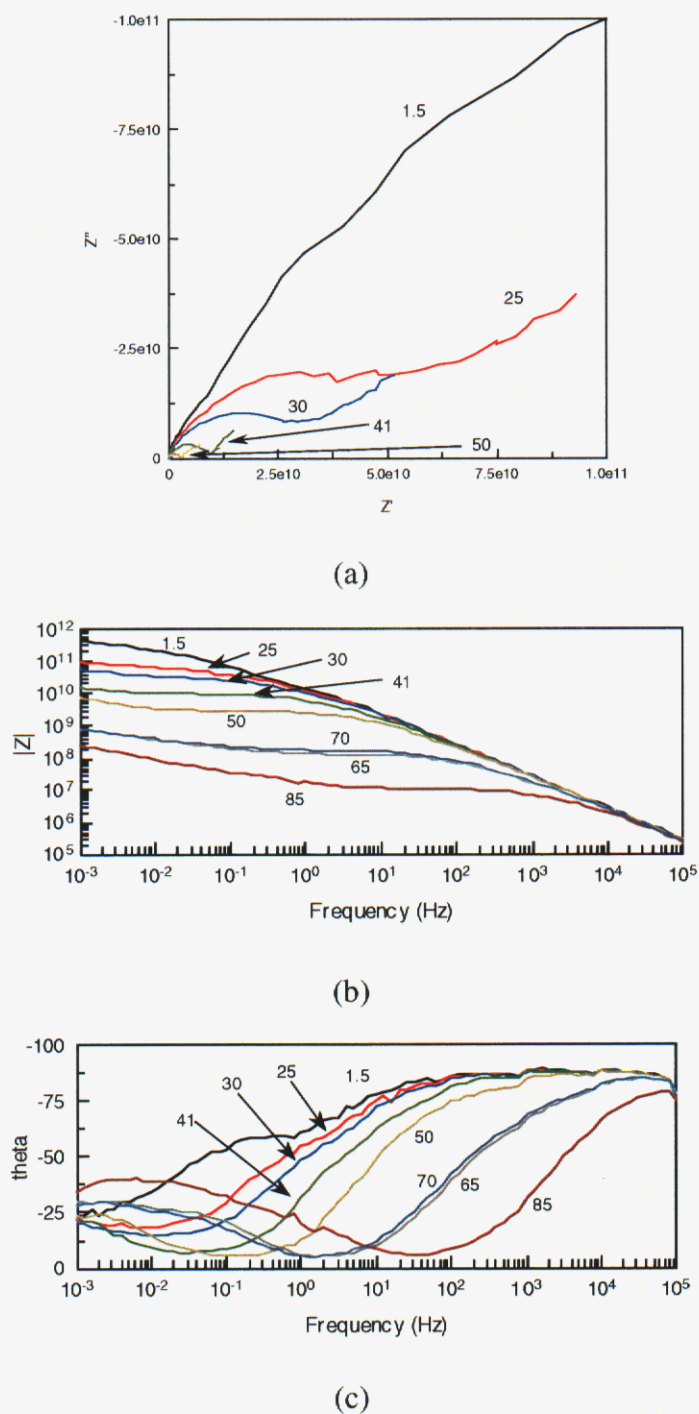


Figure 22 EIS data for Au-Au electrode as a function of RH. (a) Nyquist plot (data for 65, 70 and 85% RH are not visible on this plot), (b) Bode magnitude plot, (c) Bode phase angle plot. For each plot the numbers indicated refer to the RH at the time of the measurement.

The circuit model developed to fit the EIS data from the Au-Au electrode is shown in Figure 23. CPE1 is a parasitic capacitance arising from the sample design and the electrometer cables. CPE2 is an interfacial impedance due to the double layer at the electrode-electrolyte interface. W1 is a Warburg-type impedance used to describe the diffusion limited processes that occur at low frequencies. R2 is an interfacial impedance that dominates the Faradaic processes at higher frequencies. Finally, R1 is taken to be the solution resistance (R_s) and is a quantitative indication of the electrolyte impedance. A visual example of the quality of the fit is shown in Figure 24.

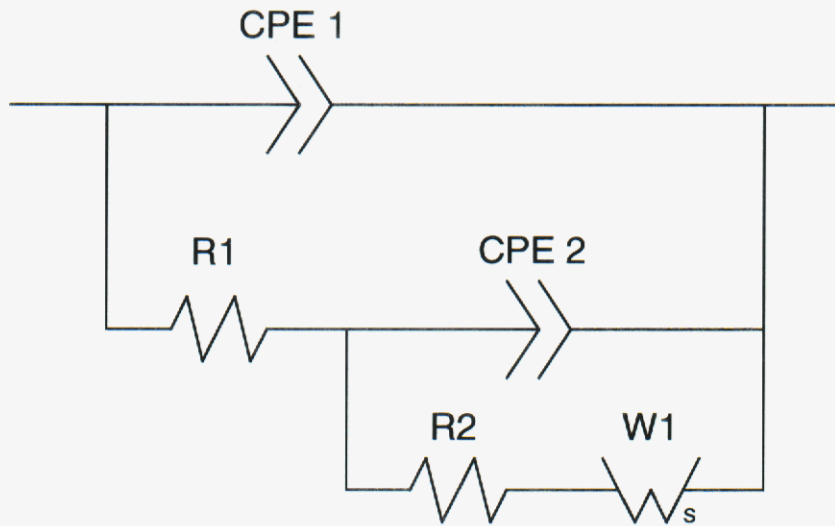
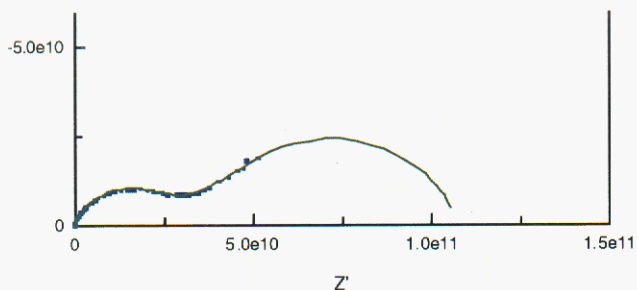
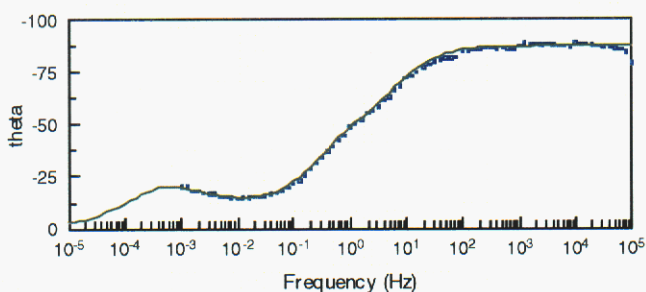
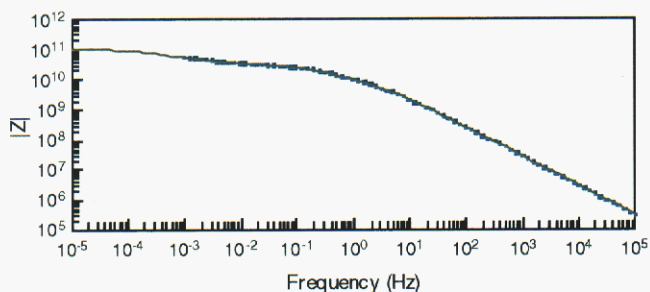


Figure 23 Circuit model used for fitting the EIS data from the Au-Au electrode.



(a)



(b)

Figure 24 Example of EIS data fitted to circuit model analogue. The individual markers are the raw data and the solid line is the fit.

By fitting the circuit model from Figure 24 to each data set shown in Figure 22, it was possible to determine estimates of R_s as a function of RH. When R_s is plotted against RH (Figure 25) a classic S-curve shape is observed. The rapid decrease in R_s that occurs between about 30% and 40% RH can be interpreted as indicative of a critical RH where the adsorbed electrolyte becomes sufficiently thick to support ionic conduction and electrochemical reactions. Comizzoli reports an exponential dependence of surface current on RH for nonconductors having the form¹⁴:

Equation 1
$$I = I_0 \exp(b * RH) \exp(-E/kT)$$

Where I_0 and b are constants, E is activation energy, k is Boltzmann's constant, and T is temperature. The constant b is the slope of the plot of $\ln I$ vs. RH and has experimentally determined values ranging from 0.1 to 0.3¹⁴. Because resistance and current have a

reciprocal relationship, $1/R_s$ can be plotted vs. RH and a value extracted for b . Excluding the datapoint collected at 1.5%RH, the $1/R_s$ data are shown in Figure 26 along with a fit to Equation 1. The slope from this fit was determined to be 0.11, in good agreement with the literature values.

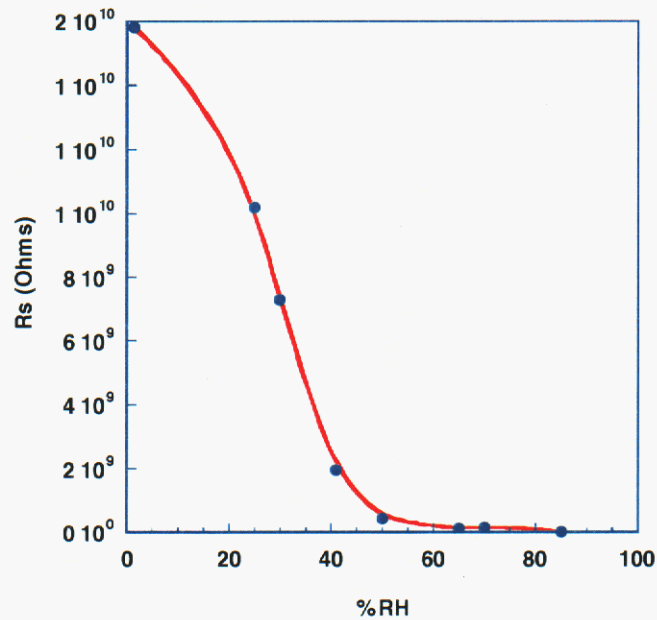


Figure 25 R_s vs RH determined using the Au-Au electrode. R_s Values were determined by fitting the data from Figure 22 with the circuit model from Figure 23.

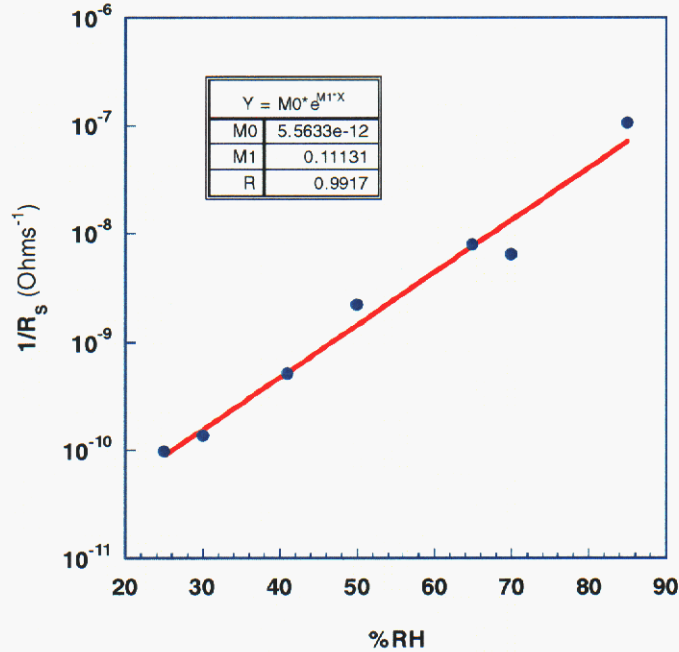


Figure 26 $\ln(1/R_s)$ plotted against RH. The slope was determined to be 0.11.

The R_s vs. RH data can also be used to calculate estimates of the solution layer thickness as a function of RH. For two parallel, coplanar electrodes, the resistivity of the adsorbed electrolyte is related (approximately) to the dimensions of the electrochemical cell and measured resistance as follows:

$$\text{Equation 2} \quad \rho = \frac{R_s \cdot l \cdot h}{d} \quad \text{or,} \quad h = \frac{\rho \cdot d}{R_s \cdot l}$$

where, ρ is resistivity ($\text{Ohm}\cdot\text{cm}^2$), R_s is solution resistance (Ohms), l is the length of the electrodes (cm), h is the solution height (cm) and d is the electrode separation (cm). For the Au-Au electrode, $l = 22700 \mu\text{m}$, $d = 20 \mu\text{m}$, and R_s is measured with EIS. Only h and ρ are unknown. The conductivity of deionized H_2O that has equilibrated with the ambient atmosphere is approximately $2.2 \text{ M}\Omega\cdot\text{cm}$; this value was used as an upper bound on the estimate of the resistivity of the adsorbed electrolyte during exposures to moist air. Because surface cleanliness is unknown, an additional prediction of solution height was made using $1\text{e}5 \Omega\cdot\text{cm}$ as the resistivity, to simulate the presence of contaminants. The resulting predictions as a function of RH are shown in Figure 27. For $\rho=2.2\text{e}6 \Omega\cdot\text{cm}$, the solution thickness varies from 1.3 nm at 1.5%RH to 2200 nm at 85%RH. For $\rho=1\text{e}5 \Omega\cdot\text{cm}$, the solution thickness varies from 0.06 nm at 1.5%RH to 102 nm at 85%RH. These values are reasonable for adsorbed solution layer thickness. Clearly, future work should include a complimentary technique for directly measuring solution

thickness in parallel with R_s measurements; then it would be possible to more accurately calculate solution conductivity as a function of RH.

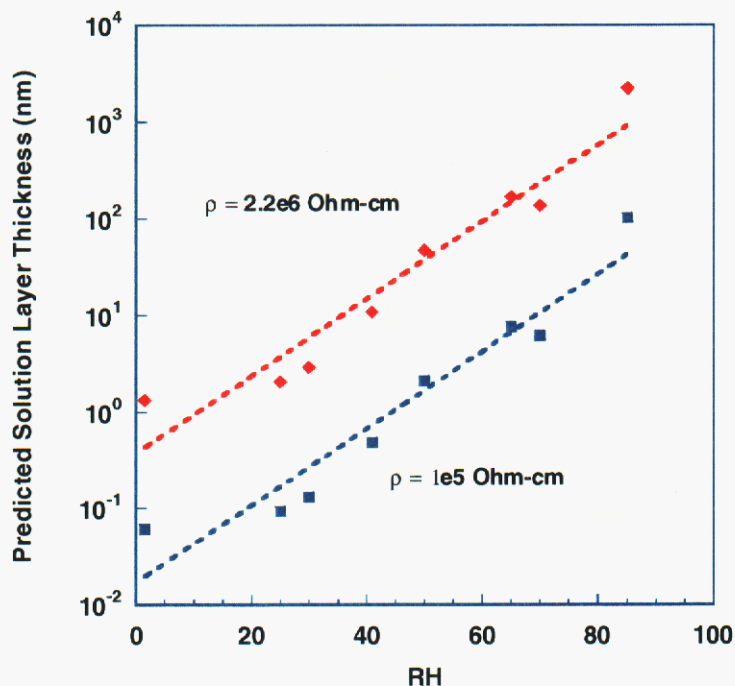


Figure 27 Predicted solution layer thickness as a function of RH. R_s values from EIS experiments run on the Au-Au electrode were used to estimate the solution layer thickness.

3.4.4 Al foil-Al foil electrode

An electrode constructed from parallel Al foils was tested under various combinations of RH and $[\text{Cl}_2]$ to (1) determine the functionality of this type of electrode and (2) study the atmospheric behavior of Al. The parallel foil construction allows the sample to be used multiple times by simply re-polishing the electrode surface between experiments. The drawback to this electrode design is that the parallel foils have a large capacitance that can interfere with high impedance measurements. As a comparison, the Bode magnitude impedance data is shown for a nominally dry Al foil electrode, the Au-Au EIS electrode at 1.5%RH, and the response of the test equipment (Femtostat) when no sample is connected (Figure 28). It is clear that the Au electrode has significantly higher impedance and is better suited to making measurements in low conductivity environments. However, the foil electrodes should be sensitive to changes in impedance at low frequencies. The foil electrodes should also be applicable to testing in relatively high RH environments.

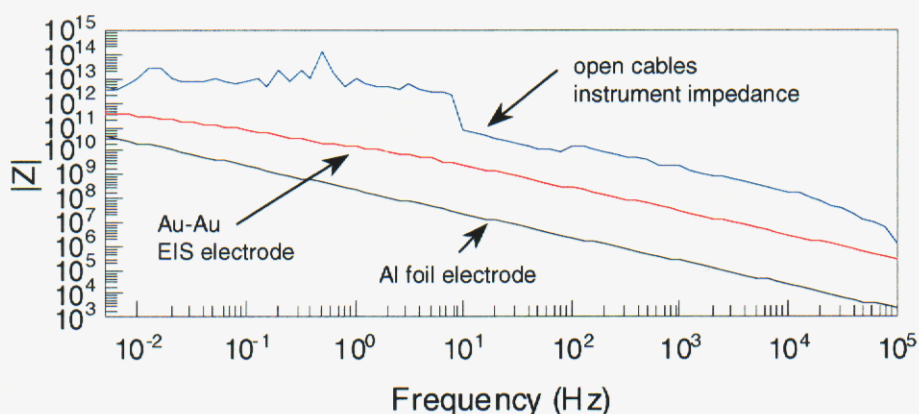


Figure 28 Comparison between the impedance of the Femtostat potentiostat, the Au-Au EIS electrode and the Al-Al foil electrode.

The impedance behavior of the Al-Al foil electrode was measured in 20 ppb Cl_2 at RH levels of 35, 40, 50 and 60% in order to determine the sensitivity of this electrode/measurement combination, and to determine if a critical RH could be identified for Al. An example of the raw EIS data from these experiments is shown in Figure 29. The 60%RH data can be easily differentiated from the data collected at lower RH, however, there does not seem to be resolvable differences between the 35, 40 and 50% RH data. The expected trend is for the magnitude of the impedance to decrease with increasing RH. In these experiments, the most sensitive datum to RH should be the lowest frequency probed (4 mHz). Multiple EIS experiments were conducted at each RH and the resulting real component of the impedance (Z') and the magnitude of the impedance ($|Z|$) were plotted as a function of experiment number (Figure 30). Although $|Z|$ should decrease with increasing RH, Z' should increase with increasing RH for high impedance systems. After a period of stabilization at 35%RH, the expected trends in Z' and $|Z|$ are observed. These data demonstrate the need to look at a population of measurements (for this type of electrode) in order to resolve differences at low RH.

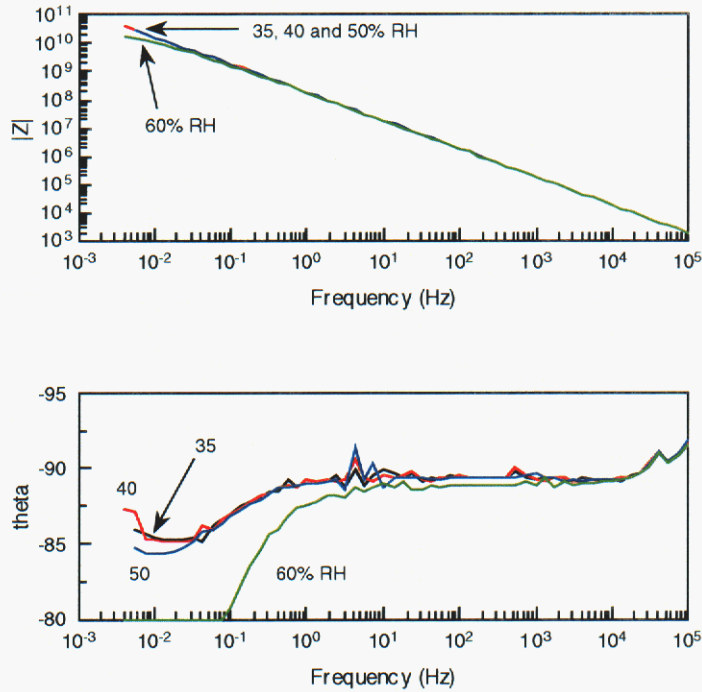


Figure 29 Bode magnitude and Bode phase angle plots of the Al-Al foil electrode impedance as a function of RH in the presence of 20 ppb Cl_2 . A reduction in impedance from 50%RH to 60%RH can be resolved, however, the impedance results at 35%, 40% and 50% RH are not clearly distinguishable.

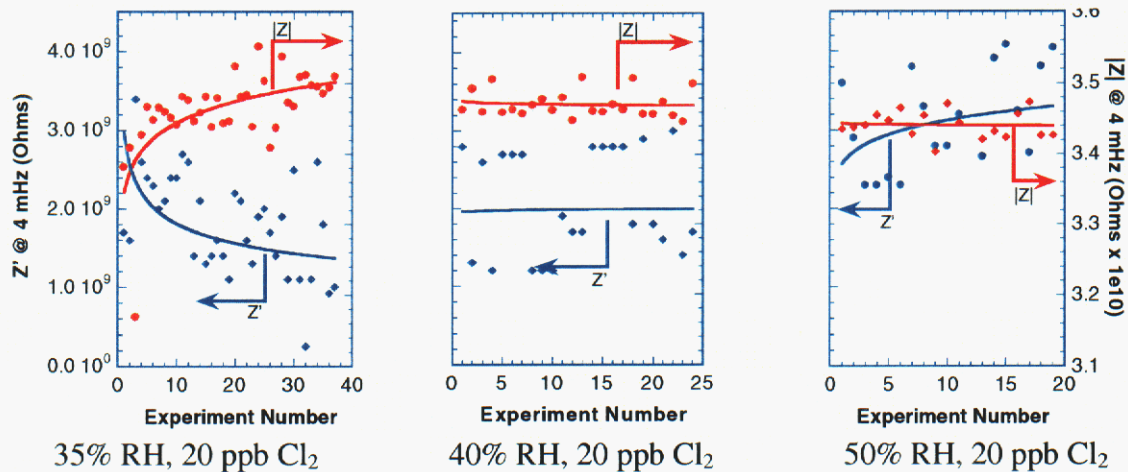


Figure 30 Low frequency impedance data for Al-Al foil electrode exposed to 20 ppb Cl_2 at 35, 40 and 50% RH. For these experiments, Z' at 4 mHz increases with decreasing impedance and $|Z|$ decreases with decreasing impedance. The overall trend is that the impedance decreases with increasing RH.

The $|Z|$ data for all four RH values are shown in Figure 31. Once again, on this scale, it is very difficult to differentiate electrode behavior at low RH. The important observation from these data is the profound change in electrode behavior when the RH is

increased from 50% to 60%. The $|Z|$ value changes dramatically as a function of time at 60%RH. This behavior is indicative that a critical RH value has been reached and electrochemical reactions can take place. To test the ability to measure corrosion in this environment/ electrode system a galvanodynamic experiment was performed. In this experiment a ramped current was applied between the two Al electrodes at a rate of $1e-13$ A/s and the resulting potential difference between electrodes was measured (Figure 32). As the current increases, the potential field also increases. When the potential field reaches a critical value, the aluminum oxide breaks down and localized current ensues. Breakdown of the oxide exposes metallic aluminum to the electrochemical system and causes a negative shift in the measured potential. The localized corrosion propagates until the applied current is insufficient to maintain active dissolution, at which time the system repassivates and the measured potential decays back to the previous level. As the current is increased, the potential signal will continue to oscillate indicating passive and corroding behavior. It is anticipated that at a high enough current the corrosion will stabilize (this has been observed in aqueous systems).

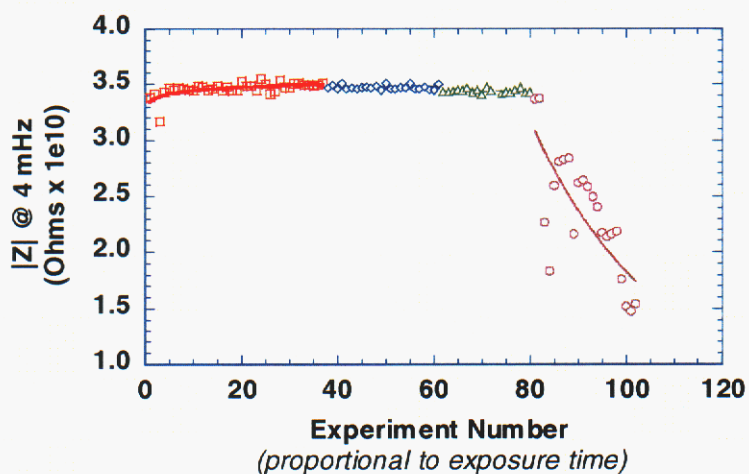


Figure 31 Low frequency impedance data for Al-Al foil electrode exposed to 20 ppb Cl_2 at 35, 40, 50 and 60% RH. Only subtle changes occur in the impedance data until RH > 50%. These data suggest a critical RH for Al in this environment between 50% and 60% RH.

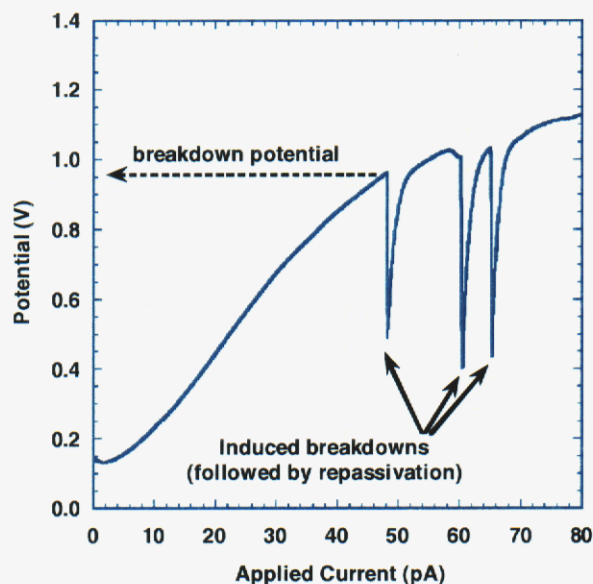


Figure 32 Galvanodynamic data from Al-Al foil electrode at 60%RH and 20 ppb Cl_2 . Negative spikes in the potential signal correspond to oxide rupture.

In a separate experiment an Al-Al foil electrode was exposed to 85% RH and 20 ppb Cl_2 in order to evaluate the behavior of the electrode under more conductive atmospheric conditions. A series of open circuit tests, galvanic current experiments and EIS tests were run as a function of time in this environment. The galvanic current experiments indicated that pitting might be taking place on the electrodes, but the data contained artifacts that made it difficult to make conclusive interpretations. The open circuit data also indicated localized corrosion events were taking place but once again contained artifacts. The EIS data, on the other hand, were more consistent and made it possible to track the average behavior of the electrode as a function of time. The Nyquist, Bode magnitude and Bode phase plots (Figure 33) all indicate a significant decrease in the impedance as the sample equilibrates with the environment. The details of the Bode phase plot are more easily resolved as time progresses and it becomes easier to separate solution resistance and polarization resistance. In order to quantify these parameters, the data were fit to the circuit model shown in Figure 34 and the extracted values are plotted in Figure 35. Interestingly, it is not possible to extract separate R_s and R_p values at short exposure times. This is attributed to the lack of adsorption of moisture to the surface. With increasing time, the R_s value becomes distinct from R_p , differing by a factor of 100. These data demonstrate the applicability of the Al-Al foil electrode to measuring electrochemical reactions under high humidity conditions.

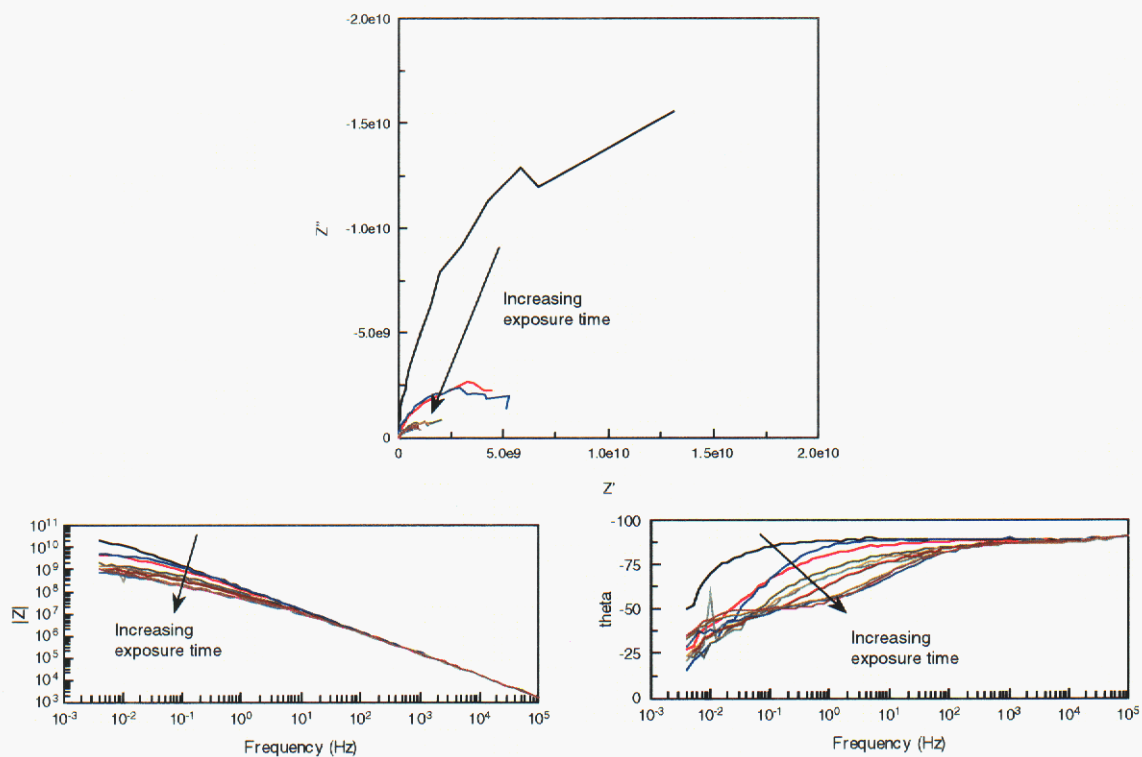


Figure 33 Impedance data in the Nyquist and Bode formats for an Al-Al foil electrode at 85% RH and 20 ppb Cl_2 . As the exposure time increases and the adsorbed electrolyte layer forms, the impedance decreases and features in the data are more easily resolved.

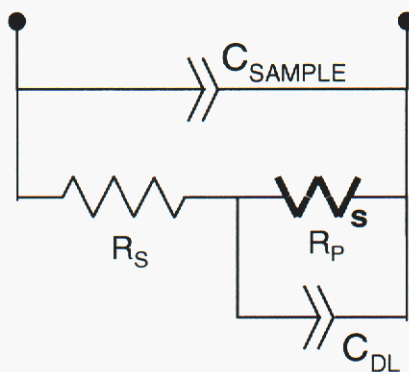


Figure 34 Circuit model used for fitting data from the Al-Al foil electrode.

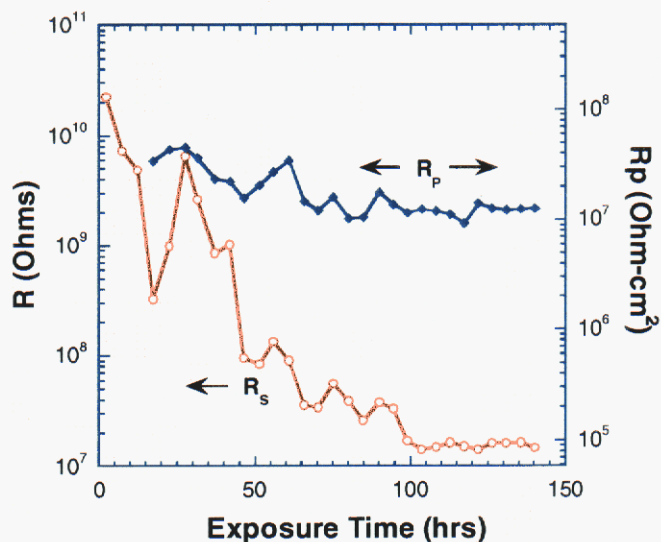


Figure 35 R_p and R_s for an Al-Al foil electrode in 85%RH and 20 ppb Cl_2 . Values were extracted from a fit of the model shown in Figure 34 to the raw EIS data.

After the exposure at 85%RH and 20 ppb Cl_2 , the sample was examined using scanning electron microscopy (Figure 36). It is evident from the presence of corrosion products that localized attack took place, validating to some extent the trends observed in the open circuit and galvanic current measurements.

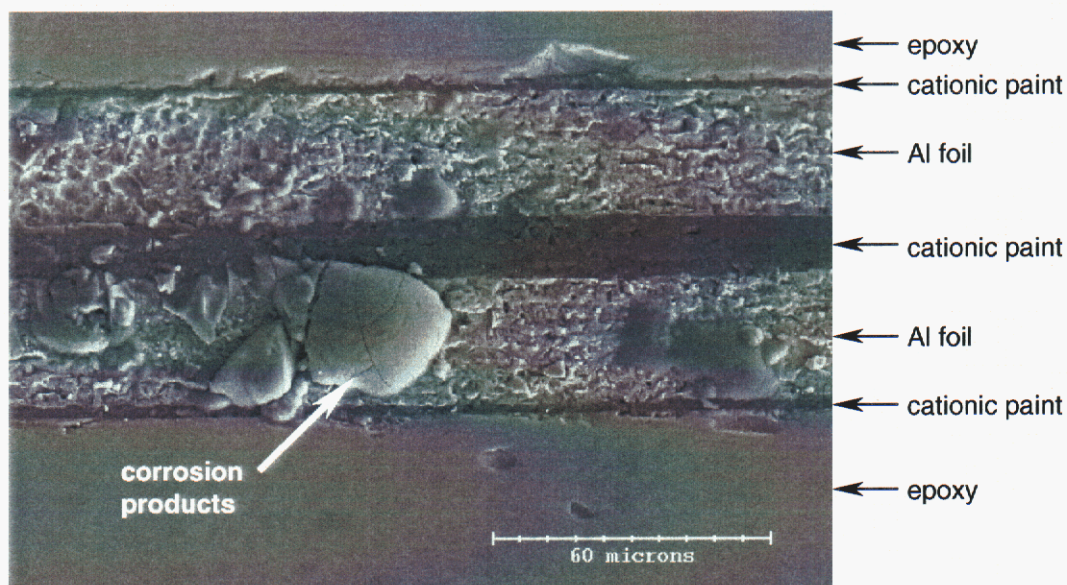


Figure 36 SEM micrograph of Al-Al foil electrode following exposure to 85%RH and 20 ppb Cl_2 .

Overall, the Al-Al foil electrode is suitable to measuring the corrosion behavior of Al over a range of RH. Below a critical RH, differences in EIS data are difficult to resolve, but the data still yield a quantifiable measure of conductivity between electrodes. The critical RH can be measured with this electrode by tracking $|Z|$ as a function of RH. Above the critical RH, it appears that standard two-electrode electrochemical experiments can be carried out. The galvanodynamic data suggest that pitting susceptibility can be quantified as a function of atmospheric environment. Finally, at sufficiently high RH it is possible to quantify both R_s and R_p , allowing for interfacial processes to be distinguished from solution resistivity. It is anticipated that fabricating parallel, coplanar Al metallizations will result in a much lower electrode capacitance, and thus allow even better quantification of the electrochemical behavior across a wider range of RH.

3.4.5 Cu-Cu foil electrodes

Electrodes were constructed from parallel foils of Cu and tested at high RH to determine the sensitivity of EIS to a system undergoing uniform attack. Whereas the Al-Al electrodes exhibited generally passive on the electrode surface, the Cu-Cu electrodes should corrode at a fairly consistent rate. Samples were initially tested in 20 ppb Cl_2 , and either 80% or 85% RH. All samples had approximately 10 mm of exposed electrodes, thus comparisons of the data without area correction should be valid. EIS data from three separate experiments are shown in Figures 37-39. Sample #1 (Figure 37) exhibited two stages of behavior; early in the exposure the impedance of the system was very high and good data could not be collected. Later in the experiment, the impedance dropped significantly and it was possible to resolve R_p and R_s values after that point. The cause of the change in behavior is not well understood and has not been observed in any other experiments. It is possible that a surface contaminant acted to impede water adsorption and resulted in an induction time for corrosion attack. Interestingly, once the impedance of the system dropped, the magnitudes of the impedance data were similar to the other experiments, although the shapes of the low frequency data were slightly different. Samples #2 (Figure 38) and #3 (Figure 39) showed consistent behavior throughout the experiment with gradual decreases in both low and mid-frequency impedance.

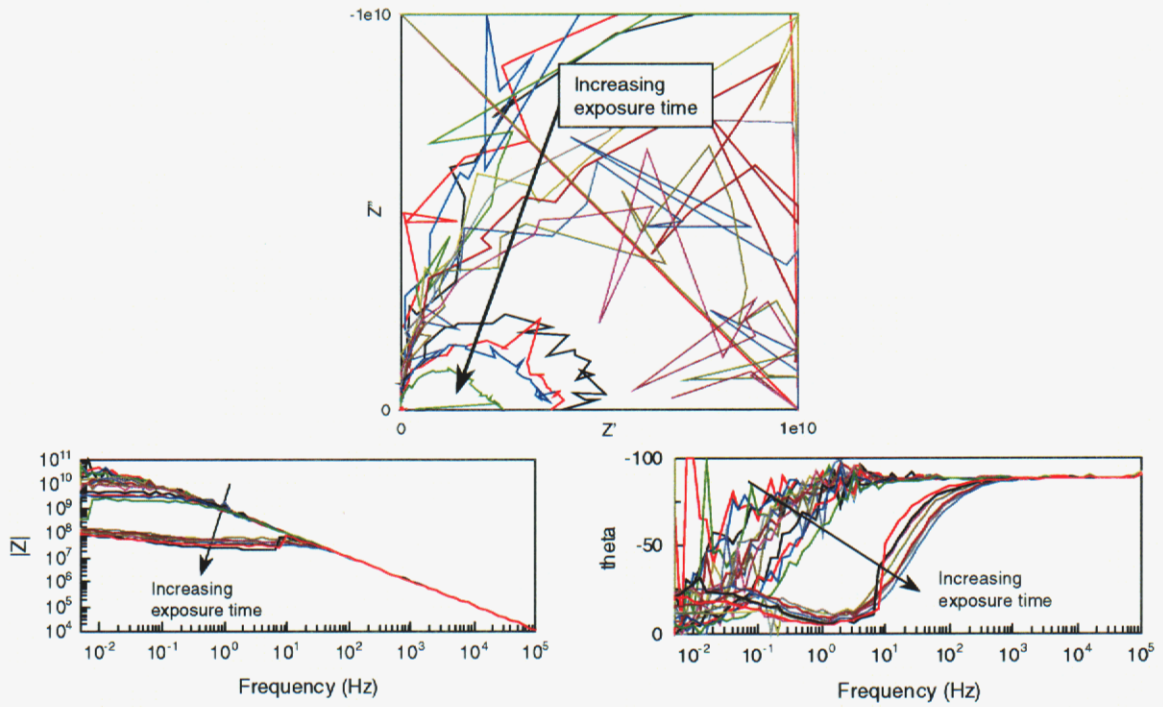


Figure 37 Impedance data in the Nyquist and Bode formats for Cu-Cu foil electrode #1 at 85% RH and 20 ppb Cl_2 . At early times in the exposure, high impedance coupled with the lack of proper shielding results in poor data quality.

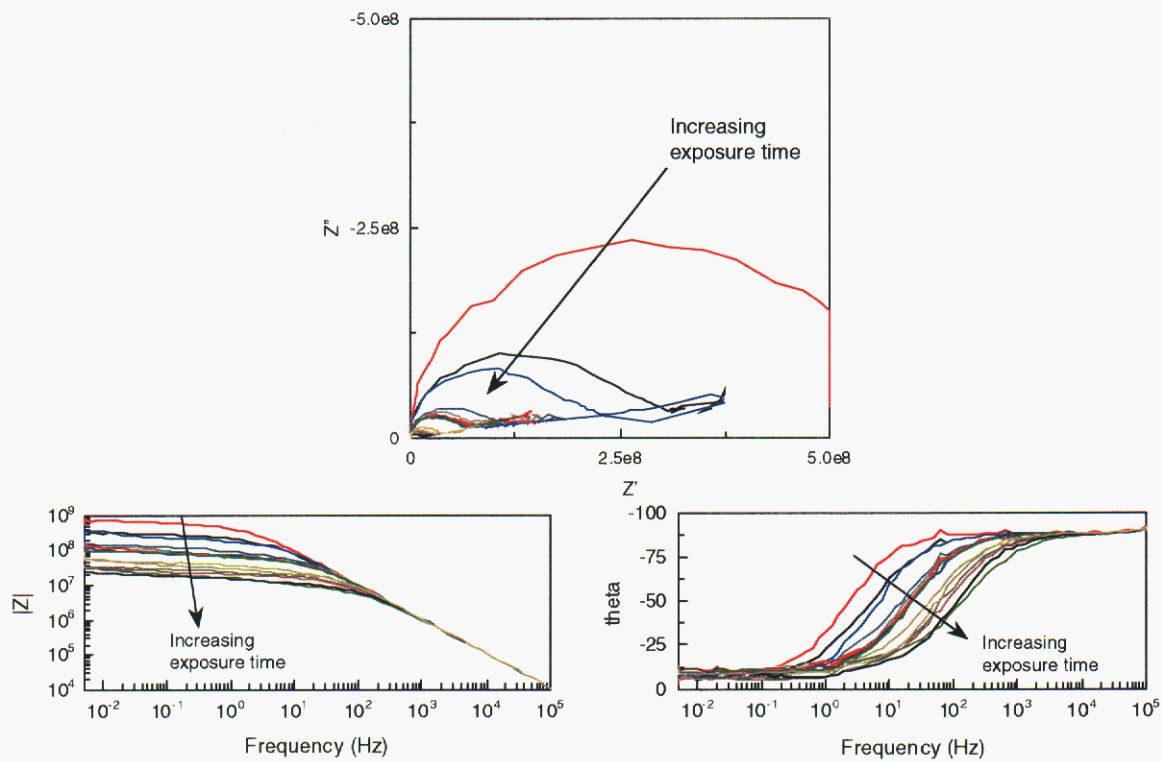


Figure 38 Impedance data in the Nyquist and Bode formats for Cu-Cu foil electrode #2 at 85% RH and 20 ppb Cl₂.

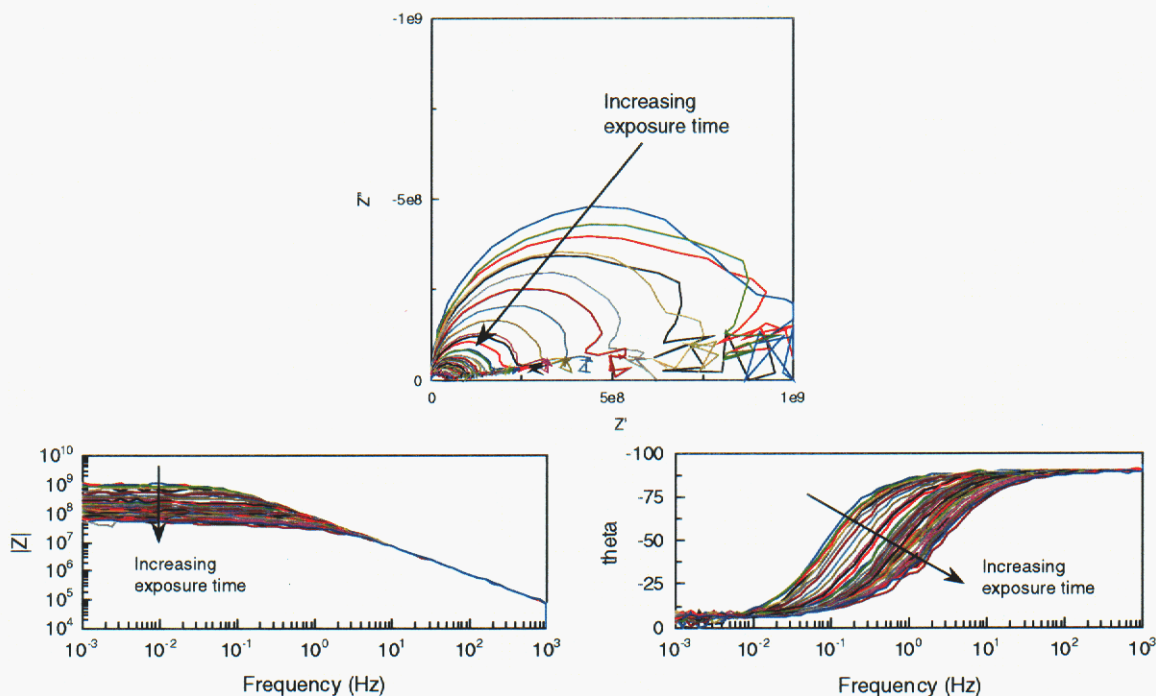


Figure 39 Impedance data in the Nyquist and Bode formats for Cu-Cu foil electrode #3 at 80% RH and 20 ppb Cl_2 .

The circuit model used for fitting the data from the Cu-Cu electrodes was the same as that used for the Al-Al electrodes (Figure 34). The data from sample #2 were fit using this model and the resulting values for R_s and R_p were plotted as a function of exposure time (Figure 40). The R_p values decrease with time, but the rate of decrease appears to slow as the experiment progresses. This may be due to corrosion product layers building up and impeding the process. Of course, corrosion product build-up can also alter the hygroscopic behavior of the surface and lead to increased water layer adsorption.

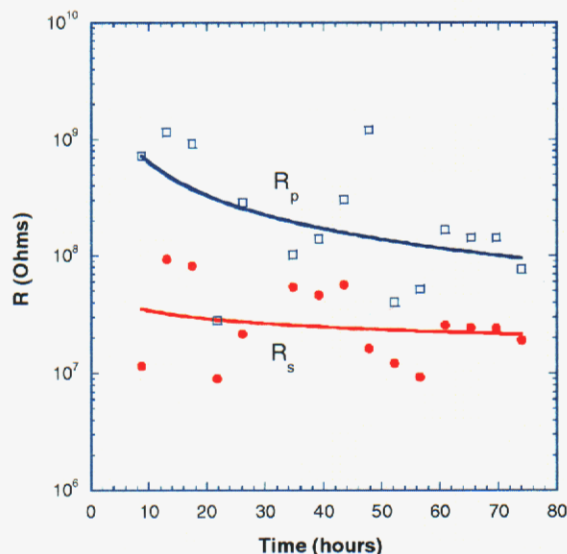


Figure 40 R_p and R_s values for Cu-Cu electrode #2 exposed to 85%RH and 20 ppb Cl_2 . The values were extracted from the data in Figure 38 by fitting to the circuit model shown in Figure 34.

In order to facilitate analysis of large data sets, a simple indicator for the magnitude of R_p was developed. The low frequency ($f = 5$ mHz) value of $|Z|$ provides an adequate indicator of R_p as determined by complex equivalent circuit fitting of the data (Figure 41). The magnitudes of the values determined by the two methods usually agree within about a factor of 2X, and the trends of R_p vs. time are practically identical. Using this analysis approach, R_p values were plotted as a function of time for the data from samples #2 and #3 (Figure 42). Although there is considerably more scatter in the data from sample #2, the trends and magnitudes of the data are in exceptional agreement. This reproducibility suggests that the EIS test is applicable to corrosion monitoring, especially when the electrode is undergoing uniform corrosion. The mode of attack on the copper electrodes was verified as uniform attack using SEM (Figure 43). Attempts were made to quantify the extent of corrosion by Focused Ion Beam cross sectioning of the corroded area. However, it was not possible to establish a reference height for how much material had been removed. Future endeavors to link EIS data to material loss should be performed with thin film samples such that the starting material thickness will be accurately known.

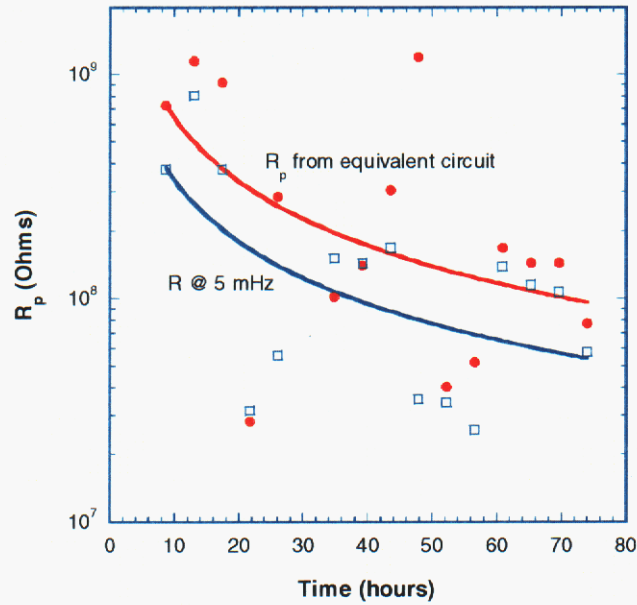


Figure 41 Comparison of R_p determined by fitting data to an equivalent circuit model and R determined by taking the 5 mHz datum for $|Z|$. The data are from Cu-Cu sample #2 (Figure 38).

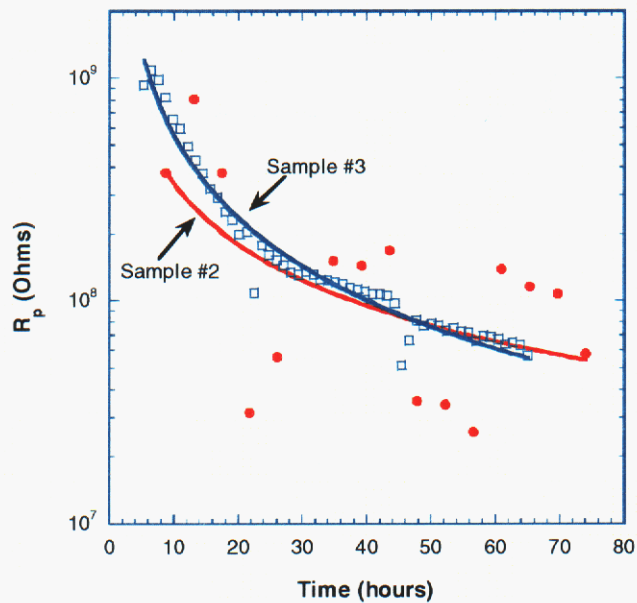


Figure 42 Comparison of R_p for Cu-Cu samples #2 and #3. R_p values were approximated as the $f=5$ mHz datum from the $|Z|$ data.

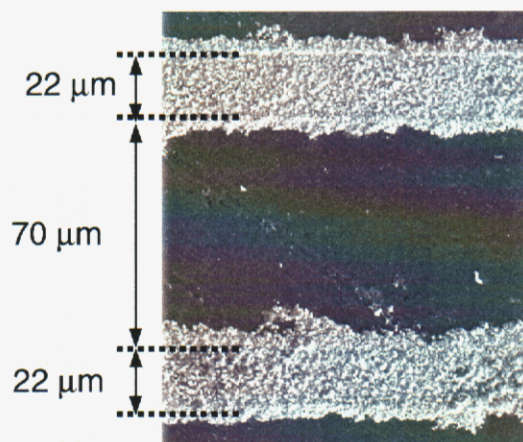


Figure 43 SEM micrograph of parallel Cu electrodes after exposure to 85%RH and 20 ppb Cl_2 at 25°C for approximately 150 hours.

A Cu-Cu foil electrode (sample #4) was exposed to an 80%RH, 155 ppb H_2S environment for comparison with electrodes exposed to the Cl_2 environment. The EIS data were very consistent throughout the experiment and indicated gradual decreases in both the high and low frequency impedance (Figure 44). For evaluation purposes, the R_p values were approximated by value of $|Z|$ at 2 mHz. R_s values were evaluated by fitting a semicircle to the high frequency data in the Nyquist plot and taking the intercept with the real axis as the solution resistance value. The high frequency semi-circle in these data reflects the time constant formed by the R_s and the sample capacitance. Plotting R_p and R_s vs time (Figure 45) shows that both values decrease throughout the experiment. The R_p data appears to be reaching a plateau value at around 10 hours but then begin decreasing with a different slope. It is hypothesized that this decrease is due to the spread of conductive corrosion products between the electrodes. Further evidence for corrosion product spreading is observed in the last datum for the R_p data, which is considerably lower than for earlier times. After that datum was collected, it was determined that the sample had shorted out.

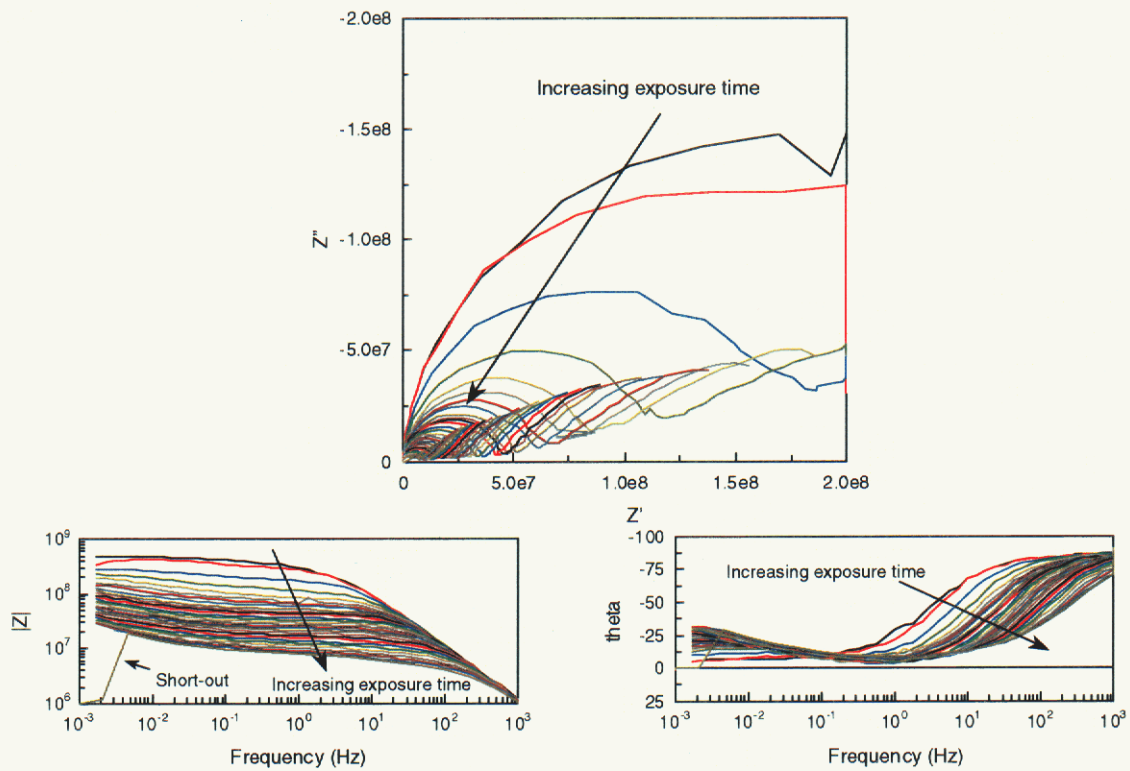


Figure 44 Impedance data in the Nyquist and Bode formats for Cu-Cu foil electrode #4 at 80% RH and 155 ppb H₂S.

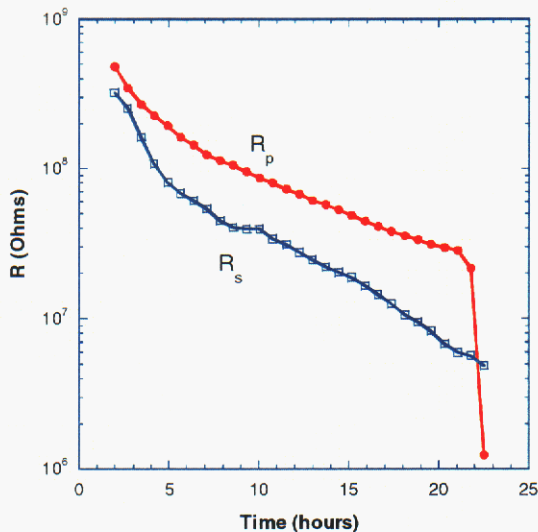


Figure 45 R_p and R_s values for Cu-Cu electrode #4 exposed to 80%RH and 155 ppb H_2S . The values were extracted from the data in Figure 44. The R_p values were approximated by the value of $|Z|$ at 2 mHz. The R_s values are from a simple circle fit to the Nyquist data in the high frequency regime. The sharp drop in R_p at the end of the experiment corresponded to the electrodes shorting out due to growth of corrosion products.

A clear difference can be seen between the response of the Cu-Cu electrodes in the Cl_2 and H_2S environments by inspecting the trends of R_p and R_s vs time (Figure 46). For Cu in the Cl_2 environment R_s appears to reach somewhat of a steady state early in the experiment whereas for Cu in the H_2S environment R_s decreases throughout the entire exposure. R_p decreases more rapidly in the H_2S environment and attains lower average values than observed in the Cl_2 environment. These trends indicate that the corrosion products formed in the presence of Cl_2 are more protective than those formed in the presence of H_2S .

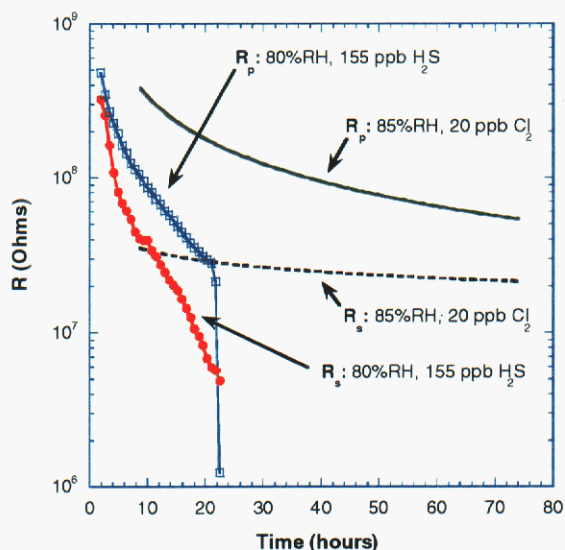


Figure 46 Comparison of R_p and R_s for Cu-Cu electrodes in 85%RH, 20 ppb Cl_2 (sample #3) and 80%RH, 155 ppb H_2S (sample #4).

The Cu-Cu foil electrodes demonstrate the applicability of using EIS to monitor corrosion rate as a function of time and environment. Even though the EIS data were not correlated with material loss, the changes in R_p and R_s are reasonable and demonstrate the ability to quantify the relative corrosion rate during an exposure. Furthermore, the technique appears to be reproducible (Figure 42) and is capable of differentiating the rates of attack that occur in environments of varying severity (Figure 46).

3.4.6 Cu-plated Al electrodes

Electrodes were constructed from parallel foils of Cu-plated Al in order to study the response of a system undergoing exacerbated localized attack. The Cu plating was intended to drive corrosion of the Al foils; both enhanced uniform dissolution and localized attack. If each electrode corrodes at an elevated rate, the electrochemical data should indicate an active system. Test samples were exposed to an aqueous environment as well as atmospheric in order to gather data on the baseline response of this electrode type. Furthermore, comparisons could be made between inundated, aqueous corrosion behavior and atmospheric corrosion behavior.

The aqueous exposure was performed by exposing an electrode to 100 ml of deionized H_2O with continuous bubbling of 20 ppb Cl_2 gas through the solution. A large area Pt-mesh counter electrode was included in the test cell for making measurements of the electrodes against an inert and stable electrode. Since the Pt mesh is much larger than the Cu-plated Al foil electrodes, the Pt should not contribute significantly to any impedance measurement; that is, Z_{measured} should be approximately equal to $Z_{\text{Cu/Al electrode}}$.

Figure 47 shows the EIS data for measurements made between two identical and adjacent Cu-plated Al foil electrodes, and between a Cu-plated Al foil electrode and a

bulk Pt counter electrode in solution. The data are shown for time different exposure times and indicate that the system does not change significantly over the course of the exposure. All formats for representing the EIS data show a high noise level at low frequencies. This is attributed to pitting attack occurring on the Al electrodes, and causing an unstable E-I relationship. The instability at low frequency makes quantification of a polarization resistance difficult by normal fitting procedures. Therefore R_p was approximated by the following relationship¹⁵:

Equation 3

$$R_p = \frac{4}{\pi} \int_{\ln \omega_m}^{\infty} Z''(\omega) d \ln \omega$$

Where, ω_m is the frequency corresponding to the maximum in the Z'' data. This method for calculating R_p is shown to agree with a circle fit to the Nyquist data for atmospheric data later in this report (Figure 59). After approximately 15 hours of exposure, the R_p values calculated using this technique are 4.4 M Ω for the foil-foil experiment and 1.7 M Ω for the foil-Pt mesh experiment. This is approximately a factor of 2 difference, which agrees with the predicted behavior.

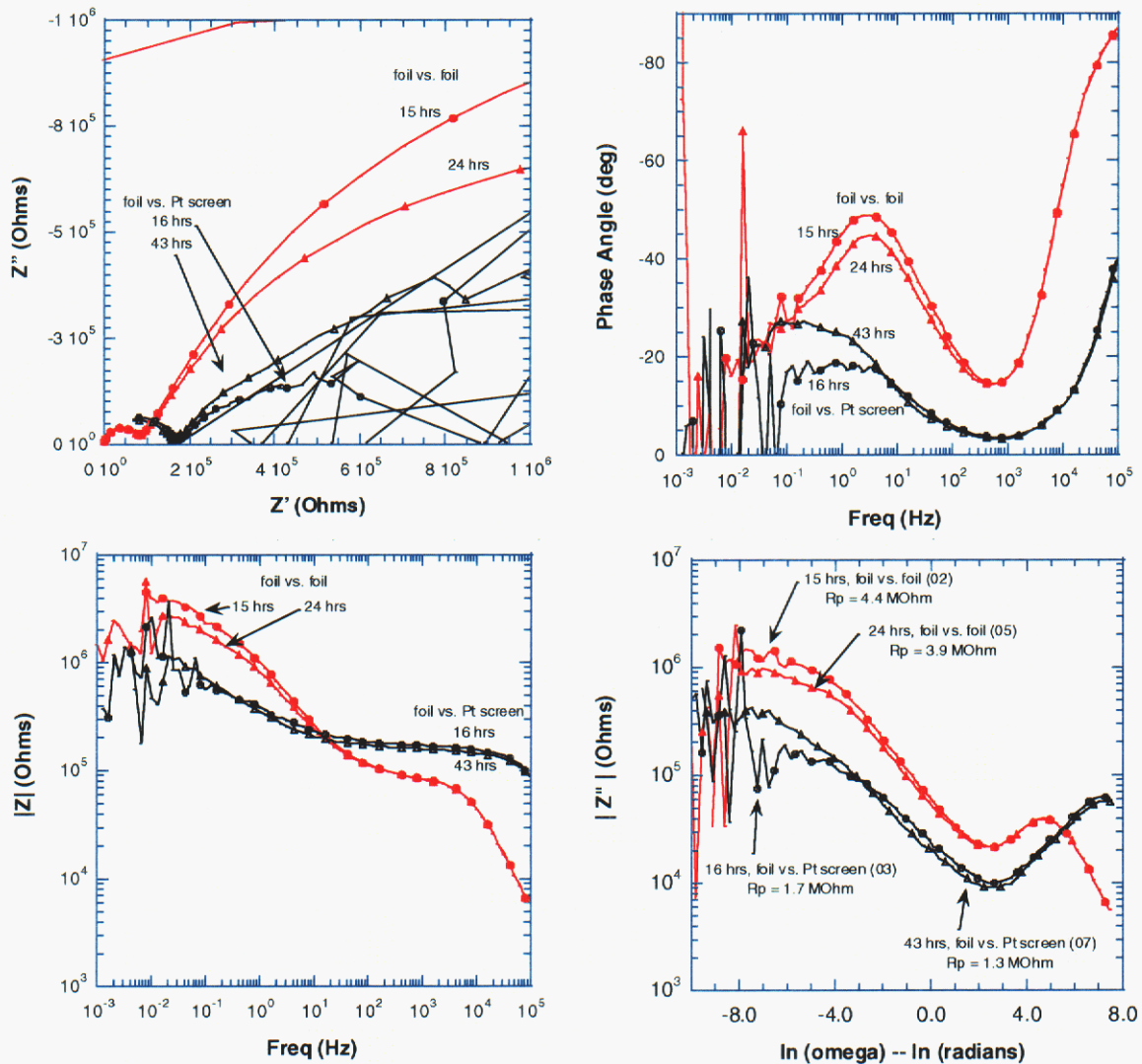


Figure 47 EIS data for Cu-coated Al foils in deionized H₂O sparged with Cl₂ gas. Impedance determined from testing two identical electrodes is approximately twice that from a one-electrode test.

Open circuit potential noise measurements were also used to evaluate the corrosion behavior under aqueous conditions. When two identical Cu-coated Al foil electrodes are used to make the measurement (Figure 48), the mean value for the signal is approximately 0 and significant positive and negative fluctuations indicate activity on both electrodes. Later in the exposure (approximately 45 hours), the potential of each Cu-coated Al foil was measured against the Pt electrode (Figure 49). In each case negative going potential fluctuations indicate localized attack. The oscillating behavior is likely due to initiation and repassivation of local corrosion sites.

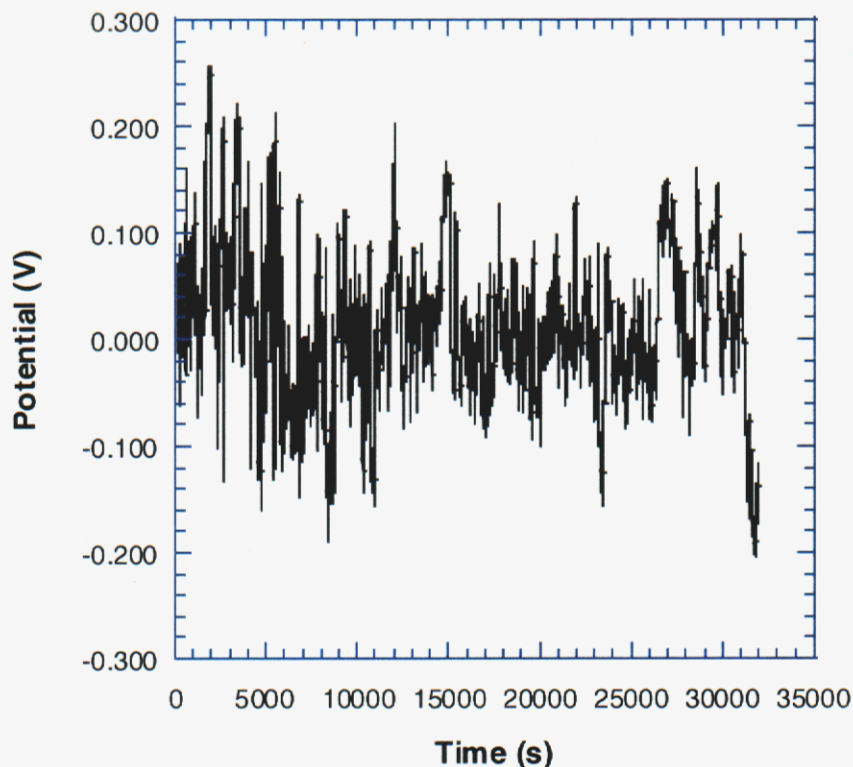


Figure 48 Potential measured between two identical Cu-coated Al foil electrodes exposed to deionized H₂O sparged with 20 ppb Cl₂ gas. Symmetric, large-magnitude fluctuations are indicative of localized corrosion occurring on both electrodes. Data are from the beginning of the exposure.

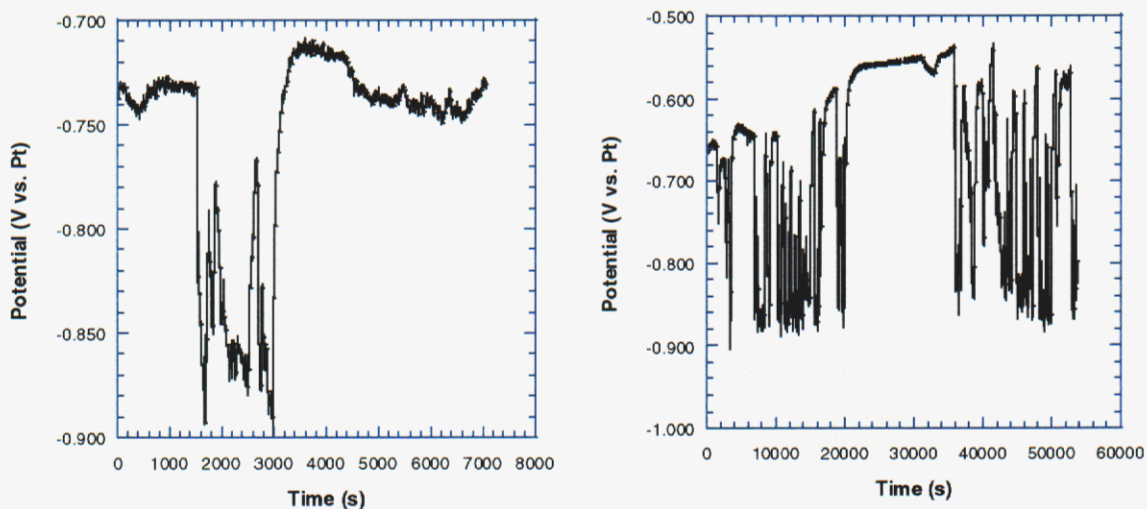


Figure 49 Potential measured between Pt mesh electrode and Cu-coated Al foil electrodes in deionized H₂O sparged with Cl₂ gas. Left graph is from electrode number one after 45 hours. Right graph is from electrode number two after 47 hours.

An attempt was made to evaluate the corrosion resistance behavior of these electrodes using galvanodynamic polarization (Figure 50). In order to calculate an accurate R_p value, a clear linear region of the E vs. I plot is required. In this data set the potential is not consistently dependent on the current and an R_p value could not be calculated. This is essentially due to the random fluctuations in current and voltage between the electrodes being of larger magnitude than the imposed signal.

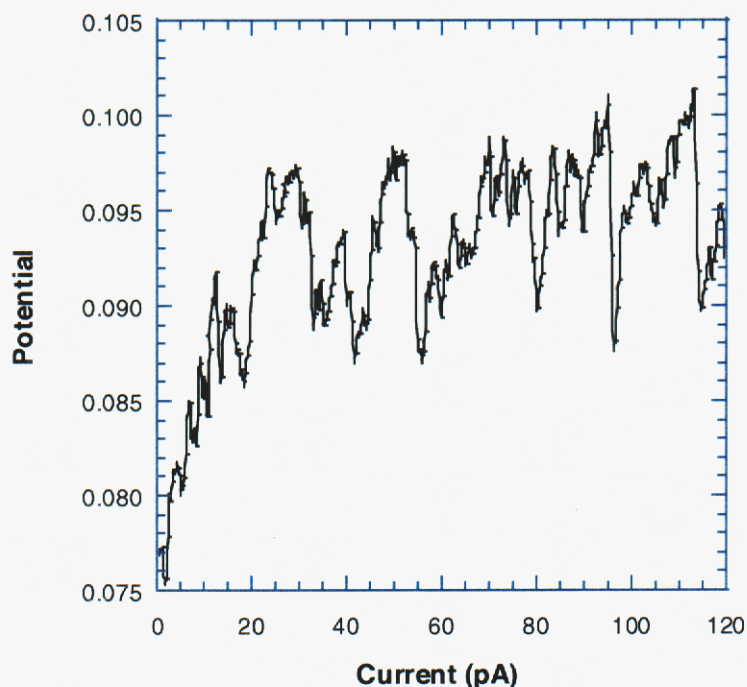


Figure 50 Example of galvanodynamic scan run on Cu-coated Al foil electrode in deionized H_2O sparged with 20 ppb Cl_2 . This experiment does not yield a reliable measurement of the electrode polarization resistance because of the localized corrosion occurring during the scan.

The Cu-plated Al foil electrode was inspected pre- and post-test using optical microscopy (Figure 51). A mostly continuous corrosion product is seen along all four of the Cu-Al interfaces. This could indicate that corrosion occurred preferentially at these locations. Alternatively, if there was a sharp pH gradient from the Al (anode, acidic to neutral pH) to the Cu (cathode, neutral to alkaline pH), then corrosion products from pits formed on the Al would become insoluble in this region and precipitate out of solution. No pits were observed optically, lending support to the first hypothesis, but more detailed microscopy is required to come to a definitive conclusion.

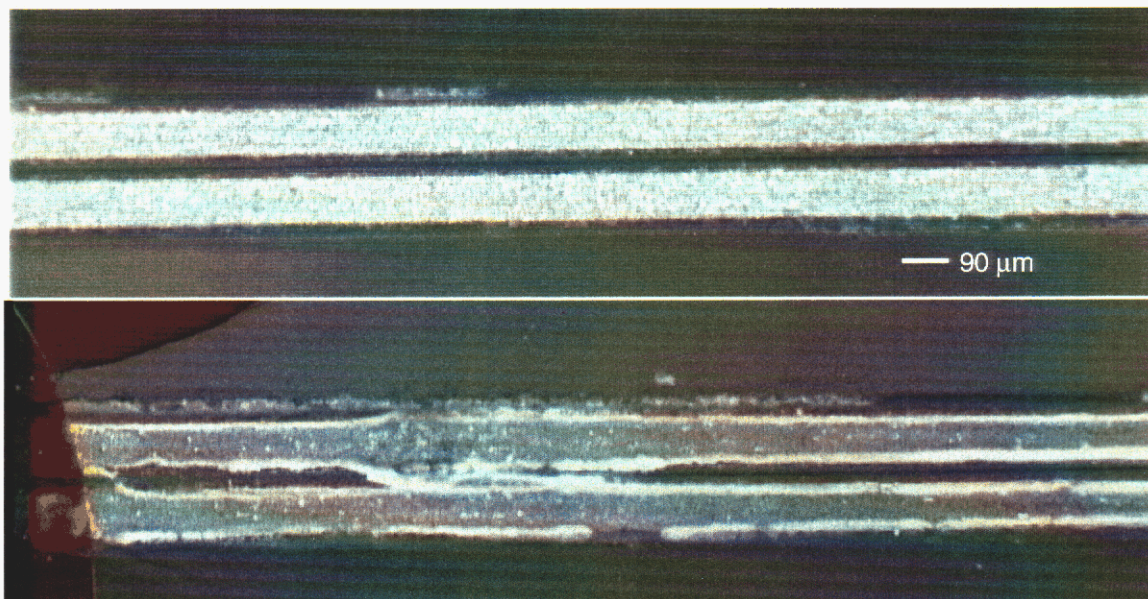


Figure 51 Cu-coated Al foils before (top image) and after (bottom image) exposure to deionized H₂O sparged with Cl₂ gas. Corrosion products are concentrated at the Cu-Al interface, indicating either localization of corrosion or possibly a preferential site for corrosion product precipitation.

The aqueous exposure solution was tested at the start and finish of the experiment for pH and conductivity. The pH decreased from 6.37 to 5.46 and the conductivity decreased from 4 MΩ to 0.048 MΩ after 67 hours of bubbling 20 ppb Cl₂ gas through 100 ml of solution.

Cu-plated Al foil electrodes were also exposed to 85%RH and 20 ppb Cl₂. An example of the raw EIS data is given in Figure 52. Similar to the aqueous exposure, the low frequency EIS data for the atmospheric exposure is erratic, indicating localized corrosion of the electrode. However, the magnitude of the noise in the atmospheric data is smaller, possibly due to a lower rate of corrosion attack. A circle fit was performed on the Nyquist data for three separate experiments and a plot of R_p vs. exposure time was constructed (Figure 53). There is significant variation in the data from the three exposures. Notably, sample #3 has an elevated R_p and sample #2 appears to have a low R_p , suggesting that it is the most active of the electrodes. Post test microscopy (Figures 54 and 55) qualitatively supports this interpretation. Sample #2 was inspected using focused ion beam (FIB) and SEM (Figure 56), and localized pitting and attack at the Cu-Al interfaces were identified as the modes of localized attack that occurred during atmospheric exposure. Comparison of the morphology of corrosion products on these samples to those observed under aqueous exposure (Figure 51), shows that corrosion products are distributed all across the Al foil under atmospheric conditions but are concentrated along the Cu-Al interface under aqueous conditions. In the atmospheric case the corrosion products will precipitate in close proximity to where they are formed because the local solubility is quickly exceeded when no bulk solution exists. Under aqueous conditions, however, the corrosion products may stay soluble and diffuse away

from the corrosion site. As mentioned previously, a pH gradient at the Cu-Al interface may be responsible for crash precipitation of the corrosion products. The other possibility is, of course, that the corrosion is concentrated at the boundary under aqueous conditions. The data collected in this program are insufficient to discriminate between these two hypotheses. Future research in this area will address the change in corrosion morphology that occurs as the solution layer thickness is reduced.

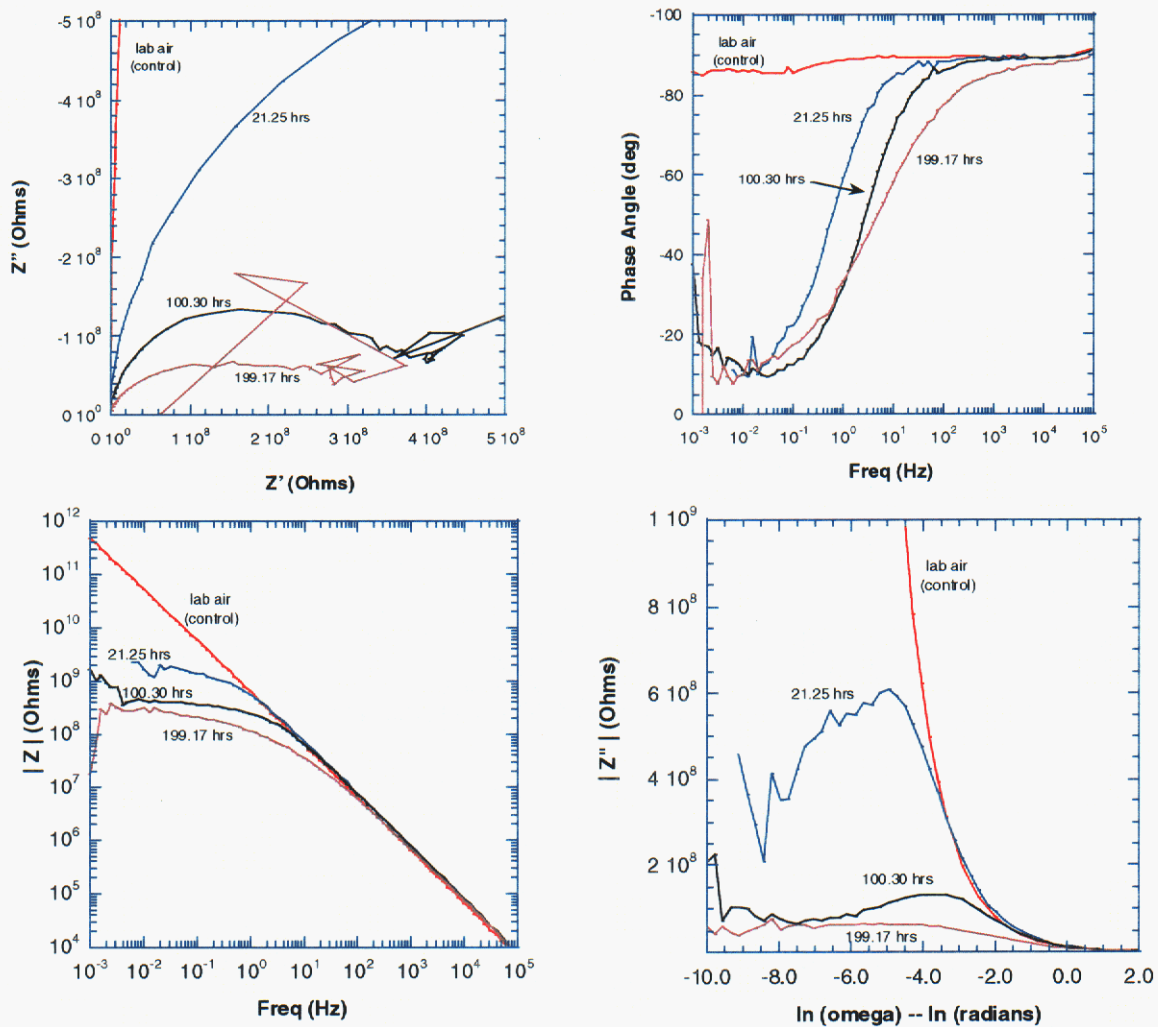


Figure 52 EIS data from parallel Cu-coated Al foil electrodes exposed to 85%RH and 20 ppb Cl_2 gas.

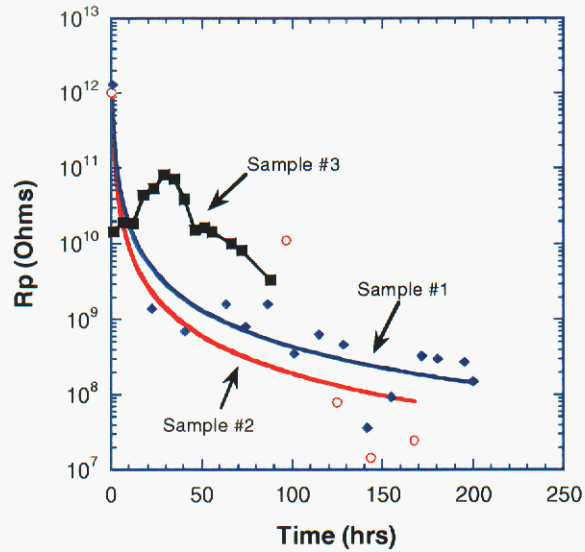


Figure 53 R_p data calculated from circle fit of Nyquist data for three Cu-plated Al foil samples exposed to 85%RH and 20 ppb Cl_2 . Sample #2 appears to have generally lower impedance than samples #1 and #3; optical inspection of the post-test surfaces suggests qualitatively that #2 underwent more severe corrosion.

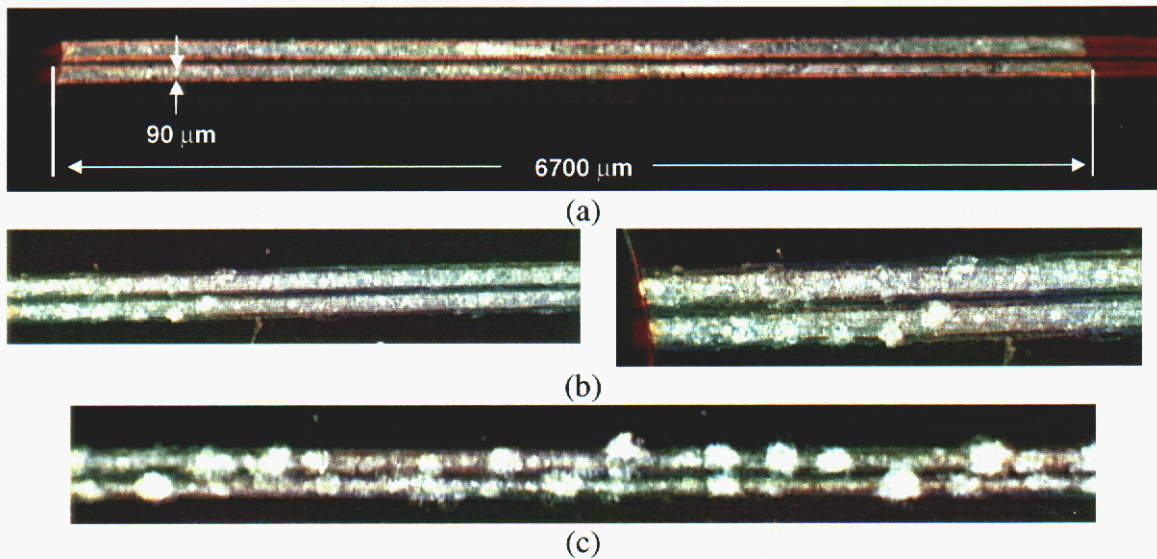


Figure 54 Pre- and post-test images of Cu-coated Al foil electrodes. (a) Pre-test, (b) sample #1 exposed for 216 hours, (c) sample #2 exposed for 219 hours.

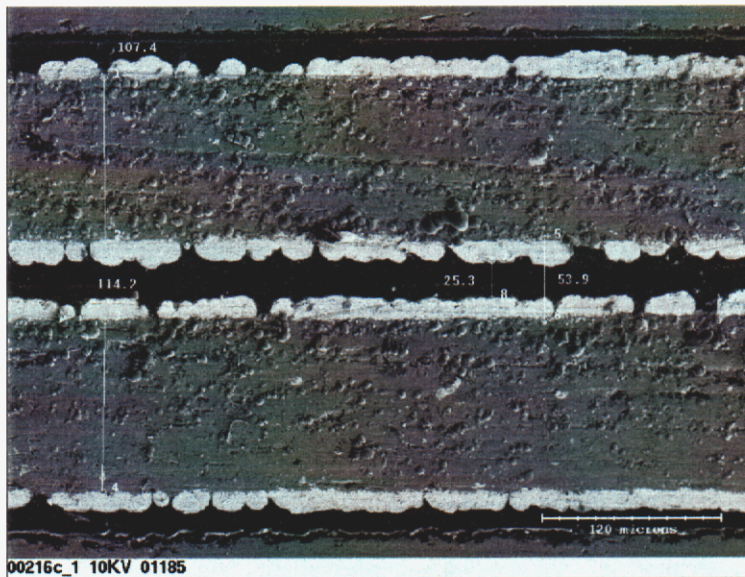


Figure 55 SEM of Cu-plated Al foil sample #3 after 88 hours exposure to 85%RH and 20 ppb Cl₂.

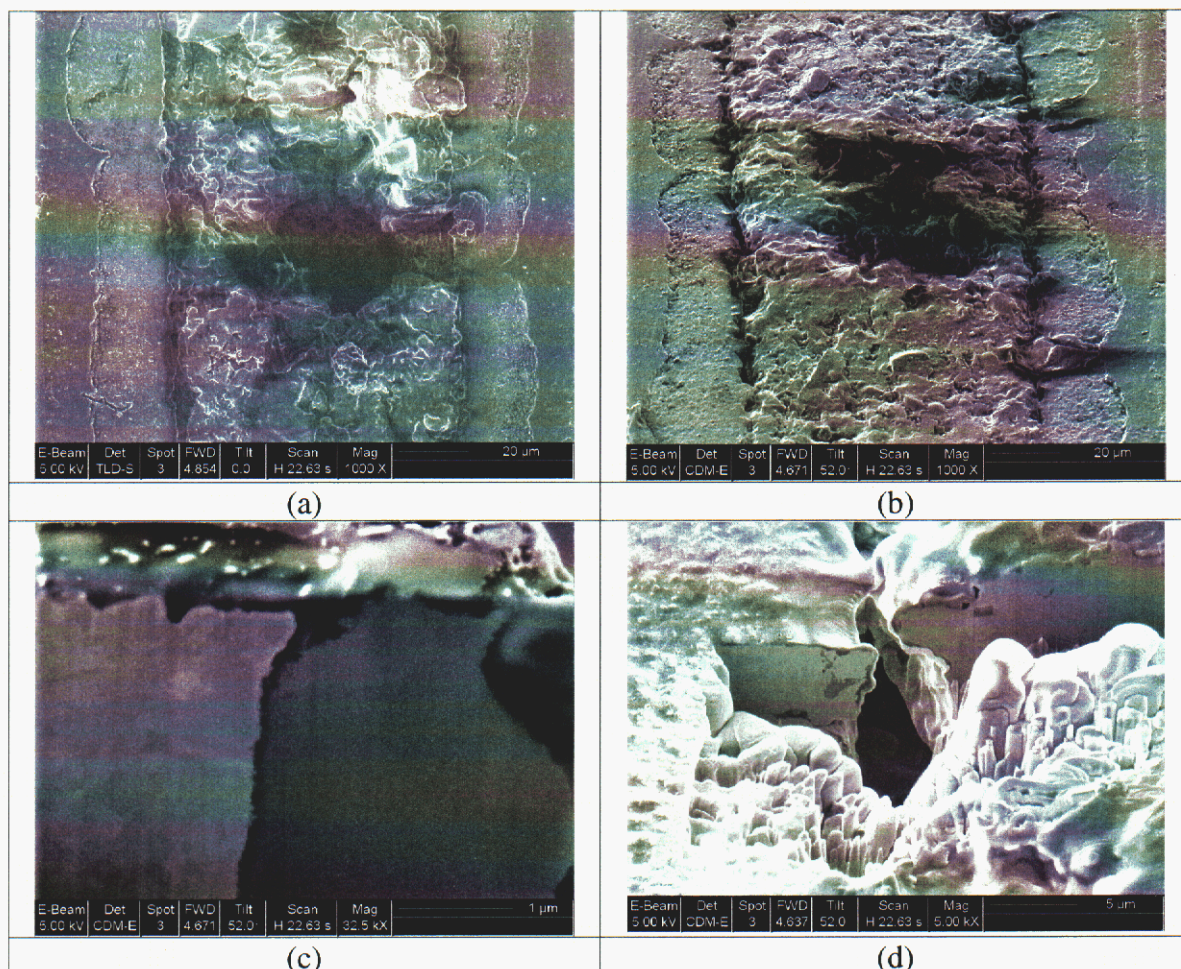


Figure 56 SEM and focused ion beam (FIB) of Cu-plated Al foil sample #2 exposed to 85%RH and 20 ppb Cl₂. Examples of pitting within the interior of the sample (a and b) and interfacial attack at the Cu-Al interface (c and d).

In addition to EIS testing, galvanodynamic (GVD) scans were used to evaluate the atmospheric corrosion behavior of Cu-plated Al foil electrodes. Figure 57 shows GVD and EIS data from sample #2. A linear E vs. I region was not apparent on the GVD plot; instead, the scan seemed to reflect periods of localized corrosion which appear as large drops in the measured potential. Although the potential fluctuations were on the order of 100's of mV, only very small currents were applied in this scan. The test was discontinued because of the large potential perturbations being induced (nominally, linear E-I regions are measured over a range of 10's of mV). Despite the difficulty with extracting R_p from the GVD data, a value was determined from a fit of the EIS data.

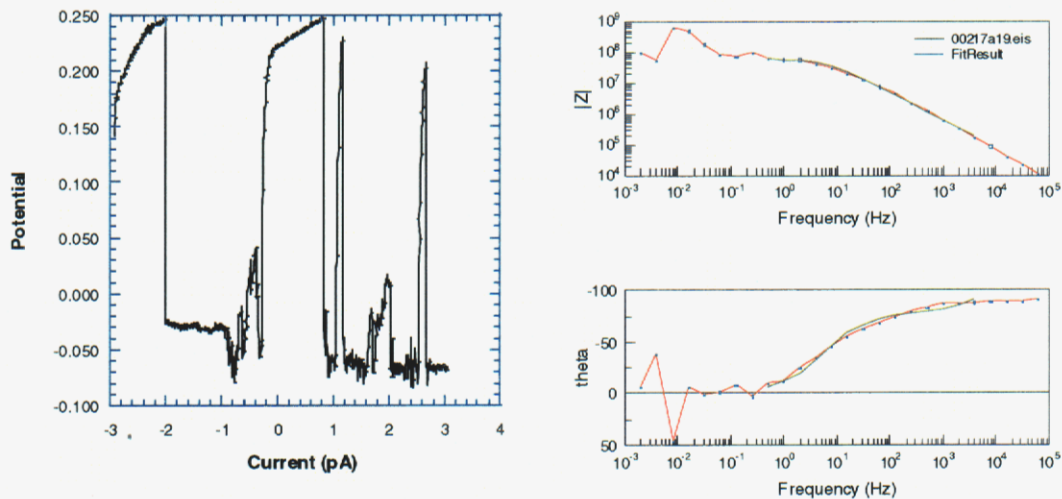


Figure 57 Galvanodynamic scan run on Cu-plated Al foil sample #2 (left) and EIS data (right). A R_p value could not be extracted from the galvanodynamic scan although a fit to the EIS data yielded a value of 60 M Ω .

During other portions of the same experiment it was possible to determine R_p from the GVD data (Figure 58). In this case the applied currents were much higher than in the previous experiment (nA vs. pA). Although the applied currents were higher, the large magnitude swings in potential were not observed. This is indicative of passive behavior of the Al-Cu couple. The GVD data yielded a value of 43 M Ω , which is in good agreement with the value of 39 M Ω obtained from the EIS data. The EIS data in Figure 58 is much cleaner at low frequencies than the EIS data in Figure 57; indications of passive and active behavior, respectively. Thus, the EIS data can always be manipulated to yield an average corrosion resistance (R_p) independent of the nature of the processes occurring on the electrode; whereas, the GVD data may not always yield an R_p value, but give indications as to the type of corrosion that is occurring.

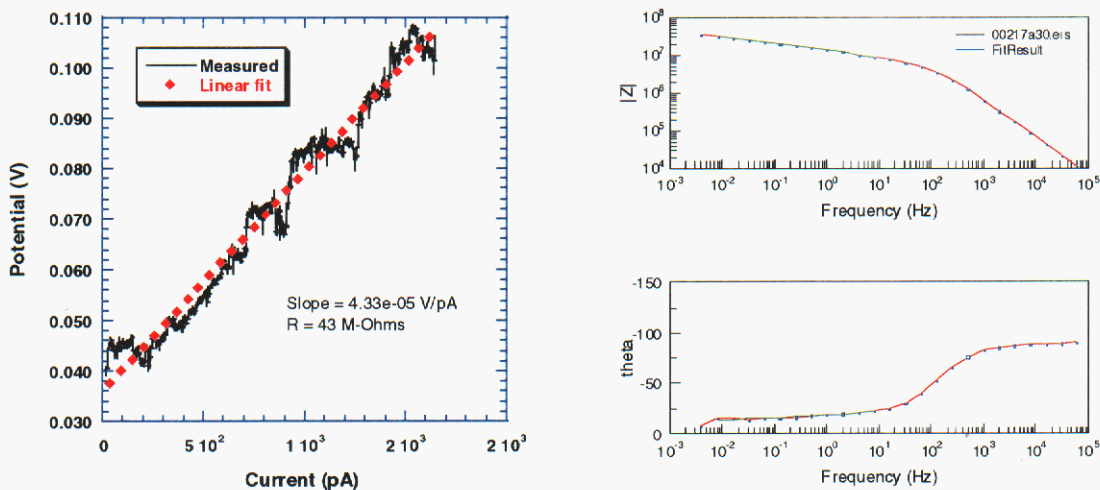


Figure 58 Galvanodynamic scan run on Cu-plated Al foil sample #2 (left) and EIS data (right). A R_p value of 43 M Ω was extracted from the galvanodynamic data and is in good agreement with the value of 39 M Ω from a fit to the EIS data.

Additional comparisons were made between GVD and EIS testing on sample #1 (Figure 59). A comparison is also included between the R_p values obtained by performing a simple circle fit to the Nyquist data and those obtained by integrating the Z'' vs. $\ln \omega$ data according to Equation 1. The GVD data agree quite well with the R_p values determined using the integration method. The R_p values from the integration method and from the circle fit are in reasonable agreement for all of the datapoints analyzed. Either method appears suitable for tracking changes in impedance as a function of exposure time. Neither method should be used as a precise measure of corrosion rate without correlating the values to independently measured material loss.

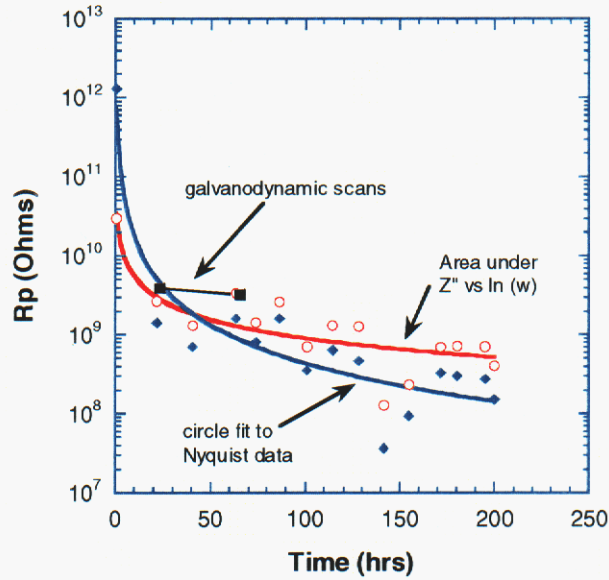


Figure 59 Comparison of R_p data for sample #1 determined by a circle fit to the EIS Nyquist, calculated using Equation 3 and from a linear fit to galvanodynamic data.

During the atmospheric exposure of sample #1, open circuit data between the two Cu-plated Al foil electrodes was periodically collected. The RMS potential (E_{RMS}) was calculated for each data set using a commercial software package.¹⁶ A correlation between R_p and E_{RMS} was observed (Figure 60), suggesting that open circuit monitoring might be a viable indicator for corrosion activity for this type of environmental probe. This technique was not pursued further in this program.

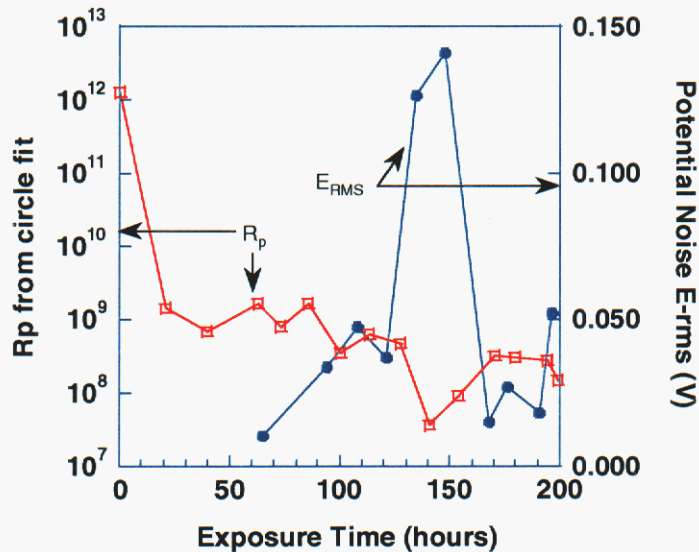


Figure 60 Comparison of R_p data from EIS data and potential noise data calculated from E_{OC} data. All data are from Cu-plated Al foil electrode #1 exposed to 85%RH and 20 ppb Cl_2 .

A comparison was made between the R_p data for the Cu-plated Al foil electrode, the Al foil electrode and the Cu foil electrode (Figure 61). It was anticipated that the Al foils would be mostly passive and have the highest impedance, the Cu foils would undergo uniform attack and have an intermediate impedance and the Cu-plated Al foils would undergo significant localized corrosion and thus have the lowest impedance. The data show the Cu electrodes had the lowest impedance, suggesting the rate of uniform attack was higher than was anticipated. The Al foils had fairly high impedance, which is consistent with a low corrosion rate. The Cu-plated Al foils had a range of responses including a very high impedance response. The troubling aspect of this result is that all of the Cu-plated Al electrodes showed signs of significant localized attack. It appeared that although the electrodes were corroding, there was a large signal loss between electrodes. It was hypothesized that the structure of the electrode might be contributing to the inconsistent impedance results. Perhaps a local chemistry on the Cu portions of the electrode were causing a change in surface tension and hence creating a high-impedance region. To test this hypothesis, two additional electrodes were constructed with the foils arranged as shown in Figure 62.

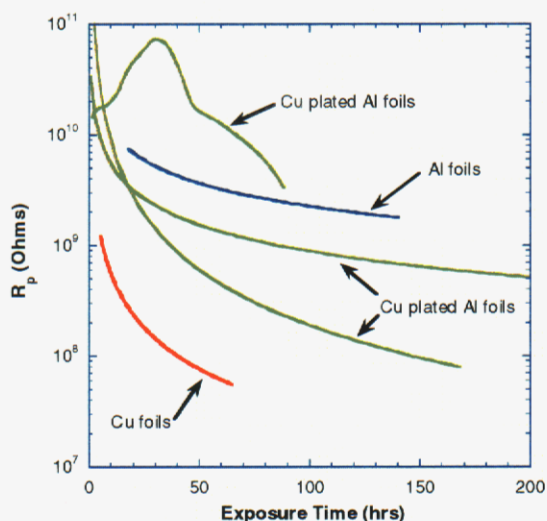


Figure 61 Comparison of various foil-based electrodes exposed to 85%RH and 20 ppb Cl_2 . The impedance of the Cu-plated Al foils is somewhat inconsistent. Theoretically, R_p for Al foils should always be larger than that for the plated electrodes.

The electrodes were exposed to 85%RH and 20 ppb Cl_2 and EIS data recorded as a function of exposure time. Surprisingly, the Al|Cu—Cu|Al electrode (Figure 63) behaved nominally the same as the Cu-plated Al electrodes, whereas the Cu|Al—Al|Cu electrode (Figure 64) had an extremely high impedance throughout the exposure. A comparison of the impedance magnitude data is given in Figure 65. Switching the order of the electrodes resulted in almost 4 orders of magnitude change in the impedance response! Post-test optical microscopy revealed similar types (pitting) and extent of damage on both electrodes. Thus it appears that the damage is the same although the behavior indicated by the EIS data is completely different. The most significant

conclusion to be drawn from this observation is that visual confirmation is mandatory for any damage assessment made from EIS data on a new electrode / environment system.

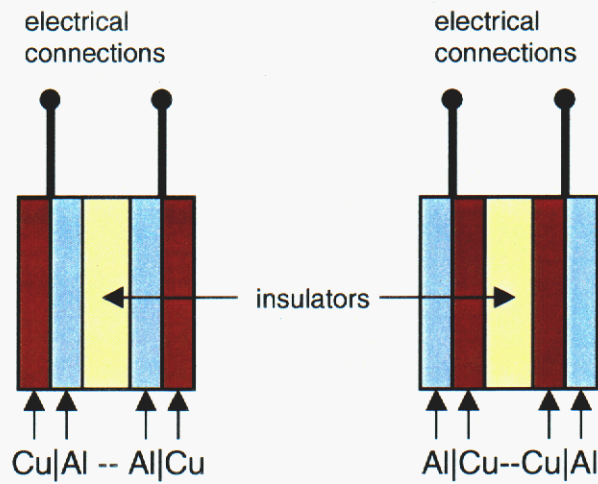


Figure 62 Schematic layout of electrodes for testing the effect of electrode order on impedance response.

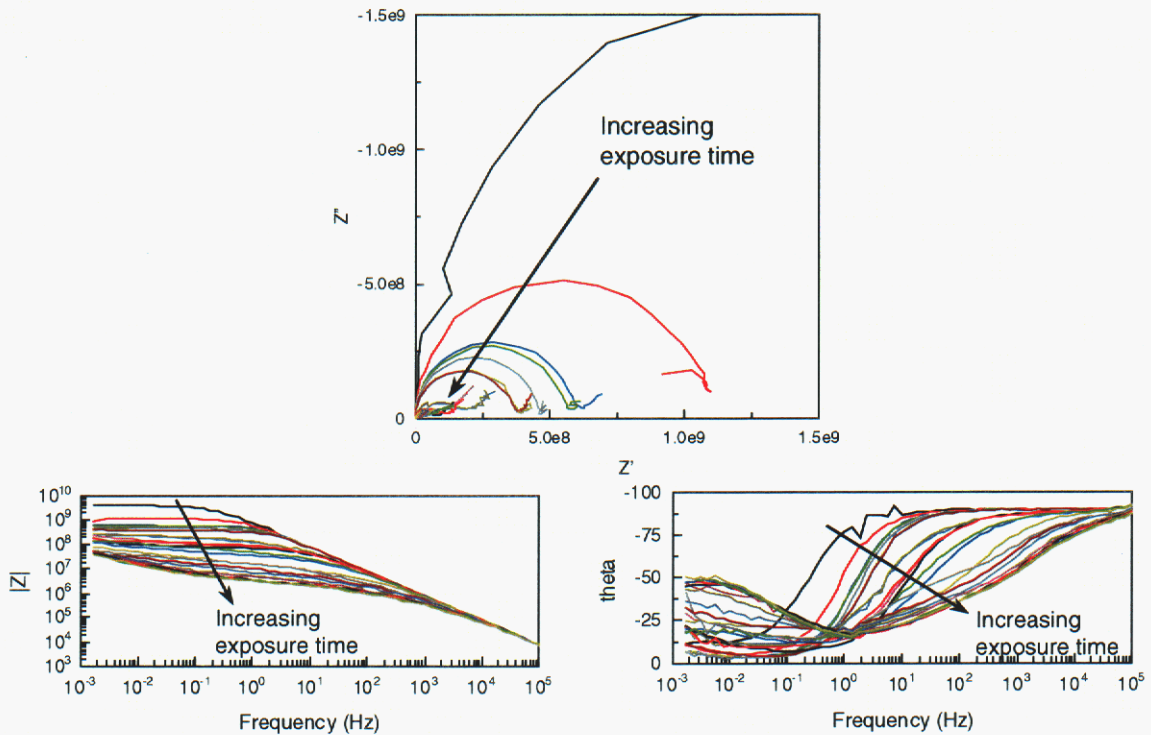


Figure 63 EIS data for Al|Cu—Cu|Al electrode in 85%RH and 20 ppb Cl₂.

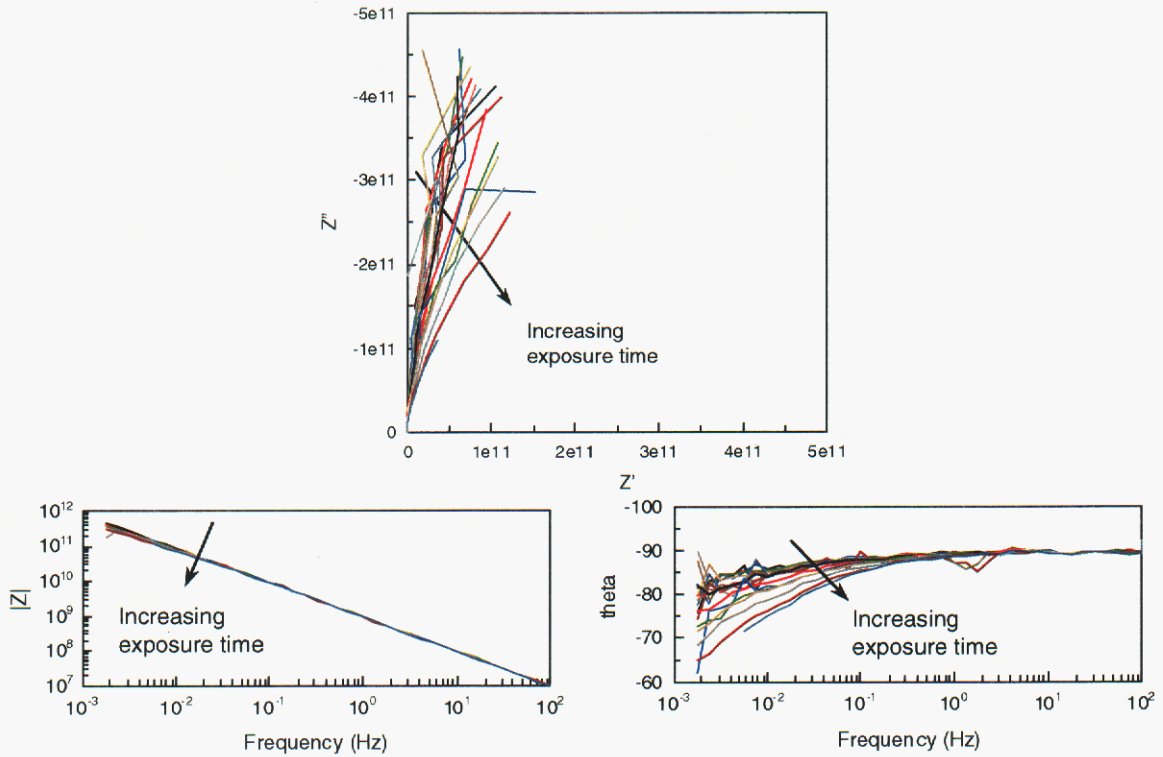


Figure 64 EIS data for Cu|Al—Al|Cu electrode in 85%RH and 20 ppb Cl₂.

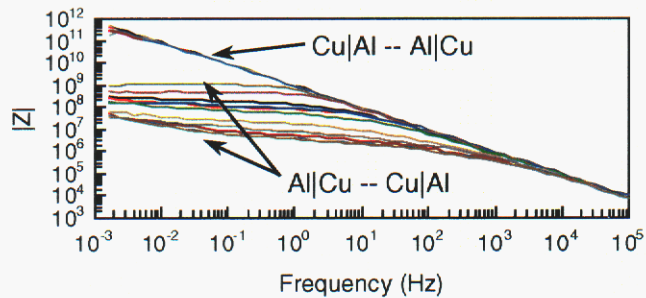


Figure 65 Comparison of EIS data in the Bode magnitude format for a Cu|Al—Al|Cu and a Al|Cu—Cu|Al electrode in 85%RH and 20 ppb Cl₂. Spatial arrangement has a dominant effect on the impedance response.

One hypothesis for the difference in behavior is that the electrolyte layer thickness is controlled by local chemistry differences.. If the surface tension were a strong function of electrolyte pH then perhaps a heterogeneous pH could result in thin regions of electrolyte. To test this hypothesis contact angles were measured as a function of solution pH on Al, Cu and various insulators used in the construction of the atmospheric sense electrodes (Figure 66). Only the Al showed a dependence of contact angle on pH of the electrolyte. The data suggest that Al covered with an alkaline electrolyte would have a lower surface energy than the other materials. It can be envisioned that the

interface between regions of high and low surface energy would cause a discontinuity in the electrolyte coverage. If Al were adjacent to any of the insulating materials, a transition from low to high surface energy would exist at each of the interfaces. Conversely, if Cu were adjacent to the insulating material, the surface energy would remain fairly constant across the interface. This hypothesis also requires that the Al be in an alkaline pH region. Once the Cu polarizes the Al to a potential where pits can initiate, then both the Cu and the unpitted Al can act as cathodes. Thus, the actively pitting regions of the Al would become acidic (due to metal ion hydrolysis) and the surrounding regions could have an alkaline pH (due to O₂ reduction). No direct evidence exists to support this hypothesis; however, at the moment no other plausible explanations have been developed.

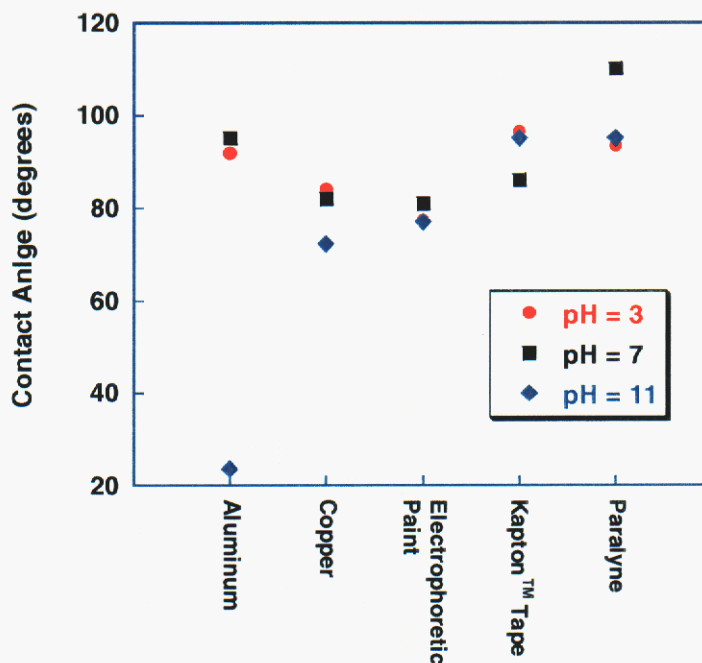


Figure 66 Contact angle measured as a function of pH for various electrode materials.

3.4.7 Al-Cu galvanic couple electrodes

Electrodes were constructed from electrically isolated foils of Al and Cu in order to make measurements of the galvanic current that flows between these materials as a function of RH and Cl₂ concentration. The galvanic current measurement is truly non-perturbing and is intended to yield information on the severity and type of corrosion that occurs on the anode material (Al in this case). Information was obtained on the behavior of electrodes at fixed RH, as a function of increasing RH and as a function of decreasing RH. The Cl₂ concentration was held fixed for each experiment.

The sensitivity of the galvanic current measurement at high RH was assessed by exposing an Al-Cu couple to 85%RH and 20 ppb Cl₂. The top graph in Figure 67 shows

the current as a function of exposure time. Significant localized corrosion is observed after about 5000 s of exposure. However, close examination of the current trace reveals significant corrosion activity at much earlier times. As early as 262 s into the exposure an anodic transient is discernable (Figure 67, bottom graph). The size of the local dissolution event can be estimated by integrating the area under the anodic spike. If the event is assumed to be a hemispherical pit, the diameter of the pit would be approximately 40 nm. The integrated charge also corresponds to material loss of 4.7×10^{-17} grams (47 ato-grams). This excellent sensitivity is made possible because the background current is so low in this experiment (i.e., 8 pA). By comparison, a standard (1 cm^2) Al electrode exposed to an aqueous environment will have a background current in the range of 10^{-6} to 10^{-5} A. In that case, the anodic spike from Figure 67 would be at least 10^6 times smaller than the background current and could not be resolved.

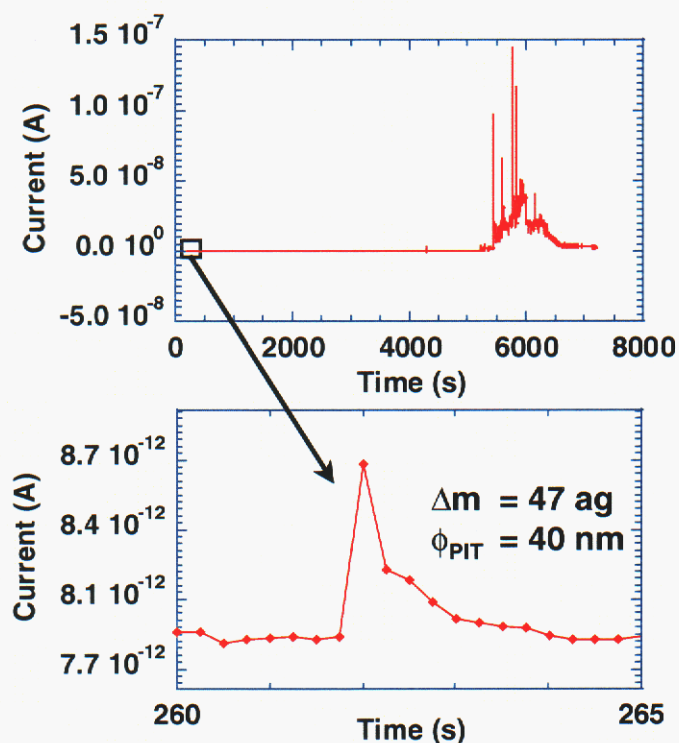


Figure 67 Galvanic current for Al-Cu couple exposed to 85%RH and 20 ppb Cl_2 . Very small changes can be detected due to the low background current.

The response of an Al-Cu couple to RH was examined initially by exposing a sample to 0%RH and 20 ppb Cl_2 then periodically increasing the RH. Figure 68 shows the galvanic current as a function of RH. The current measured at 0% RH was within 25 fA of the current for the potentiostat with no leads connected. This was taken as a zero value for current. Increasing the RH in increments of 10%RH resulted in resolvable changes in current for each RH level examined. The current vs. RH follows an S-shape

at low RH. RH levels above 80% were not investigated in this experiment, but it is anticipated that current would become less sensitive to RH at the higher RH levels. The significant change in the curve occurs between 40% and 60% RH. It follows that this range would correspond to a critical RH for corrosion of the Al-Cu couple. Indeed, evidence for localized corrosion was not observed until the RH level reached 60% (Figure 69). In other experiments (i.e., Figure 72) however, localized corrosion was observed at an RH of 50% and 20 ppb Cl₂. It is possible that localized corrosion was not observed in the present case because of either a long induction time or because the electrode had been conditioned by the exposures at the lower RH levels. Nevertheless, the data indicate that the propensity for localized attack is extremely low (or nonexistent) below about 40%RH.

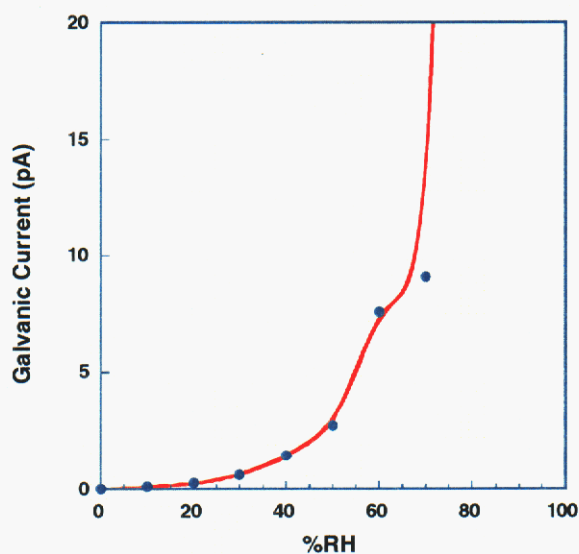


Figure 68 Galvanic current as a function of RH for Al-Cu couple exposed to 20 ppb Cl₂. The current for 80% RH (not shown on graph) is 125 pA. The RH was ramped from low to high in this experiment.

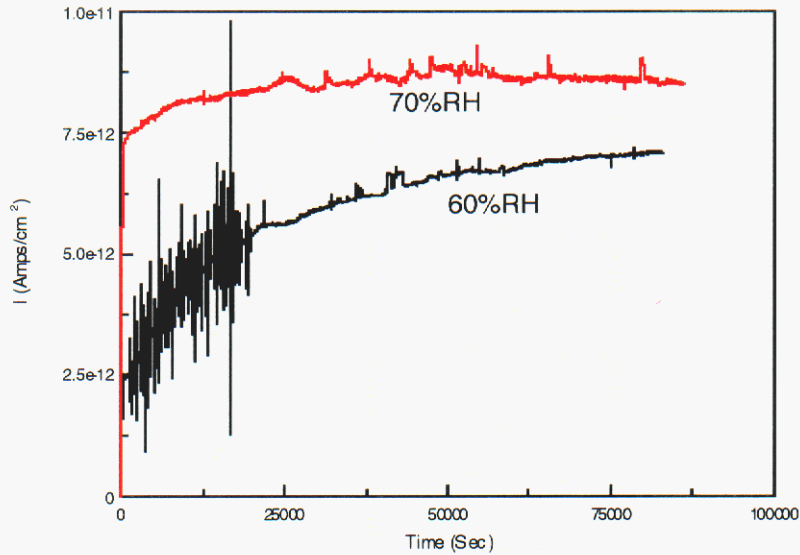


Figure 69 Galvanic current for Al-Cu electrode exposed to 20 ppb Cl_2 . No signs of localized corrosion were observed below 60%RH.

The current response of a second Al-Cu electrode to RH was examined by exposing the sample to 20 ppb Cl_2 and 50%RH, then periodically decreasing the RH. The average current response at each RH level is shown in Figure 70. Initially the sample was exposed to 50%RH and the data indicate that the current was slowly increasing during this exposure. While the current did not reach a steady state, the rate of change was very low (less than 2 pA in 4 days) so a decision was made to reduce the RH and continue with the experiment. At each subsequent RH the electrode underwent a very gradual drying-out process. The current vs. time curve did not appear to reach a steady-state value for any of the RH levels investigated. Thus these data can be viewed as indicators of the behavior of the electrode after a jump in RH but should not be used as estimates of the steady-state behavior at a particular RH. The data in Figure 68 provide a better indication, and better still would be data from a single sample at the RH level of interest.

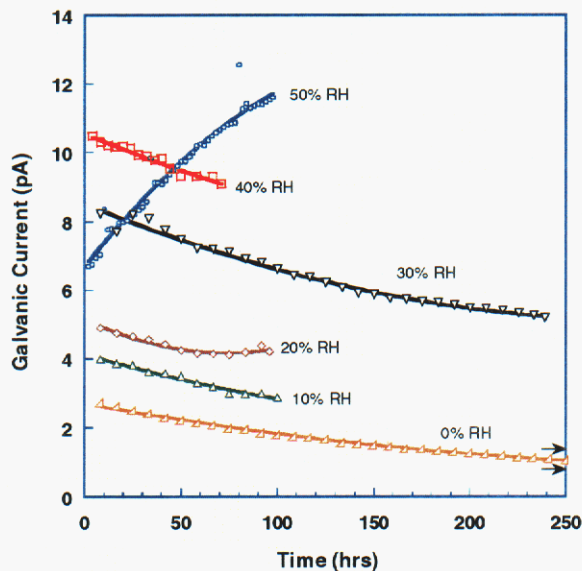


Figure 70 Galvanic current for Al-Cu electrode exposed to 20 ppb Cl_2 as a function of RH. RH was ramped from high (50%) to low (0%). Not all of the 0%RH data is shown.

The sample was exposed to the 0%RH environment for 384 hours without the current reaching the range of values observed when the potentiostat is disconnected. This was interpreted to mean that the sample still had an adsorbed electrolyte layer intact that was capable of supporting conduction between the electrodes. An effort was made to remove the electrolyte by baking the sample at a slightly elevated temperature. The sample was removed from the atmospheric test chamber and placed in an oven at 40°C , then returned to the test chamber for further current measurements. Three consecutive bake-outs of 67, 120 and 166 hours were performed, each followed by galvanic current measurements (Figure 71). The data indicate that galvanic currents were resolvable on the sample until the last bake-out. Thus a total of 353 hours (2 weeks) at 40°C was required to dry the sample. The drying-out behavior of this sample indicates that while water adsorption to the electrode surface may be reversible, it is kinetically hindered. No clear prediction can be made about the length of time to dry out at a particular humidity level; the data here can only serve to indicate the sluggishness of the process.

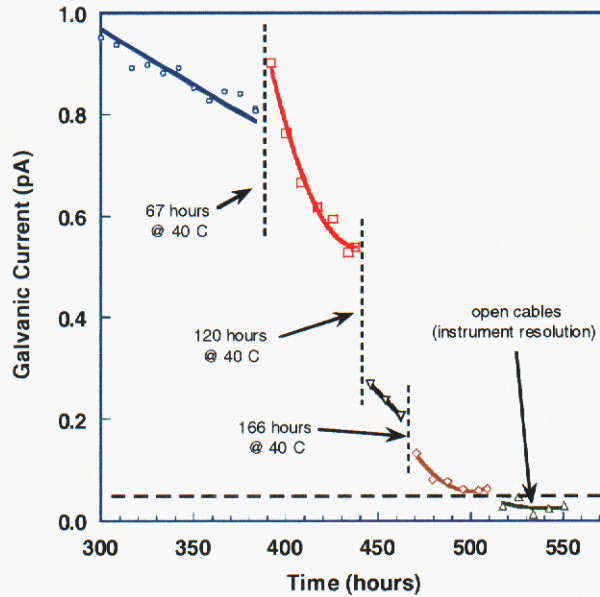


Figure 71 Galvanic current for Al-Cu electrode exposed to 20 ppb Cl_2 and 0%RH. Electrode had previously been exposed to 50%, 40%, 30%, 20% and 10% RH. At indicated break points, the sample was placed in an oven at 40°C for the specified length of time. Bake-out times are not cumulative; total bake-out time was 353 hours (~ 2 weeks).

Evidence of localized attack was observed in the current vs. time traces for the drying-out sample at 50% RH (Figure 72) and 30% RH (Figure 73). This is in contrast to the behavior observed for the sample exposed to increasing RH levels where current transients were not observed until exposure to 60% RH (Figure 69). As mentioned previously, the increasing RH sample may have been pre-conditioned by exposure to low RH, thus explaining the lack of pitting for this sample at 50%RH. Additionally, the decreasing RH sample most likely did not achieve equilibrium with the 30% RH environment when the pitting occurred. Thus, even though the environment was controlled at 30% RH, the sample may have had water layers commiserate with a 40% or 50% RH environment.

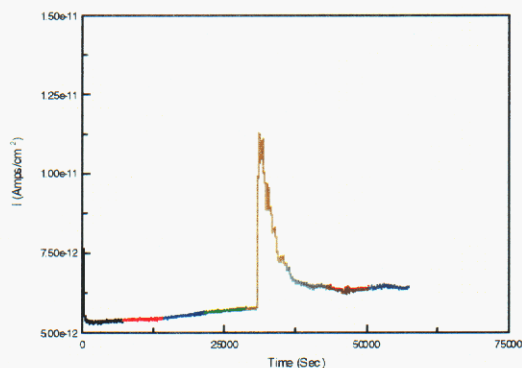


Figure 72 Galvanic current for Al-Cu electrode exposed to 50%RH and 20 ppb Cl₂; example of pitting. The 50%RH environment was the first exposure for this sample.

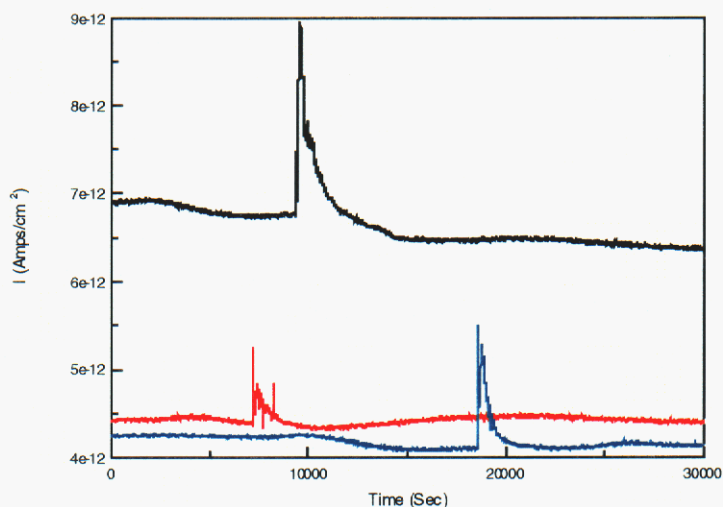


Figure 73 Galvanic current for Al-Cu electrode exposed to 30%RH and 20 ppb Cl₂; examples of pitting at low RH. The sample had been exposed to 50% and 40% RH prior to this exposure. The time axis is relative to individual data files and does not reflect the total duration of the exposure.

An Al-Cu galvanic couple electrode was also exposed to decreasing RH levels without intentionally added contaminants. There was no evidence of localized attack in the current data for this electrode. The current response of a function of RH was compared to that of the electrodes tested in the presence of 20 ppb Cl₂ and the results are plotted as log I vs. RH in Figure 74. All three data sets show an exponential dependence of current on RH although the slope is greater for the sample run from low to high RH. This is reasonable in light of the slow desorption kinetics for the samples run from high to low RH, and the fact that those samples never reach a true steady-state at any of the RH levels. The difference in magnitude of currents for the Cl₂ contaminated samples vs. the uncontaminated sample seem to support the enhanced current flow being due to Cl₂ adsorption and dissociation. However, the magnitudes of the currents from individual

Al-Cu samples are sensitive to variations in surface preparation, suggesting that only trends in sample behavior and not absolute magnitudes of values should be extracted from these plots.

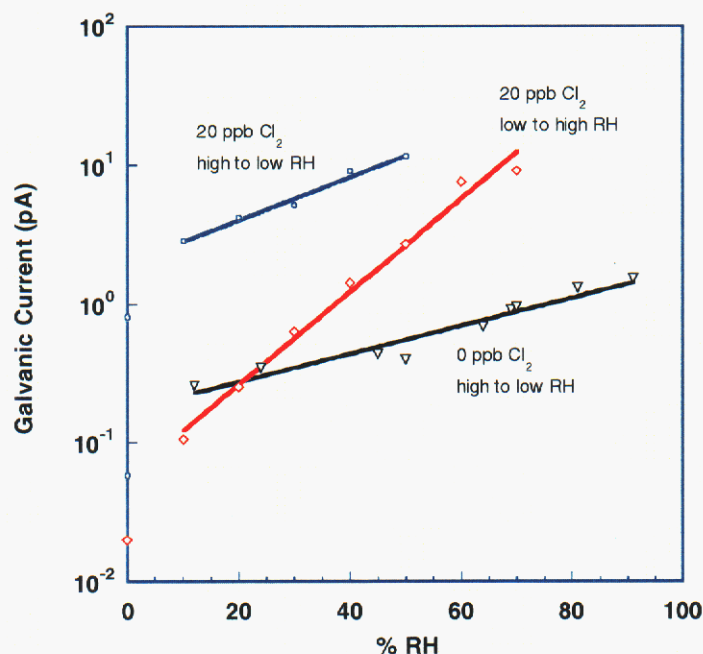


Figure 74 Galvanic current for Al-Cu electrodes exposed to various conditions. The slope for I vs RH is greater when RH is ramped from low-to-high rather than high-to-low, indicating the slower kinetics for electrolyte desorption.

It was not always possible to identify the localized corrosion sites on the Al foil in an Al-Cu couple electrode after an atmospheric exposure. In many cases, the size of the damage is much smaller than the electrode area and can not be located. However, in some instances coupling together alternating layers of Al and Cu enhanced the magnitude of the damage. Figure 75 shows the current trace of a multi-layer sample exposed to 60%RH and 20 ppb Cl₂ and the resulting damage. In this case the current transient is 6 orders of magnitude higher than the background current and the morphology and extent of damage is easily resolved. This is a contrived and atypical example of atmospheric corrosion damage, but serves to highlight the possible consequences of galvanic interactions, especially in thin-film applications.

The Al-Cu galvanic couple electrode proved to be the most sensitive means of measuring atmospheric corrosion over a wide range of RH levels. This technique should be generally applicable to studying material compatibility under atmospheric conditions and is capable of providing insight into the phase-space where atmospheric degradation could be problematic.

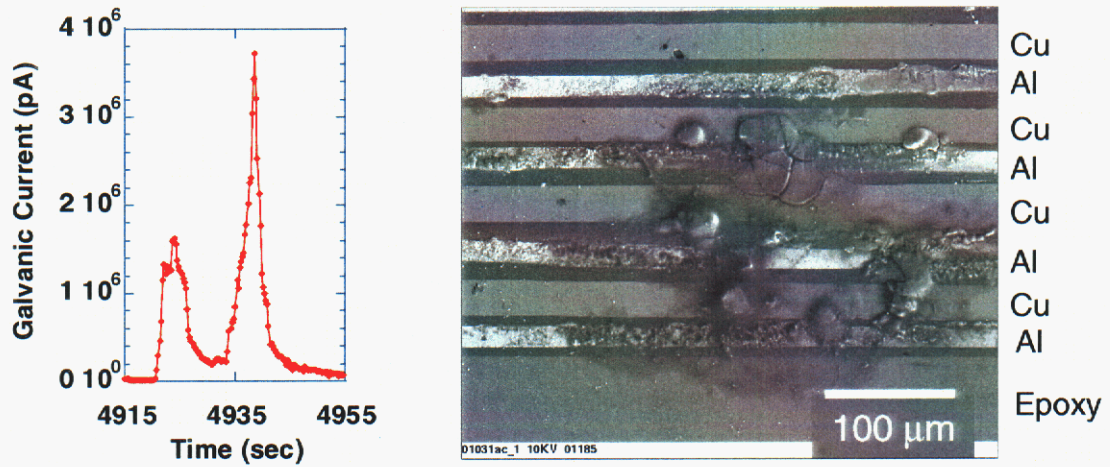


Figure 75 Multi-layer Al-Cu electrode exposed to 60% RH and 20 ppb Cl₂. The graph of current vs. time (left) shows a 10⁶ increase in corrosion current when the localized attack (right) occurred.

4 ELECTRICAL MODEL

4.1 Model Development and Implementation

At its most basic, the problem of pitting is an electrical one. Materials that are susceptible to pitting, as Al in this case, generally undergo attack in an aggressive environment and beyond a critical potential. The potential can be imposed externally, or can arise naturally when the susceptible anodic material is polarized by a cathodic material to which it is galvanically coupled. In the present problem, Al can be naturally polarized near Cu defects, and this work has addressed that phenomenon by modeling Al attack near Cu defects.

Ideally, the electrical response of a galvanic couple can be determined by a simple steady-state ohmic analysis, with the environmental (e.g. electrolyte) conductivity and material polarization behaviors as inputs. More specifically, the flow of charge through a uniform, linearly conducting medium is derived and described in the same manner as Fickian diffusion, i.e. by the Fourier equation,

Equation 4
$$\frac{\partial \phi}{\partial t} = \frac{\kappa}{\rho c} \nabla^2 \phi,$$

where ϕ is the potential, κ is the electrical conductivity, ρ is the mass density, and c is the specific electrical capacitance. In steady state, where the potential does not vary in time, the Fourier equation simplifies to the Laplace equation,

Equation 5
$$\nabla^2 \phi = \frac{\partial^2 \phi}{\partial x^2} + \frac{\partial^2 \phi}{\partial y^2} + \frac{\partial^2 \phi}{\partial z^2} = 0.$$

For very simple cases, Equation 5 can be solved analytically. However, most problems of technological interest demand a numerical approach.

In order to solve Equation 5, the computational domain is divided into an orthorhombic grid of nodes, as shown in two dimensions (for simplicity – all actual calculations are three dimensional) in Figure 76. In the example Figure 76, the computational domain is meant to represent a couple between Al (gray) and Cu (copper-colored) in contact with water (blue). The dots are the nodes, and the lighter coloration surrounded by dotted lines represents the effective extent of each component, such that a material boundary between two dissimilar nodes is halfway between the nodes themselves.

Consider the group of nodes in Figure 77a, and assume that they are in the interior of the electrolyte. The blue dots and numbers label nodes, and the black dots and numbers label points midway between each node. In order to solve Equation 5 at node #0, we make a finite difference approximation,

$$\text{Equation 6} \quad \frac{\partial^2 \phi}{\partial x^2} \Big|_0 \cong \frac{1}{\Delta x} \left(\frac{\partial \phi}{\partial x} \Big|_b - \frac{\partial \phi}{\partial x} \Big|_d \right) \cong \frac{1}{\Delta x} \left(\frac{\phi_2 - \phi_0}{\Delta x} - \frac{\phi_0 - \phi_4}{\Delta x} \right),$$

where Δx is the spacing between nodes in the x -direction and ϕ_j is the potential at node # j . A similar equation holds for the y -direction in Figure 76, and for the z -direction in a three-dimensional case. Combining Equation 6 with its analogue for the y -direction and rearranging provides an expression for the potential at node #0 as a function of the potentials at the neighboring nodes, i.e.,

$$\text{Equation 7} \quad \phi_0 \cong \frac{1}{2} \left(\frac{1}{\Delta x^2} + \frac{1}{\Delta y^2} \right)^{-1} \left(\frac{\phi_2 + \phi_4}{\Delta x^2} + \frac{\phi_1 + \phi_3}{\Delta y^2} \right).$$

Now consider the group of nodes in Figure 77b, where nodes #0, #1, and #3 are at the edge of the computational domain. We have no direct information about the potential field to the right of the boundary nodes, and so we must use boundary conditions to modify Equation 6 and Equation 7 for nodes at the domain boundaries. Specifically, the analogue to Equation 6 for Figure 77b is

$$\text{Equation 8} \quad \frac{\partial^2 \phi}{\partial x^2} \Big|_5 \cong \frac{2}{\Delta x} \left(\frac{\partial \phi}{\partial x} \Big|_5 - \frac{\partial \phi}{\partial x} \Big|_h \right) \cong \frac{2}{\Delta x} \left(\frac{\partial \phi}{\partial x} \Big|_5 - \frac{\phi_5 - \phi_9}{\Delta x} \right).$$

The analogous equation for the y -direction will look very much like the one for Figure 77a, i.e.,

$$\text{Equation 9} \quad \frac{\partial^2 \phi}{\partial y^2} \Big|_5 \cong \frac{1}{\Delta y} \left(\frac{\partial \phi}{\partial y} \Big|_e - \frac{\partial \phi}{\partial y} \Big|_g \right) \cong \frac{1}{\Delta y} \left(\frac{\phi_6 - \phi_0}{\Delta y} - \frac{\phi_0 - \phi_8}{\Delta y} \right)$$

Combining Equation 8 and Equation 9 yields an expression for the potential at node #5 in Figure 77b,

$$\text{Equation 10} \quad \phi_5 \cong \frac{1}{2} \left(\frac{1}{\Delta x^2} + \frac{1}{\Delta y^2} \right)^{-1} \left[\frac{2}{\Delta x} \left(\frac{\partial \phi}{\partial x} \Big|_5 + \frac{\phi_9}{\Delta x} \right) + \frac{\phi_6 + \phi_8}{\Delta y^2} \right].$$

A similar procedure yields expressions for the potentials at the y-boundaries and at the domain corners.

In this work, we consider three-dimensional computational domains with combinations of free surface, mirrored, and metal surface (consisting of Al and Cu) boundary conditions. The mirrored and free surface boundaries have zero potential gradients in the direction(s) perpendicular to the boundary plane(s) (plurals apply to domain corners). The boundary conditions at the metal surface are obtained from the polarization behavior of the various constituent materials in the following manner.

The continuum version of Ohm's law relates the potential gradient and the current density as

Equation 11
$$\frac{\partial\phi}{\partial x} = \frac{i_x}{\kappa},$$

where i_x is the current density in the x -direction and κ is the conductivity. Equation 11 immediately suggests the proper approach for applying boundary conditions at the metal surface. The polarization behavior of each material relates the potential to the current density. Thus, for any value of the potential at the metal surface, the polarization curve is used to determine the corresponding current density, which is in turn used in Equation 11 to obtain the potential gradient at (and perpendicular to) the metal surface, which is then used as the boundary condition in an equation like Equation 10. In fact, it is precisely the nonlinear polarization behavior of real materials, wherein the potential gradient at the material's surface depends on the value of the potential itself that prohibits a direct solution of Equation 5 and demands the approach taken here.

By examining Equation 7, Equation 10, and Equation 11 we can see that the only inputs to this model are the internodal spacings, the electrolyte conductivity, and the boundary conditions. The internodal spacing (and thus the simulation domain size) and the conductivity are chosen to appropriately reflect the problem of interest. In problems with Al and Cu, the polarization behaviors are taken from the experimental data shown in Figure 78a, and in practice the metal boundary conditions (i.e. current densities) for an arbitrary potential value are obtained by linearly interpolating between the experimental data points.

Armed with finite difference approximations like those in Equation 7 and Equation 10 for each node in the computational domain, and with the boundary conditions discussed above, an approximate solution to Equation 5 can be obtained in a variety of ways. If the boundary conditions are fixed, i.e. either the potentials or the potential gradients are constant at each boundary node, then a direct numerical solution to Equation 5 is possible. This approach will be discussed in a later section, and we will focus first on cases where nonlinear boundary conditions are present, e.g. due to complex polarization behaviors. In these cases, a solution to Equation 5 is obtained using an iterative Gauss-Seidel method.¹⁷ This method begins with an initial guess for the potential field, and then iteratively corrects the guess until it reaches steady state. In this

sense, the method uses a pseudo-time which serves to move a guessed solution to the correct one. At each iteration, the computational domain is “scanned” in order of increasing x , then y , then z . Thus, returning to the example in Figure 77a, the evaluation of the potential at node #0 for iteration # n would be

$$\text{Equation 12} \quad \phi_{0,n} \cong \frac{1}{2} \left(\frac{1}{\Delta x^2} + \frac{1}{\Delta y^2} \right)^{-1} \left(\frac{\phi_{2,n-1} + \phi_{4,n}}{\Delta x^2} + \frac{\phi_{1,n-1} + \phi_{3,n}}{\Delta y^2} \right),$$

where $\phi_{j,n}$ is the potential at node # j and iteration # n . Notice that the iterative Gauss-Seidel method is a modification of iterative Jacobi in that up-to-date values for the potential field are used as soon as they are available. (Inherent in Equation 12 is the spatial order of the evaluation, i.e. in increasing x , y , and z , as described above.) Appropriate modifications to Equation 12 are made at the domain boundaries, as in Equation 10. Equation 12 is iterated until the changes in the potential field are below a tolerable level. (In practice, this tolerance is placed on the sum of the percent changes to the potentials at all nodes after each iteration, and tolerable values of this sum are generally less than 0.000001%.)

This approach on its own is not particularly efficient, and measures must be taken to speed it up. In this study, we employ two techniques to accelerate the convergence of the Gauss-Seidel iterative scheme. The first involves simply setting the initial guess for the potential field to the corrosion potential, which is obtained from the intersection of the (area-scaled) polarization curves. This creates an initial guess for the potential field that is, on average, near the correct solution by definition.

The second technique involves multigridding¹⁸ the simulation space. This has numerous advantages, but our primary concern in this regard is to quickly obtain an approximate solution before attempting to reach full convergence on the simulation grid of interest. Three levels of grid refinement are used in each simulation: the finest grid, which is the one we “care” about, with $N_x N_x N$ nodes; a coarser “medium” grid with $5 \times 5 \times 5$ nodes; and the coarsest grid of $3 \times 3 \times 3$ nodes. Limited numbers of iterations are performed in series at various levels of grid refinement, and each set of iterations on a new grid starts with potential field data from the last set of iterations on the previous grid. When the grid is coarsened, information at nodes that are present in the finer grid but not in the coarser one, is discarded. When the grid is refined, information at nodes that are not present in the coarser grid but are in the finer, are linearly interpolated from the data in the coarser grid.

Since the relative electrode surface areas can change when the grid is coarsened or refined, the boundary conditions at the electrode surfaces (i.e. the current densities from the polarization curves) are scaled accordingly. For example, if the finest grid has a $A:B$ ratio in Al:Cu surface area, then all calculations on a grid with a $C:D$ area ratio would have the Al current densities scaled by A/C and the Cu current densities by B/D .

This ensures that the system's corrosion current and potential do not change when the grid is coarsened or refined.

The same multigridging schedule is used in all of the iterative simulations presented here. Specifically, if the finest, medium, and coarsest grids are denoted **F**, **M**, and **C**, then the multigridging schedule used here is **F** → **M** → **C** → **M** → **C** → **M** → **F**. The final set of iterations on the finest grid is allowed to progress until the solution for the potential field converges to the desired tolerance. This approach substantially accelerates the convergence of the solution to its steady state.

4.2 Results for Al/Cu

Before examining results from this model, it is useful to determine what we can expect from the types of problems of primary interest here, i.e. polarization behavior of microscale Al/Cu couples in aqueous salt solutions. Consider the schematic polarization curves in Figure 78b. The curves relate the potential to the current (and *vice versa*) at the surfaces of Al and Cu electrodes. (The current is, of course, simply the current density scaled by the appropriate electrode surface area.) When the anode and cathode in Figure 78b are placed in electrical contact, they will polarize one another such that their potentials and current densities are “forced” to values near the intersection point in the polarization curves. Because the anodic currents are positive and the cathodic negative, charge will flow between the anode and the cathode, and the potential difference between them will depend on the amount of current flowing and on the resistance along the current's path.

Since the process must, at its most basic level, obey these simple principles, it is possible to roughly estimate the magnitude of the “IR drop” between the anode and cathode in an ideal system. For example, consider two electrically connected materials with polarization curves, similar to those in Figure 78b, which intersect at a current density of 1 mAmp/cm². If the surfaces in electrical contact are of equal 1 cm² areas, then the current at the curves' intersection would simply be 1 mAmp. Now imagine that the electrical connection between the materials has a conductivity of 10 (mΩ cm)⁻¹, and that the materials are separated by 1 cm. Then the resistance between the materials is 0.1 mΩ. Thus, if $I = 1$ mAmp and $R = 0.1$ mΩ, then $\Delta V = 0.1$ μVolt. The numbers in this example were chosen to be roughly comparable to those of interest here, and clearly this yields a relatively small IR drop. The salient point is that when two materials with small surface areas and low corrosion current densities are electrically connected by a relatively conductive medium, the system simply cannot support large IR drops between the two electrodes. The numbers simply do not “work out that way.” This result assumes, of course, many idealities, not the least of which is the homogeneity of the morphology and properties of the individual electrode surfaces.

To study the polarization behavior of Cu and Al microelectrodes we use a computational domain like that in Figure 79. The actual computational volume is outlined

in red, and the rest of the picture shows the simulated Cu defect array that is created when mirrored boundary conditions are applied to the faces of the computational domain in the directions parallel to the metal surface. We will consider only one medium, i.e. a water electrolyte with 50 mM NaCl and a conductivity of $0.006322 (\Omega \text{ cm})^{-1}$, so the conducting medium is the same in all Al/Cu calculations. Thus, the variations we will consider deal primarily with electrode and electrolyte geometry.

4.2.1 Effects of Electrolyte Thickness

To study the impact of the thickness of the water layer on polarization behavior, a uniform Cu defect array geometry was chosen to have a Cu dot diameter of $170 \mu\text{m}$ and center spacing of $320 \mu\text{m}$. The size of the simulation domain (see Figure 79) is $17 \times 17 \times 17$ nodes, and the thickness of the electrolyte layer was varied in decades from 1 cm to $0.1 \mu\text{m}$. Figure 80a shows a surface plot of the potential at a Cu dot with a $1 \mu\text{m}$ thick layer of water and 50 mM NaCl. The data in Figure 80 was mirrored to create four adjacent simulation domains, so that the potential over an entire Cu dot (bounded in white) can be seen. Figure 80b shows the IR drop (i.e. potential difference) between the center of the Cu dot and the point on the Al farthest from the Cu, as a function of the electrolyte thickness.

The IR drop increases as the electrolyte thickness decreases. The electrolyte provides the electrical path for the transfer of charge between the Cu and Al surfaces. As this charge path is constricted, its effective resistance increases and the voltage difference also increases ($V = IR$). Scaling the polarization curves in Figure 78a by the surface areas in a single simulation domain reveals that the corrosion current in this system is approximately 2 nAmps. The resistance through $160 \mu\text{m}$ of 50 mM NaCl in water is approximately $10 \text{ k}\Omega$. From these values, the IR drop can be estimated at 0.02 mVolts, which is near the apparent asymptote in Figure 80b.

4.2.2 Effects of Cu Defect Spacing and Area

Changes to the electrode geometry generally involve changes to both the relative electrode areas and to the electrode spacing. Therefore, we will consider both effects in the same subsection. Figure 81 shows the electrical steady-state, as a function of the Cu spacing, at the surface of an array of $110 \mu\text{m}$ diameter Cu dots on Al covered by 1 mm of water with 50 mM NaCl. Variations in the Cu spacing were achieved by holding the size of the Cu defect constant while increasing the size of the simulation domain from $7 \times 7 \times 21$ nodes to $25 \times 25 \times 21$ nodes. As the spacing between the (constant area) Cu dots increases in Figure 81, the Al:Cu area ratio increases and the Al curve in Figure 78a shifts to the right relative to the Cu curve. The impact of this relative area change on the potential and IR drop at the electrode surface can be understood by considering how the shifts to the polarization curves affect their intersection. If we examine the polarization curves in Figure 78a, and focus on their intersection as we imagine shifting the Al curve to the

right while fixing the Cu curve, we can clearly see that the corrosion current and potential (i.e. the current and potential at the curves' intersection) will increase and decrease, respectively.

As discussed above, these small systems with low corrosion currents cannot support large IR drops, and this is evident in Figure 81. The IR drops in Figure 81a are in the nAmp range, and track the corrosion current (obtained from the intersection of the area-scaled polarization curves) very closely. The average potential at the electrode surface, shown in Figure 81b, is almost exactly the same as the corrosion potential and is nearly constant across the electrode surface. (Note that the IR drop, which is the total potential difference across the electrode surface, is in the sub-mVolt range. Error bars corresponding to the standard deviations are shown on the average potential data, but are in the μ Volt range and are smaller than the plotting symbols.) The “knee” at around -400 mVolts in the Cu polarization curve in Figure 78a is clearly reflected in Figure 81b.

Figure 82 shows the electrical steady-state, as a function of the Cu surface area, at an array of Cu dots spaced $480 \mu\text{m}$ apart on Al covered by $1 \mu\text{m}$ of water with 50 mM NaCl . These simulations were performed in a domain of $25 \times 25 \times 21$ nodes. Increasing the Cu area has the opposite effect from increasing Cu spacing, for exactly the reasons given above. The IR drop in Figure 82a is larger than in Figure 81a because the water layer is one thousand times thinner (see Figure 80b), and does not track the corrosion current as closely as in Figure 81a. (The standard deviations across the electrode surface of the average potential are plotted as error bars in Figure 82b, and are anywhere from one to three orders of magnitude larger than in Figure 81b, but are still so small that they are not clearly visible behind the plotting symbols.) Unlike in Figure 81b, the potential varies enough across the electrode surface so that the average electrode potential in Figure 82b deviates slightly from the corrosion potential. As before, much of the behavior in Figure 82 can be understood by examining the polarization curves in Figure 78a.

4.2.3 Effects of Pitting Sites

Although this model cannot directly address the complex and dynamic physics of pit initiation and growth, it can provide some information about the electrical aspects of pitting. Specifically, if we presume a “polarization” behavior for a stable pit, then we can incorporate this information into the present model and treat the pit as simply a third type of material on the electrode surface. This is clearly of limited validity, but it can provide information about the effects of a pit on the electrical steady state of the Al/Cu system, and *vice versa*.

For this purpose, we make a crude linear approximation to the polarization curve of an Al pit, based on the data in Reference 19, such that it passes through the points (-1 Volts, 0 Amps/cm^2) and (0.5 Volts, 1 Amps/cm^2). To model the effects of pit size on the system response, a single node on the electrode surface is made to obey the “pit” polarization response, and the current density at the pit node is scaled by the desired pit size relative to the electrode surface area per node. So, if the pit is to be $1/100^{\text{th}}$ the size of

a node, then the polarization response for the node with the pit will be linear and pass through (-1 Volts, 0 Amps/cm²) and (0.5 Volts, 0.01 Amps/cm²).

Figure 83 shows the effect of a potential field at the electrode surface, with and without a 1 μm^2 pit, for an array of 330 μm diameter dots spaced 480 μm apart in 1 μm of 50 mM NaCl water. (Only a single simulation domain is shown.) The polarization potentials for the pit are low relative to those for Al and Cu (Figure 78a), so the presence of the pit lowers the overall potential noticeably. Taking into account the mirrored boundary conditions, it is clear that there is one pit per simulation domain in Figure 83c, and one pit per every four simulation domains in Figure 83b, so the suppression of the potential in Figure 83c is stronger than in Figure 83b. The pit site has a strong anodic current density, but because it is relatively small, it affects the Al and Cu current densities only slightly and is not shown.

Figure 84 shows the ratio of the total anodic to cathodic current on the electrode surface as a function of the "size" of the pit (see above). In steady state, the anodic and cathodic currents must balance one another (i.e. be equal in magnitude and opposite in sign) so that charge is not accumulating in the system. When the currents do not balance, then there is no electrical equilibrium (according to the allowable polarization behaviors) between anodic and cathodic materials. In Figure 84, values of the current ratio that deviate from unity represent imbalanced current, and this means that there is insufficient cathodic current to support the anodic current requirements of the pit. This information is useful because it provides a qualitative approximation (assuming reliable polarization data for a pit) to the largest pit that can be electrically supported by a particular Cu/Al system. It is evident in Figure 84 that a pit of any appreciable size causes the current ratio to deviate from one, and thus it is not possible from these results to obtain a meaningful estimate of the maximum sustainable pit size. However, it is important to note that this analysis does not account for transient chemical and diffusive effects that might contribute strongly to pit stability.

4.3 Other Applications: Microelectronic Device Performance

Although the focus of this work has been on corrosion of Al in the presence of Cu defects, the model can be applied to a wide variety of problems. One such application is electrical degradation due to corrosion in plastic encapsulated microelectronics (PEMs).²⁰ These systems contain Au wires bonded to Al pads, and heat treatment produces various AuAl intermetallic compounds (primarily Au₅Al₂, Au₂Al, and Au₄Al) near the wire/pad interface. These intermetallics modify (by increasing) the resistivity of the bond, and they also accelerate corrosion of the Al at the interface. Although a model like the one described above cannot address the fundamental mechanisms of this type of corrosion, it can help predict the impact of corrosion and intermetallic formation on device performance. In particular, as described above, the model developed here calculates potential fields and current flow given information about geometry, conductivity, and boundary conditions. Thus, if we know or postulate the microstructure of the bond pad, and the conductivities of each component (Au, Al, intermetallic, and corroded Al), then we can calculate its electrical properties.

Since this application involves an assembly of discrete solid materials, we must make a modification to the model equations to account for variations in conductivity throughout the computational domain. This modification is introduced by rewriting Equation 4 for the case of a nonuniform, linearly conducting medium, such that

$$\text{Equation 13} \quad \frac{\partial \phi}{\partial t} = \frac{1}{\rho c} \nabla(\kappa \nabla \phi).$$

If the only variations in conductivity are discontinuous, e.g. for an assembly of different but individually uniform materials, the requisite modifications to Equation 10 are straightforward:

$$\text{Equation 14} \quad \phi_5 \equiv \frac{1}{2} \left(\frac{2\kappa_{5,9}}{\Delta x^2} + \frac{\kappa_{5,6} + \kappa_{5,8}}{\Delta y^2} \right)^{-1} \left[\frac{2}{\Delta x} \left(\kappa_5 \frac{\partial \phi}{\partial x} \Big|_5 + \frac{\kappa_{5,9}\phi_9}{\Delta x} \right) + \frac{\kappa_{5,6}\phi_6 + \kappa_{5,8}\phi_8}{\Delta y^2} \right],$$

where $\kappa_{j,k}$ is the average of the conductivities at nodes # j and # k , and we have again used the example in Figure 77b. The terms in Equation 14 suggest the appropriate modifications at other locations in the computational domain.

Our goal is to calculate the net resistivity of an assembly of solids, so the boundary conditions consist of free surfaces, with constant current (i.e. constant potential gradient) imposed on two opposing faces of the computational domain to force the flow of current through the assembly. Because these boundary conditions are constant, we can solve Equation 14 directly using a linear biconjugate gradient technique²¹ to obtain a solution for the potential field.

This approach was used to simulate the electrical degradation of an idealized Al bondpad containing intermetallic inclusions. The inclusions were modeled as cylinders that extend through the thickness of the Al. Uniform radial corrosion was imposed at the interfaces between the Al and the intermetallic, and the resistance of the Al pad was calculated as a function of time (as corrosion progressed). Figure 85a shows examples of cross-sections through the simulated systems. Yellow is Al, red is intermetallic, and green is corroded. The resistivities of these three phases were taken as 0.3125, 0.05, and 0 $\mu\Omega$ cm, respectively. The phase boundaries are marked in black. A constant current of 100 mA was applied to the top and bottom edges of the simulation domain (as it is depicted in Figure 85a). The effective resistance of the system was calculated by averaging the potentials at the top and bottom faces of the simulation domain (see Figure 85a), taking the difference between these two averaged potentials, and dividing by 100 mA. The results of this calculation are shown in Figure 85b. The discontinuities in the resistance occur when the corroded regions of two cylinders impinge and pinch off a region of high-conductivity Al, and this behavior is similar to that observed experimentally.²⁰

4.4 Conclusions from the Electrical Model

The results presented above serve primarily to illustrate the capabilities of the model developed herein. However, they also lead to an important conclusion about the behavior of pit initiation in real Al/Cu systems. The microelectrodes considered in this study are small. As determined experimentally, the constituent Al and Cu materials exhibit low corrosion current densities. And the NaCl-containing water electrolyte is relatively conductive. These facts, when combined, mean that these systems simply cannot support substantial IR drops (unless the thickness of the water overlayer is decreased substantially to restrict charge transfer through it).

When the potential at the electrode surface is so uniform, it is very unlikely to find a system where part of the Al is electrically prone to pitting and the rest is not. However, real-world observations of localized Al pitting in these types of systems are common. Assuming that the galvanic response of these systems obeys the classical laws of charge transfer discussed above, then this localized pitting could likely be due to inhomogeneities in the surface morphology or material properties. For example, different locations on the electrode surface will certainly not be morphologically and structurally identical, nor will they exhibit an identical local polarization response, nor begin to pit at the same potential. Perhaps it is for this reason that very small Al samples, which are more likely to be homogeneous, can have extraordinarily high pitting potentials. In addition, it is conceivable that morphological features and/or variations in local surface properties could explain dramatic Al corrosion at the interfaces with Cu defects, despite the fact that these also happen to be the locations on the Al that are highest in potential.

In short, it is important to realize that localized pit initiation might not necessarily be caused by local electrical potential, but rather could be due to the inherent inhomogeneities of real materials.

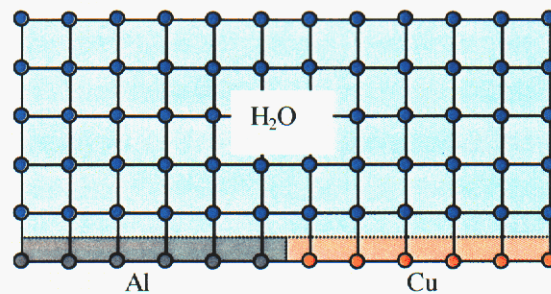


Figure 76 Schematic of a two-dimensional finite difference grid of Al and Cu electrodes in water. Blue dots are nodes in the water, gray dots are nodes at the Al electrode surface, and copper-colored dots are nodes at the Cu electrode surface. Light blue regions are areas representing water, light gray is Al, and light copper is Cu.

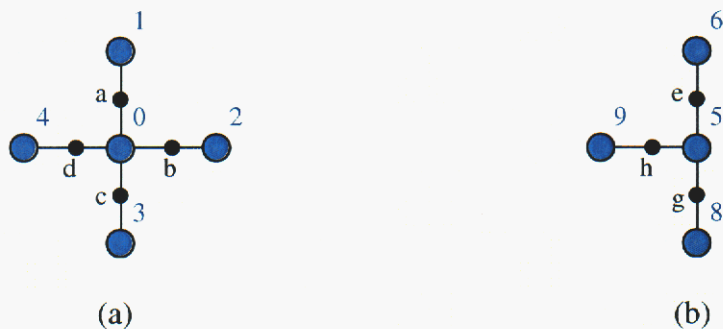


Figure 77 Clusters of adjacent nodes a) in the bulk of the water region in Fig 1, and b) at the edge of the water region. Blue dots are nodes and black dots are points midway between each node.

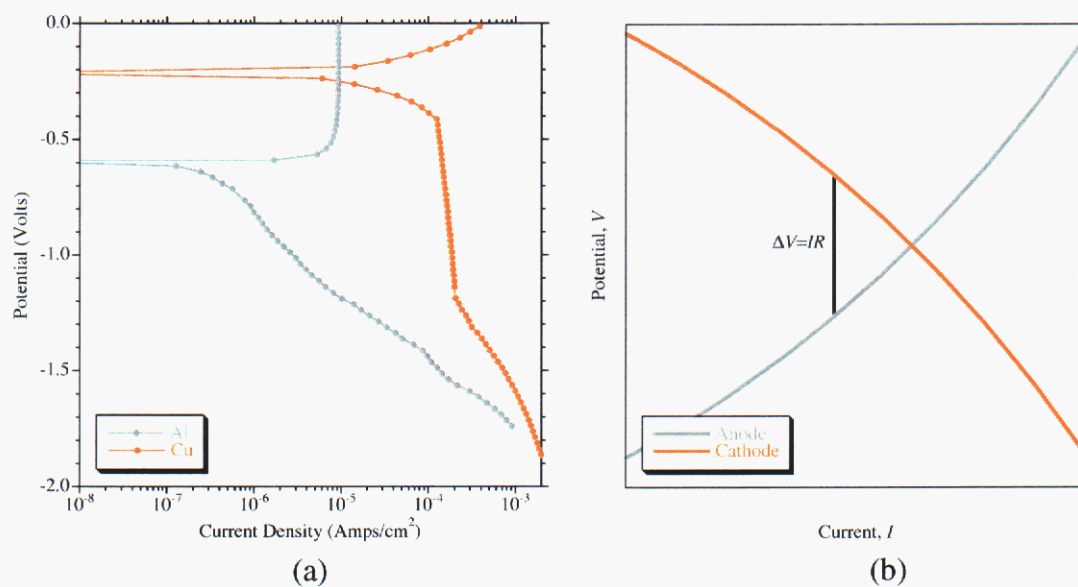


Figure 78 Polarization curves a) for Al and Cu used in this study, and b) simplified for illustration. The cathodic (Cu) curve has negative currents but is plotted as positive for clarity.

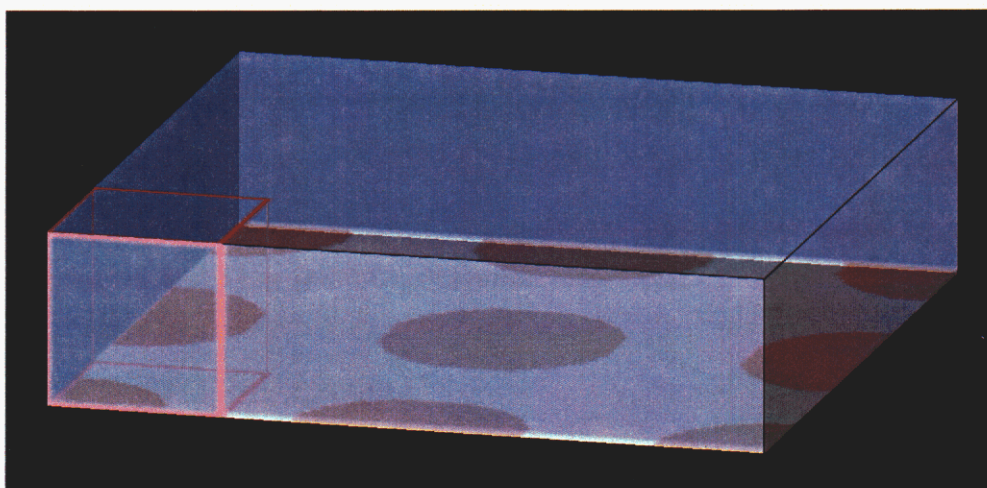


Figure 79 The simulation space for Al and Cu electrodes in water. Cu is copper-colored, Al is gray, and the water electrolyte is translucent blue. Reddish lines demarcate the size of a single computational domain, and the remaining space depicts the simulated Cu defect array created by the mirrored boundary conditions at the faces of the computational domain.

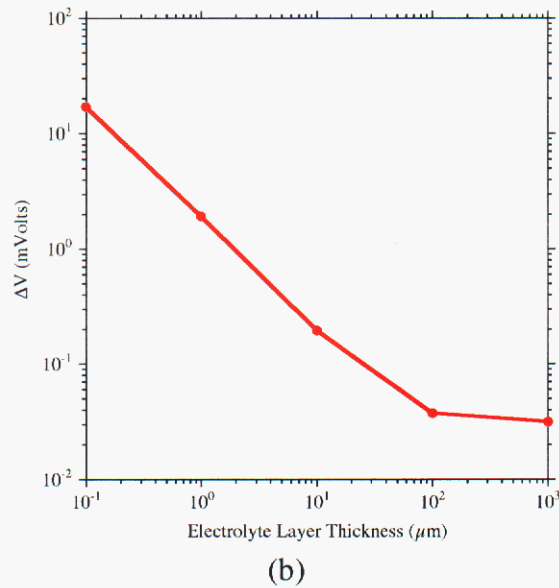
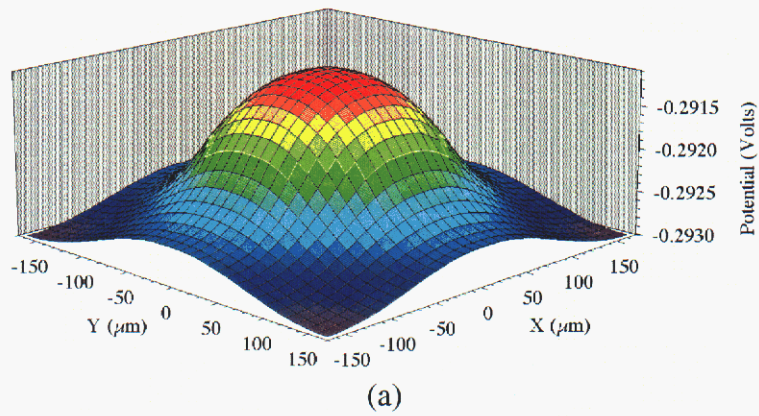


Figure 80 Plots of a) the potential field around one Cu dot, and b) the IR drop between the Cu and Al as a function of the thickness of the electrolyte. The simulated system is an array of Cu dots, with 170 μm diameter and spaced 320 μm apart, on Al covered by water with 50 mM NaCl.

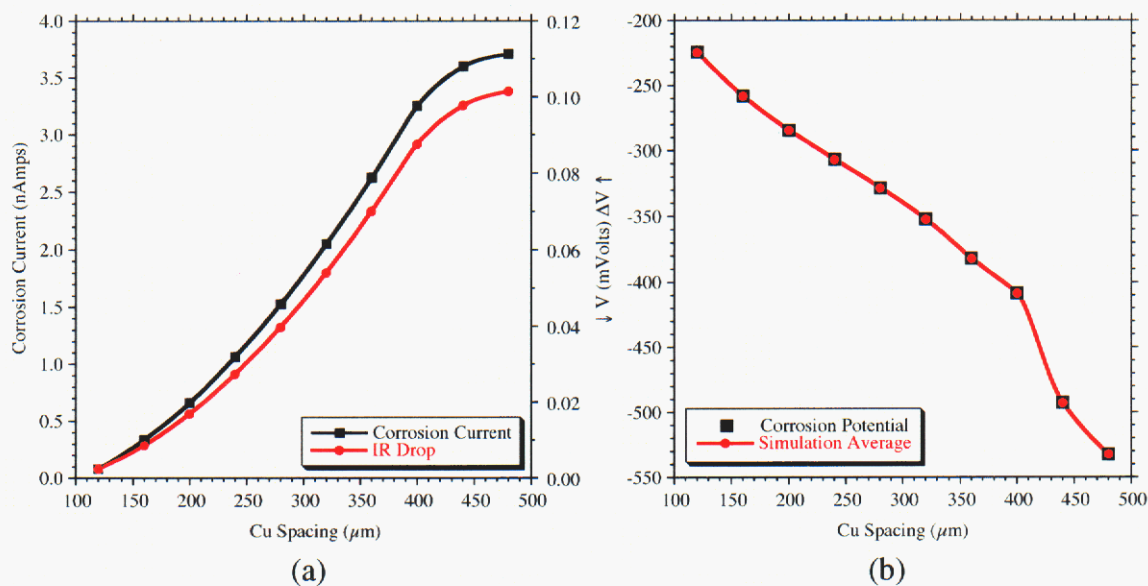


Figure 81 Plots of a) the corrosion current and IR drop, and b) the corrosion potential and average simulated potential, at the electrode surface as functions of the Cu defect spacing. The simulated system is an array of Cu dots with $110\ \mu\text{m}$ diameter on Al covered by 1 mm of water with 50 mM NaCl.

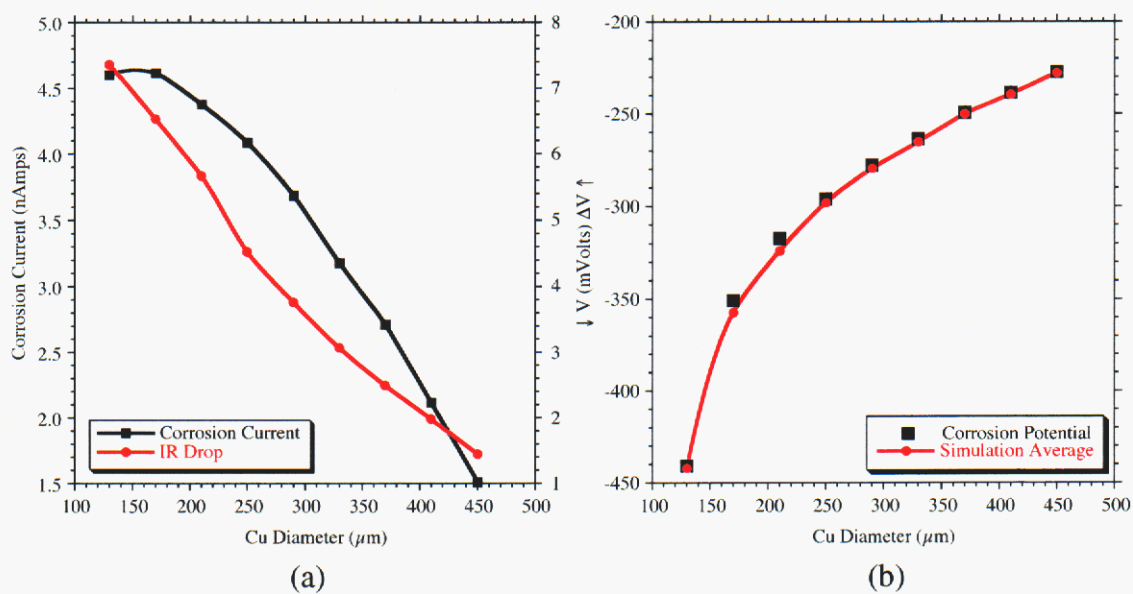


Figure 82 Plots of a) the corrosion current and IR drop, and b) the corrosion potential and average simulated potential, at the electrode surface as functions of the Cu defect diameter. The simulated system is an array of Cu dots spaced 480 μm apart on Al covered by 1 μm of water with 50 mM NaCl.

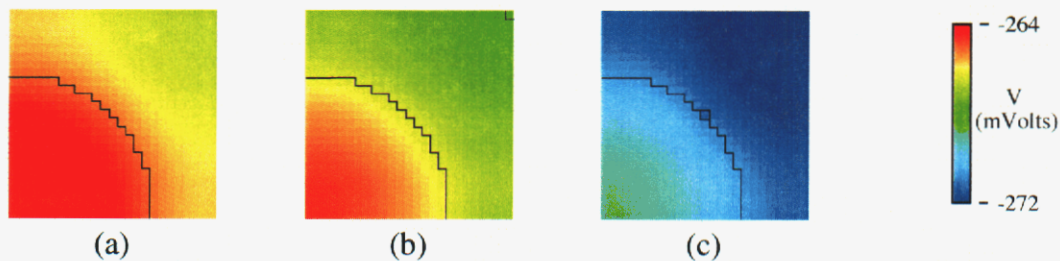


Figure 83 Potential fields a) without a pit, b) with a $1 \mu\text{m}^2$ pit between the Cu dots, and c) with a $1 \mu\text{m}^2$ pit at the edge of the Cu. Black lines demark boundaries between Al, Cu, and the pit. The large circular region is the Cu, the small square is the pit, and the rest is Al. The simulated system is an array of Cu dots with $330 \mu\text{m}$ diameter spaced $480 \mu\text{m}$ apart on Al covered by $1 \mu\text{m}$ of water with 50 mM NaCl .

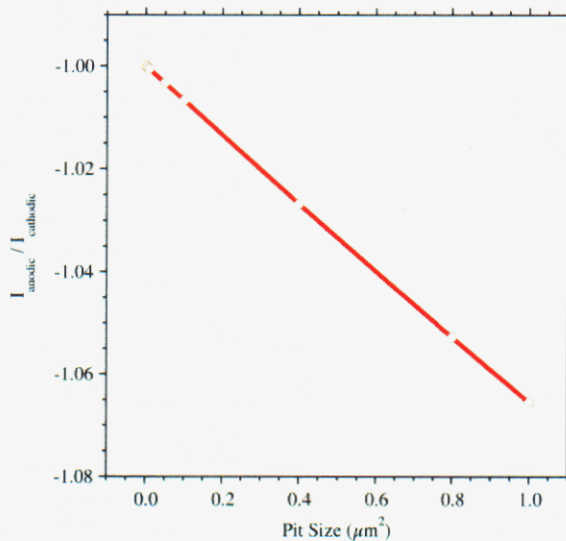
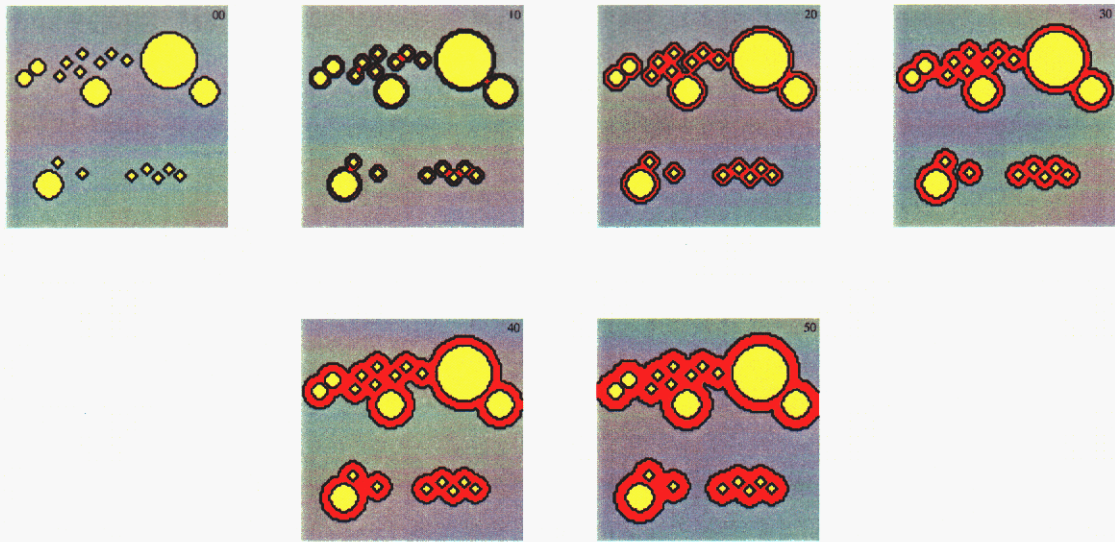
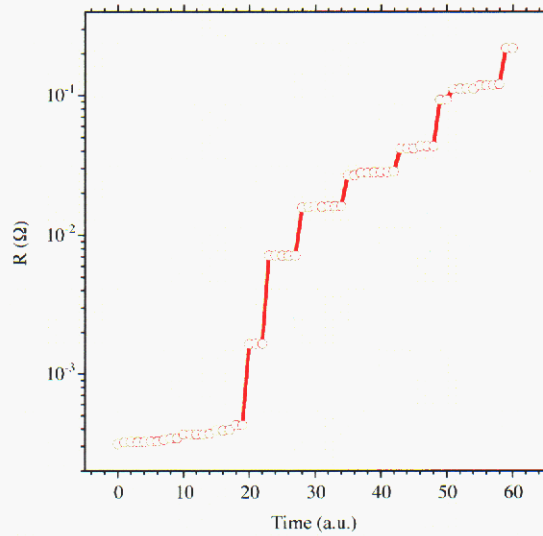


Figure 84 The ratio between the total anodic and cathodic electrode currents as a function of pit size. The simulated system is an array of Cu dots with $330 \mu\text{m}$ diameter spaced $480 \mu\text{m}$ apart on Al covered by $1 \mu\text{m}$ of water with 50 mM NaCl . The node between and farthest from the Cu dots contains a pit (see Fig Figure 83b and text).



(a)



(b)

Figure 85 Simulations of electrical degradation due to corrosion around AuAl intermetallics in an Al bond pad. a) Cross-sections of the simulation domain are shown for selected times (denoted in the upper right of each image). Gray is Al, yellow is cylinders of a lower conductivity intermetallic, and red is non-conducting corroded regions at the interfaces. b) The effective resistance across the top and bottom faces increases discontinuously with time.

5 CONCLUSIONS AND SUMMARY

1. A gold atmospheric sensor was developed based on thin-film lithographic patterning techniques. Using this sensor to make electrochemical impedance spectroscopy measurements, it was possible to quantify differences in adsorbed electrolyte conductivity from approximately 0% RH up to 80% RH. This advance in atmospheric electrochemistry makes it possible to accurately quantify critical relative humidity levels associated with the formation of a conductive adsorbed electrolyte layer. If analogous sensors are built from engineering materials, it will be possible to quantify both the electrolyte conductivity and interfacial processes in the same experiment, across a wide range of RH.
2. Aluminum, copper and copper-coated aluminum electrodes were constructed from commercially available foils, wires and insulating materials. Various electrode configurations were used in conjunction with AC and DC electrochemical techniques to quantify atmospheric corrosion behavior. At low RH the foil-based electrodes tend to mask AC signals, but sensitivity to DC signals was exceptional. The data from these electrodes demonstrates the ability to electrochemically resolve both uniform and localized corrosion phenomena over a broad range of atmospheric conditions.
3. Electrodes were constructed to measure the galvanic corrosion behavior of an aluminum-copper couple under atmospheric conditions. The corrosion current was resolvable and the values were sensible for RH levels down to approximately 0%RH. The galvanic current provides a good metric for assessing the critical RH level for accelerated corrosion of this material couple. The galvanic current measurements were also extremely sensitive to small, localized corrosion events. It was possible to measure current transients corresponding to material loss on the order of 10^{-16} grams. This sensor type can be applied to assessing materials compatibility under benign environmental conditions.
4. An electric field model was written to calculate current and potential field information for heterogeneous systems with either linear or non-linear boundary conditions. The modeling has been used to demonstrate the effects of solution layer thickness, heterogeneous microstructure, localized attack and secondary particle separation on potential and current gradients. The data suggest that under inundated conditions the initiation of corrosion at secondary phase particles *can not* be sensibly linked to local potential gradients. However, as solution layer thickness decreases, potential gradients can be severe enough to strongly influence the location of corrosion initiation and propagation.

Overall, the results from this program demonstrate that electrochemical measurements are a viable means of making quantitative, in-situ measurements under mildly accelerating atmospheric conditions. Based on the current work, it will be possible to implement in-situ monitoring in atmospheric studies, better characterize the

conditions leading to accelerated damage, and provide insight into the mechanisms of degradation. Furthermore, the sensor technology developed here provides a stepping stone for the design of early-warning corrosion sensors.

6 REFERENCES

1. F. Mansfeld, in *Electrochemical Corrosion Testing*, ASTM STP 727 (1981) pp. 215-237.
2. F. Mansfeld, in *Atmospheric Corrosion*, ed. W.H. Ailor, John Wiley and Sons, New York, NY (1982) p. 139.
3. Nishikata, Y. Ichihara, T. Tsuru, *Corrosion Science*, Vol. 37, No.6 (1995) pp. 897-911.
4. H. Katayama, Y.-C. Tay, A. S. Vilorio, A. Nishikata, T. Tsuru, *Materials Transactions, JIM*, Vol. 38, No. 12 (1997) pp. 1089-1094.
5. N. Nishikata, Y. Yamashita, H. Katayama, T. Tsuru, A. Usami, K. Tanabe, H. Mabuchi, *Corrosion Science*, Vol. 37, No. 12 (1995) pp. 2059-2069.
6. G. A. El-Mahdy, A. Nishikata, T. Tsuru, *Corrosion Science*, 42 (2000) pp. 1509-1521.
7. Y. Cheng, J. Luo, L. Zheng, Y. Du, C. Cao, *Bulletin of Electrochemistry*, 13, 6 (1997) pp. 280-283.
8. V. Kucera, J. Gullman, *Electrochemical Corrosion Testing*, ASTM STP 727 (1981) pp. 238-255.
9. F. Mansfeld, S. Tsai, *Corrosion Science*, Vol. 20 (1980) pp. 853-872.
10. F. Mansfeld, S. L. Jeaniaquet, M. W. Kendig, D. K. Roe, *Atmospheric Sciences Research Laboratory, Office of Research and Development, United States Environmental Protection Agency, Research Triangle Park, NC, EPA/600/S3-85/048* (July, 1985).
11. F. Mansfeld, *J. Electrochem. Soc.*, Vol. 135, No. 6 (1988) pp.1354-1358.
12. J. A. González, E. Otero, C. Cabañas, J. M. Bastidas, *Br. Corros. J.*, Vol. 19, No. 2 (1984) pp. 89-94.
13. J. E. Hatch, Ed., *Aluminum: Properties and Physical Metallurgy*, ASM, Metals Park, OH, 1984.
14. R. B. Comizzoli, *Materials Developments in Microelectronic Packaging Conference, Proceedings of the 4th Electronic Materials and Processing Congress, ASM International, Montreal, Quebec, Canada, August 19-22 (1991) pp. 311-316.*
15. M. Kendig, F. Mansfeld, *Corrosion*, Vol. 39, No. 11 (1983) 466-467
16. *Corrview v2.3d*, Scribner Associates, © 1990-2000, www.scribnerassociates.com.
17. R.S. Munn, "The Modeling of Galvanic Corrosion Systems Using Numerical Methods with Particular Attention to Boundary Conditions of Nonlinear Polarization," Ph.D. Dissertation, (Univ. of Conn. 1986).
18. W.L. Briggs, "A Multigrid Tutorial" (*Soc. Ind. Appl. Math.*, 1987).
19. T.R. Beck, "Salt Film Formation During Corrosion of Aluminum," *Electr. Acta* 29 (1984) p485-91.
20. N.R. Sorensen et al., "Physical Models for Predicting the Effect of Atmospheric Corrosion on Microelectronic Reliability," SAND2000-3008 (Dec 2000).
21. W.H. Press, S.A. Teukolsky, W.T. Vetterling, and B.P. Flannery, "Numerical Recipes in C," 2nd Ed.(Cambridge, 1992) p. 83-9.

7 ACKNOWLEDGEMENTS

This work was supported by a Sandia Laboratory Directed Research and Development (LDRD) Project. We extend our gratitude to Sam Lucero, Rob Sorensen and Jeff Braithwaite for their participation and guidance in the design and implementation of the gas exposure system used in this work, and their help with the interpretation of atmospheric corrosion data. Sandia is operated by the Department of Energy under Contract DE-AC04-94AL85000. Sandia is a multi-program laboratory operated by Sandia Corporation, a Lockheed Martin Company, for the United States Department of Energy.

8 APPENDICES

APPENDIX A: Electrophoretic Paint for Coating Metal Foils and Wires

The foils and wires used to make atmospheric corrosion sensors were coated with a thin insulating layer prior to assembling the electrode. The insulator had to be adherent, inert, non-conductive and uniform. The product selected for this purpose was an electrophoretic paint manufactured by PPG Automotive (part #ED5050B). The paint is used commercially for providing corrosion protection to the undercarriage of automobiles. In the commercial application the paint is applied very thick (hundreds to thousands of microns); whereas the application in this project required very thin layers. Therefore, efforts were made to determine suitable application procedures for our specific purpose.

The basic procedure was to expose the part to a bath consisting of 50/50 paint and deionized water, then apply a fixed DC voltage for a set length of time. The parts to be coated were polarized cathodically using a niobium plated Ti mesh counter electrode. After coating the parts were rinsed in deionized water then baked at 170°C for 30 minutes. The baking step acts to cross-link the polymers in the coating and gives rise to the insulating properties. The thickness is a function of the applied potential used during the coating process and the length of time that the potential is applied. The parts in this program were coated for 2 minutes. The relationship between coating potential and final thickness is shown in Table A1. In general, the separation of the electrodes in the atmospheric sensors was determined by the sum of the coating thickness and the epoxy potting compound that wicked between the electrodes. Therefore, the electrophoretic paint thickness was not critical, only that it be minimized without compromising coating integrity. In this program all of the wires and foils were coated at potentials between 5 and 20 Volts.

Coating Potential (V)	Average Thickness (μm)	Maximum Thickness (μm)	Minimum Thickness (μm)
-20	4.1	4.2	3.7
-15	4.1	4.4	3.9
-10	3.7	4.0	3.4
-7.5	2.8	3.1	2.4
-5	2.2	2.7	1.9
-4.5	1.1	1.3	1.0
-4	2.1	2.3	1.9

Table A1. Coating thickness as a function of coating potential. 10 measurements were made along a length of aluminum foil for each potential investigated.

APPENDIX B: Copper Plating of Al Foils

Cu was plated onto Al foils in order to create a material interface that would be susceptible to accelerated attack under atmospheric conditions. The Cu was intended to anodically polarize the Al, thus increasing the passive current density and inducing localized corrosion. Because of the insulating native oxide on Al, special procedures had to be used to achieve the desired Cu plating characteristics. The three critical components to the process are (1) cleaning / oxide disruption, (2) applying a Cu strike layer, and (3) Cu plating.

Two procedures were developed for disrupting the oxide on the Al. The first method is to mechanically polish the Al foil using 1000 grit SiC paper. The foils are wet-polished (using deionized H₂O) until a matte gray finish is achieved. After polishing the foils are rinsed in deionized H₂O to remove polishing media. The second method is to clean in a 10% Brulin bath at 140°F for 10 minutes. If thick foils are being prepared, ultrasonic action can be used to stimulate the process. Thin foils (e.g., 25 μm) were easily damaged by ultrasonic action. After the foil surfaces are prepared (using either process) the foils should be stored for up to three hours in 50% HNO₃ until the Cu-strike is applied. It was generally observed that 10 to 30 minutes in HNO₃ improved the quality of the Cu-strike.

The strike solution was prepared in 500 ml batches using the following procedure. Fill a mixing vessel with about 250 ml of H₂O. Add 35.5 ml of ethylene diamine (some smoke will evolve from the vessel and a sizzling sound may be heard). Add 24.5 g of CuSO₄ (additional sizzling may be heard). Add approximately 150 ml of additional H₂O. Add an additional 30 g of CuSO₄ (for a total of 54.5 g). Mix the solution then add additional H₂O to bring the total volume to 500 ml. The final solution will be dark purple in color. Cu strike is applied by immersing foils prepared as described above in the strike solution at 55°C for 10 minutes. After the strike is applied, the samples may be stored for several days under ambient conditions before the Cu plating is applied.

The plating solution was prepared in 1000 ml batches using the following procedure. Add 250 ml deionized H₂O to a 1000 ml volumetric flask. Add 240 g of copper sulfate (technical crystal, FW = 249.68 g/mol, CuSO₄·5H₂O). Add 41 ml of concentrated sulfuric acid (41 ml * 1.84 g/ml = 75 g H₂SO₄). Add deionized H₂O to bring the total volume to 1000 ml. The plating bath should be used at 40°C. The plating is applied in a current controlled mode with a current density of 75 to 200 mA/cm². A current density of approximately 80 mA/cm² was used in this program. Plating times varied from 100 s to 400 s. Final thickness of the Cu ranged from 10 to 40 μm.

9 DISTRIBUTION

Sandia National Laboratories:

1	MS1415	N. A. Missert
1	MS1411	C. C. Battaile
2	MS0888	M. A. Martinez
5	MS0888	F. D. Wall
1	MS0888	J. W. Braithwaite
1	MS0888	N. R. Sorensen
1	MS1415	J. C. Barbour
1	MS9018	Central Technical Files, 8945-1
2	MS0899	Technical Library, 9616
1	MS0612	Review and Approval Desk, 9612 for DOE/OSTI